CHARACTERIZATION OF EPITAXIAL SEMICONDUCTOR FILMS BY SCANNING TUNNELING MICROSCOPY AT AMBIENT PRESSURE

by

THOMAS HENRY PINNINGTON

B.Sc. University of Alberta, 1990

A THESIS SUBMITTED IN PARTIAL FULFILLMENT OF

THE REQUIREMENTS FOR THE DEGREE OF

MASTER OF APPLIED SCIENCE

in

THE FACULTY OF GRADUATE STUDIES

DEPARTMENT OF ENGINEERING PHYSICS

We accept this thesis as conforming

to the required standard

THE UNIVERSITY OF BRITISH COLUMBIA

December 1992

In presenting this thesis in partial fulfilment of the requirements for an advanced degree at the University of British Columbia, I agree that the Library shall make it freely available for reference and study. I further agree that permission for extensive copying of this thesis for scholarly purposes may be granted by the head of my department or by his or her representatives. It is understood that copying or publication of this thesis for financial gain shall not be allowed without my written permission.

(Signature

Department of Engineering Physics

The University of British Columbia
Vancouver, Canada

Date Dec 31/92

ABSTRACT

Epitaxial layers grown by molecular beam epitaxy on both silicon and gallium arsenide substrates are exposed by cleaving and studied by scanning tunneling microscopy (STM) at ambient pressure. The cleaved surfaces are prepared for imaging by wet chemical treatments. GaAs/AlGaAs and Si/SiGe multilayer structures are imaged with ~1 nm resolution. The contrast in the STM images is believed to be topographic in origin, resulting either from selective etching during surface preparation or strain-relaxation at the cleaved surface. Layers of alternating dopant-type are also resolved. In particular, alternately doped layers on GaAs are imaged by STM for the first time in air, and the pn junctions located to within 20 nm. The apparent topographic contrast in these images is explained in terms of an electronic contrast mechanism associated with the carrier type.

Current-voltage (IV) characteristics of the STM tunnel junction are obtained at selected locations in the epitaxial layers. IV curves acquired over n- and p-type regions resemble the IV characteristics of Schottky barrier diodes. A new imaging method is proposed which exploits the contrast between the n- and p-type IV curves. Imaging in this mode is achieved by repetitively interrupting the constant-current feedback loop during the scan and recording the tunnel current at a new tip-sample voltage setting, preselected to yield high conductivity-type contrast. This method, which decouples the electronic contrast associated with the carrier type from the topography, is demonstrated for an npn structure on GaAs.

Modification of the treated GaAs and Si surfaces is observed during imaging, and is attributed to a chemical change in the surface enhanced by the tunneling process. Photoemission spectroscopy of the treated GaAs surface indicates that the treatment inhibits oxidation, possibly by formation of a thin sulfur passivation layer. The photoemission results also suggest that selective removal of the arsenic atoms occurs during the treatment, which may also help to produce a more stable surface.

TABLE OF CONTENTS

LIST OF FIGURES

ACKNOWLEDGEMENTS

I would first like to express my thanks and gratitude to Dr. Tom Tiedje, whose insightful comments, enthusiastic assistance, and infectious optimism made this work possible and enjoyable. I gratefully acknowledge the contributions of my collaborators, in particular Steve Patitsas for stimulating theoretical discussions, Aaron Sanderson for his invaluable assistance in developing the current-voltage measurement technique, and Dr. T. P. Pearsall, who suggested the Si/Ge STM study, for his encouragement and support. The cooperation and assistance of Christian Lavoie and Shane Johnson, who grew the GaAs samples for these studies, is greatly appreciated. I also thank Dr. P. C. Wong and Tony Van Buuren for performing XPS and synchrotron PES measurements respectively, and also for helping me to interpret the data. I am indebted to Dr. J. A. Dagata, whose surface preparation technique has made the GaAs measurements possible, for his helpful advice and encouragement. The Si samples used in these experiments were supplied by Dr. D. C. Houghton, Dr. J. P. Noel, and Greg Mattiussi, whose interest and cooperation are gratefully acknowledged.

Finally I thank Jim Mackenzie and Shane Johnson for help with the figures, and Yuan Gao for typing in references.

1. Introduction

The improved performance associated with the miniaturization of electron devices has motivated the evolution of characteristic semiconductor device geometries to submicron scales. In the case of integrated circuit technology, the reduction in electron transit times as device density is increased results in faster operation. Such devices are produced by thermal diffusion or ion-implantation/anneal, of dopant atoms, producing three-dimensional structures of varying dopant type and concentration.[1,2] In the case of quantum well devices, such as quantum well lasers and photodetectors, efficiency is enhanced as electrons are confined to smaller regions.[3,4] Confinement in one dimension can be achieved by growing alternating layers of lattice-matched materials of different bandgaps, such as GaAs and AlGaAs, by molecular beam epitaxy.[5] Device structures are fabricated on semiconductor substrates and the relevant geometries extend perpendicular to the plane of the surface. High resolution characterization methods are needed to monitor production of devices and to permit meaningful comparisons between actual device behaviour and computer simulations based on device geometry.[6] In particular, dopant concentration and chemical composition both need to be measured as a function of position in the fabricated stuctures. Also, interdiffusion of chemical species, and defects in the crystal structure such as dislocations arising from lattice mismatch strain relaxation must be monitored, as these degrade the quality of the interfaces between regions of differing composition or doping and can dramatically affect performance.

Scanning tunneling microscopy[7] (STM) which is capable of atomic resolution imaging on semiconductor surfaces[8,9] and is sensitive to spatial variations in electronic properties[10,11], is a promising candidate for semiconductor device characterization. In STM, a sharp metal probe is scanned across the sample surface. The probe is held at a fixed potential with respect to the sample, and the distance between the tip of the probe and the sample surface is kept small enough (typically less than 20 Å) to permit quantum

mechanical tunneling of electrons to occur between the tip and sample. This is achieved using feedback control techniques[12], typically by adjusting the tip-sample separation to maintain a constant current of tunneling electrons. An image is acquired by monitoring the relative change in tip-sample separation as a function of location of the scanning probe. This image corresponds to the surface topography if the surface is electronically homogeneous, although more generally both electronic and topographic information is acquired simultaneously, making data interpretation more complicated. Purely electronic information can be extracted through analysis of current-voltage characteristics of the tip-sample tunnel junction.[9,13] These are acquired by interrupting the scan and disabling the constant current feedback loop, and then monitoring the tunnel current as the tip-sample bias is varied. Alternatively a small, high frequency voltage modulation signal, outside the bandwidth of the feedback loop, can be added to the tip-sample bias while scanning and the corresponding small-signal current modulation recorded.

Methods involving STM as described above have been successfully applied to the characterization of semiconductor devices.[14] In ultrahigh vacuum (UHV), STM has been used to examine GaAs/AlGaAs interfaces with atomic resolution[15]. Recently, GaAs layers of alternating doping type were resolved in UHV.[10] In these experiments, a piece of the wafer containing the device structures was cleaved in situ, permitting measurements to be made on the structures, which were exposed in crossection. Measurements on Si have also been made, although the sample is usually cleaved outside of the UHV chamber and chemically treated before imaging.[16] This is because it is difficult to produce a smooth cleave on Si, and anyway the electrical properties of the clean Si surface do not make it amenable to STM measurements of carrier-type.[10,16] Similar techniques have been used in ambient pressure STM, where chemical treatments are used to inhibit oxidation of the cleaved surfaces. Measurements on both Si [16] and more recently GaAs [17] structures have been made, although not with atomic resolution. Sensitivity to carrier type and carrier concentration has been demonstrated both in air[18] and in UHV[16] STM.

Traditional device characterization methods complement the information provided by STM, but typically can only achieve high spatial resolution in one dimension. Photoluminescence, for example, has been used to determine the overall thickness and interface quality of electron confinement layers.[19] Capacitance-voltage (C-V) measurements[19,20] yield carrier concentration as a function of depth below the substrate surface, based on the change in capacitance between a surface contact and the sample with changing voltage. Secondary ion mass spectroscopy (SIMS), in which material is removed from the sample by an ion beam, measures the concentration of dopant atoms directly (as opposed to carrier concentration).[20] By taking measurements at several locations and comparing the data with computer simulations, SIMS and C-V data have been used to construct two-dimensional dopant and carrier-concentration profiles indirectly, with 100 nm resolution.[6,14]

The combined sensitivity to sub-nanometer topographic contrast and capability of extracting quantitative electronic information, is an advantage of STM methods over other electron microscopy techniques. Scanning electron microscopy (SEM) for example, has been used to locate pn junctions using the electron beam induced current (EBIC) method.[14] The high energy electron beam creates electron-hole pairs as it scans the surface, and the excess minority carriers drift under the action of the local field in the pn junction, producing the EBIC signal which is detected in an external circuit. The resolution of the pn junction location by this method is limited to the width of the space-charge region.[6] Field emission SEM micrographs, as presented in this work, are sensitive to conductivity type, but it is not possible to differentiate between electronic and topographic contrast in the micrographs. Also, SEM is not sensitive to topography of less than a few nanometers. Transmission electron microscopy (TEM) in which an electron beam is transmitted through a thinned sample, provides two-dimensional information with high spatial resolution, but the measurement represents an average over several hundred atomic planes, due to the finite

thickness of the sample. Furthermore, dopant profiling requires the use of selective etchants or stains,[21] and TEM sample preparation times are much longer than for STM.

In this work, ambient pressure STM as a tool for semiconductor device characterization is investigated. The test structures consist of epitaxial layers of alternating chemical composition and dopant type, grown by solid source MBE on Si and GaAs substrates. These are imaged in cleaved-crossection following wet chemical treatments of the freshly cleaved surfaces to permit stable imaging at ambient pressure. The STM used in these experiments is described in Chapter 2. Results obtained on untreated surfaces are presented in Chapter 3, accompanied by a description and evaluation of the procedures developed to prepare the samples for imaging. Measurement artifacts associated with non-idealities of the scanning probe are discussed in Chapter 4 to permit more meaningful interpretation of the crossectional STM measurements. The results of these measurements are presented in Chapter 5, along with a discussion of the electronic and topographic contrast mechanisms present in the images. A theoretical description of conduction across the STM tunnel junction is given in Chapter 6. In Chapter 7, current-voltage characteristics of the tunnel junction obtained at selected locations in the epitaxial layers are presented, and used to explain the electronic contrast observed in the constant current images. The current-voltage measurements are accompanied by results acquired using a new imaging technique, developed to decouple the electronic contrast from the topographic contrast.

2. Scanning Tunneling Microscope

2.1. Description

The scanning tunneling microscope used in these experiments uses a piezoelectric scanning device under integral feedback control of the tunneling current.

The scanning device consists of a platinum-30%iridium tunneling probe concentrically mounted to the end of a 10 mm diameter PZT-5H (lead zirconate titanate) piezoelectric tube, the other end of which is rigidly fixed. The free section of the tube, illustrated in Fig. 2.1, is 20.4 mm long and the tube wall thickness is 0.84 mm. A

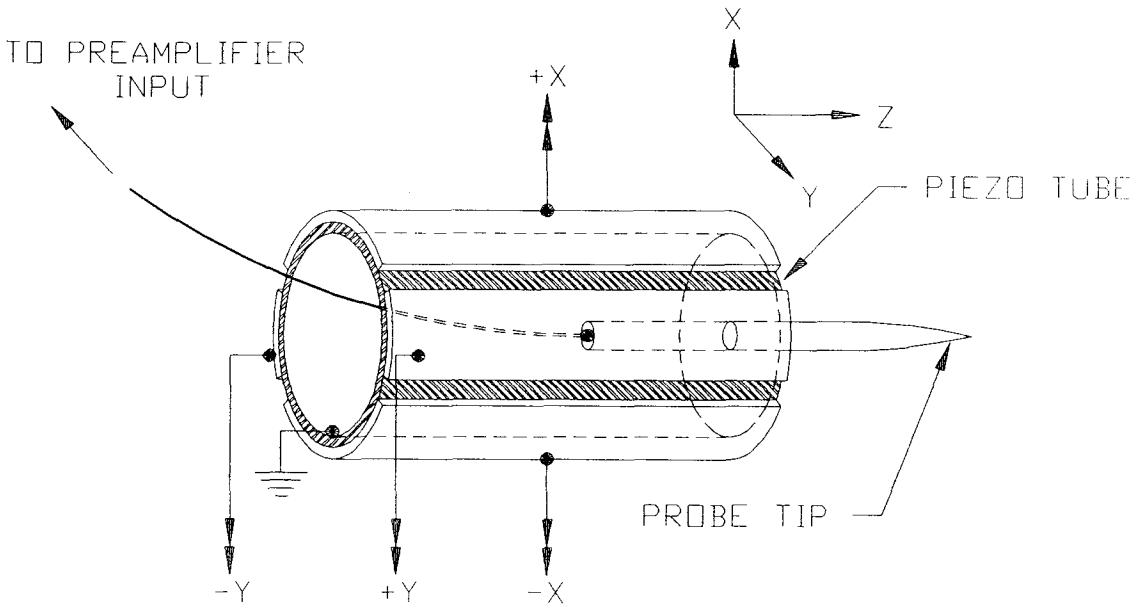

Fig. 2.1. Free section of scanning tube, showing electrode configuration.

ceramic (Macor) disc at the free end and another in the middle secure the probe and electrically isolate it from the tube wall. Four high voltage electrodes on the outer wall of the tube are appropriately biased, up to a maximum of 206V with respect to the grounded inner wall electrode, to deflect the tube. Positive and negative bias on an electrode respectively expands and contracts that portion of the tube. Common mode voltage lengthens or shortens the tube. Scanning is accomplished by biasing opposing pairs of electrodes with voltage ramps of opposite phase.

The sample to be scanned is mounted on a horizontal cantilevered hinge plate. A spring-screw mechanism at the free end of the plate controls the deflection angle, allowing fine vertical positioning of the sample (≈1/160 inch per turn midway along the hinge plate). This entire mechanism is itself mounted on a micrometer stage, which enables the sample to be brought to within a micron of the probe tip, at which point the piezoelectric tube can bring the tip into tunneling range.

The preamplifier for the tunneling current signal is an op amp (OPA111 low noise amplifier) current-to-voltage conversion circuit. The feedback loop consists of a 1 MΩ resistor in parallel with a 1 pF capacitor. This configuration provides 1 mV/nA gain over a 5 kHz bandwidth. The probe is connected directly to the inverting input of the op amp with a short wire (about 2 cm) to minimize input capacitance. The probe tip is biased with respect to the chassis ground by applying the tip voltage to the non-inverting input.

2.2. Fabrication of Tunneling Probes

The tunneling probes are made either by cutting 0.25 mm Pt/Ir wire with scissors or by electrochemically etching the wire in a saturated NaCl solution using the 'drop-off' method[22]. In the electrochemical etching an ac voltage is applied between the Pt/Ir probe wire and a tungsten electrode. One end (~2 cm long) of the probe wire is inserted into a nylon sheath to protect it from etching. The wire is suspended vertically near the surface of

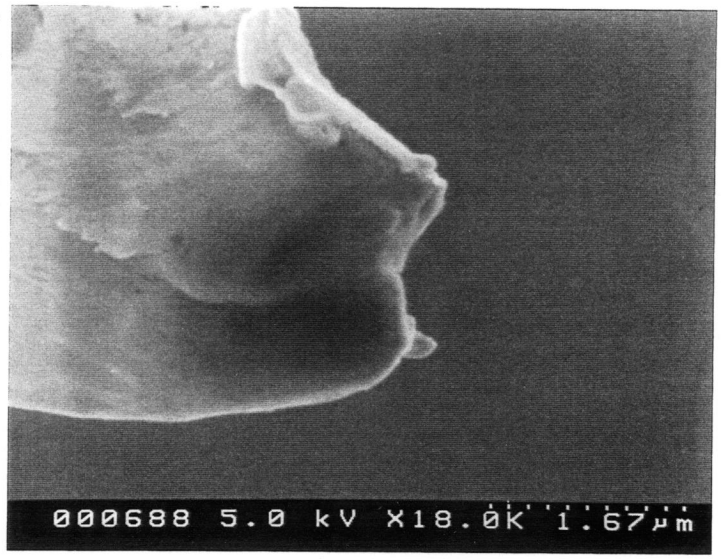

(a)

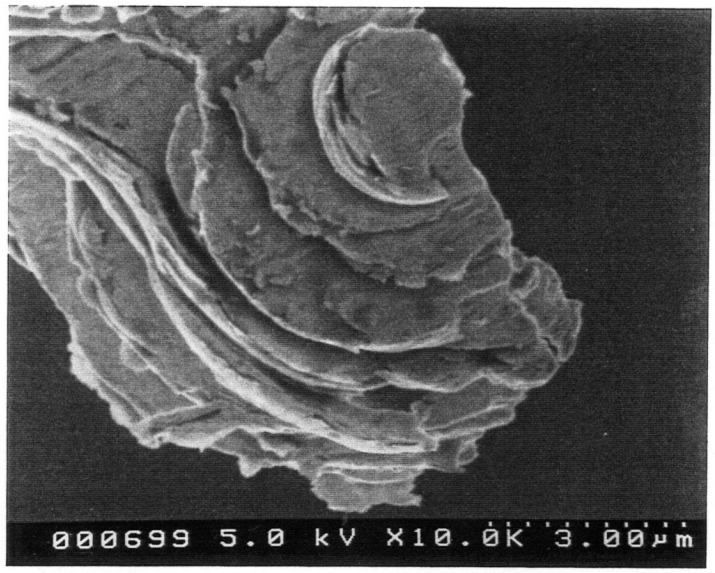

(b)

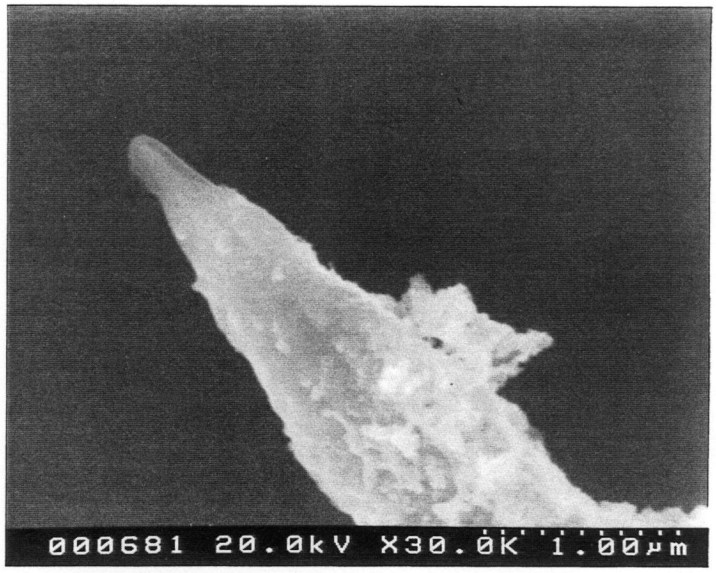

(c)

Fig. 2.2. SEM micrographs of probe tips produced by mechanical shearing (a) and (b), and by electrochemical etching (c). The length of the dotted line in lower right gives the scale. The dark grey film on the end of the etched tip is carbon deposited by the electron beam.

the salt solution so that the shielded end is fully immersed and only a small portion (~1 mm) of the exposed wire is below the meniscus. The etching voltage is high enough (~50 V) so that occassional sparking occurs at the Pt/Ir wire electrode, but is reduced to about 10 V before drop-off occurs to prevent annealing of the tip by the electrochemical current. The shielded end of the wire, which drops off, is removed from the nylon sheath, rinsed in an ultrasound methanol bath, and installed in the STM so that the etched end is the probe tip. The other end of the wire, which is connected to the voltage supply, continues to etch after drop-off resulting in a blunt tip which is not useful as a tunneling probe.

Fig. 2.2 shows SEM micrographs of both etched and cut probe tips. Mechanical shearing produces irregular probe tips (a) and (b), with many sharp points, whereas electrochemical etching results in more regular tips (c). Higher resolution micrographs of the tips indicated that a typical tip radius is about 20 nm for probes fabricated by both methods, although much larger radii (>100 nm) for etched tips result when the ac etching voltage is not reduced sufficiently before drop-off, as discussed above. Atomic resolution images were acquired on (100)-oriented graphite surfaces (in air) using both etched and cut probes.

2.3. Calibration of STM

The image acquisition software assumes a linear relationship between the the tube deflection and the voltage applied to the electrodes. Measurements were performed to establish appropriate deflection/voltage conversion factors, however nonlinearities in the actual piezo tube response result in increasingly large deflections per volt with increasing tube deflection. Systematic errors associated with this nonlinearity, which is about 20% for lateral and vertical deflections of 1 μm, result in distortion of images with large topographic or lateral range. This distortion is minimized by ensuring that the dc

component of the electrode voltages is kept small (by careful mechanical positioning of the probe) during image acquisition.

2.3a. Lateral Calibration

The scan range of the STM on small scales was calibrated using atomic resolution images of (100) graphite (ZYB monochromator calibration samples). Resolution of the hexagonal lattice (Fig. 2.3) was achieved at small values of tip bias (+0.01 V typically) and large tunneling current set points (about 5 nA). The centres of the hexagonal rings have a much lower electron density than the atomic cores, and appear black in the image. Three locations in the hexagonal lattice appear bright. These locations may correspond to locations of high electron density at the Fermi level. In many images, only these three points were resolved in each lattice. The spacing between the hexagon centres is known from x-ray diffraction to be 2.46 Å [23]. From these measurements, the lateral deflection of the scanner is found to be 12 nm/volt.

A sample consisting of arrays of regularly spaced holes in a film of TiN, evaporated on a silicon substrate, was used for large scale calibration. The sample was provided by Northern Telecom to study the quality of electrical contact holes made by photolithography. Fig. 2.4 is of a 2.0 μm x 2.0 μm square hole. These large scale scans are prone to considerable distortion due to nonlinearities in the piezoelectric deflection of the scanner. It appears that the image is compressed in the y-direction. Based on this image, the deflection is found to be roughly 14 nm/volt in the x-direction and 19 nm/volt in the y-direction.

In the images presented in this work, the lateral scale given is based on a conversion factor of 12 nm/volt. As discussed above, this linear conversion is only valid for small scan ranges (less than 1 μm).

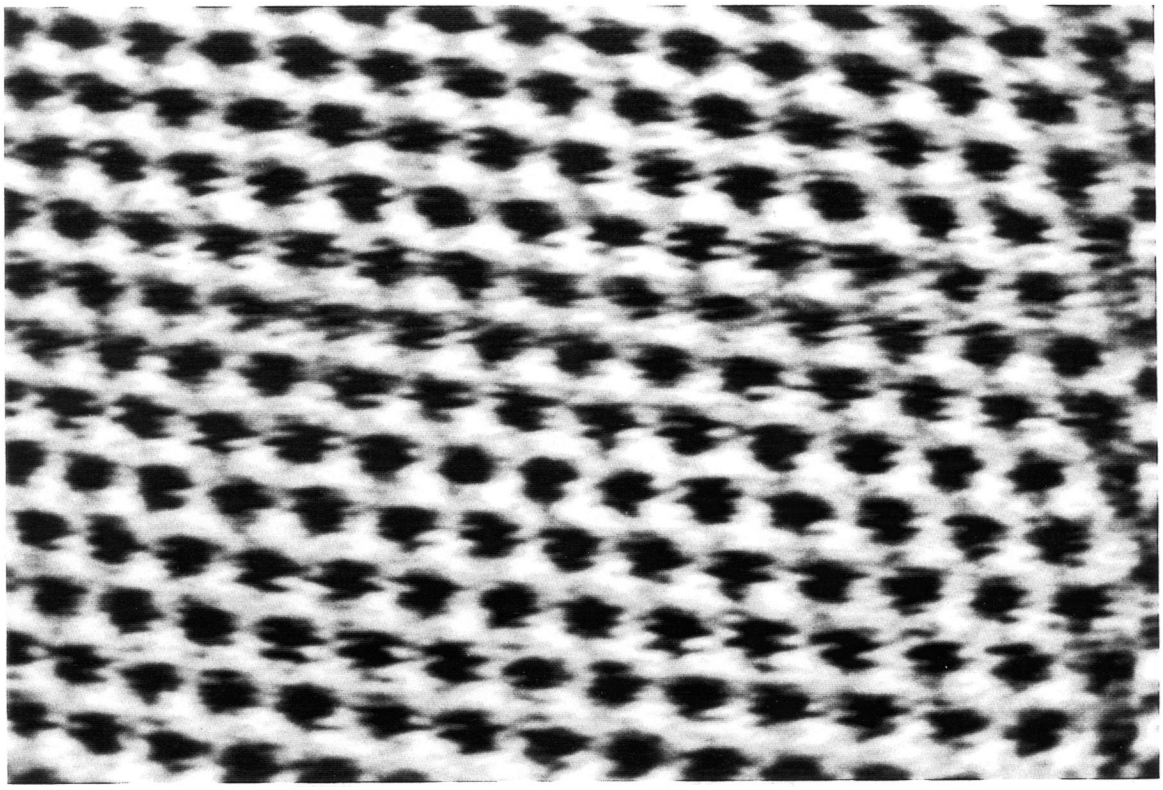

Fig. 2.3. Atomic resolution STM image of graphite. The spacing between hexagon centres is 2.46Å.

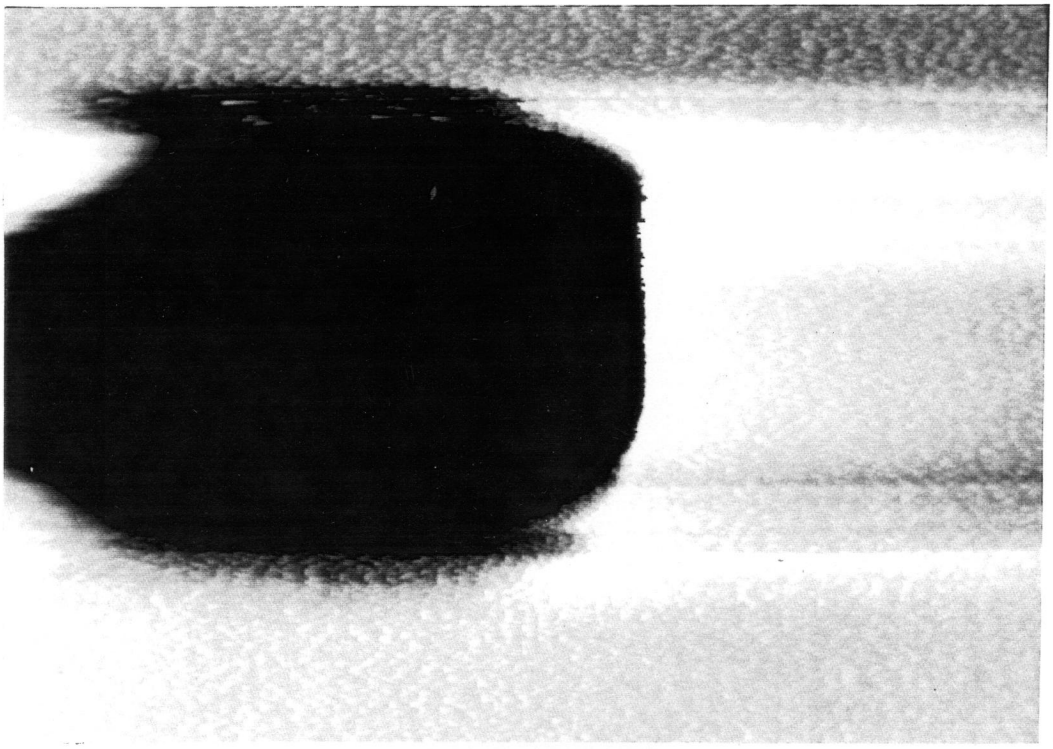

Fig. 2.4. STM image of 2 μm x 2 μm via contact hole on TiN film. The horizontal streaking is due to manual adjustments in the dc level of the common mode electrode voltage, to compensate for creep in the piezo tube (the signal was direct-coupled to the image acquisition system).

2.3b. Vertical Calibration

The vertical deflection of the scanning tube was calibrated using an optical position sensing device, which had 0.15 μm precision.[24] To reflect the sensing laser beam, a corner reflecter was mounted on the end of the tube, which was oriented vertically for these measurements. The vertical deflection as a function of common-mode electrode voltage is plotted in Fig. 2.5 for one series of measurements in which the maximum tube extension was 1 μm. The uncertainty in the calibration factor associated with the hysteresis of the piezoelectric is about 20% for these large-scale deflections. Based on an average of least-squares fits to data obtained for positive and negative deflections up to 1 μm, the calibration factor was determined to be 50±5 Å/volt (random error only).

The topographic scan line in Fig. 2.6 is taken across an image of a 2 μm x 2 μm TiN contact hole, obtained using an electrochemically etched probe which was sharp

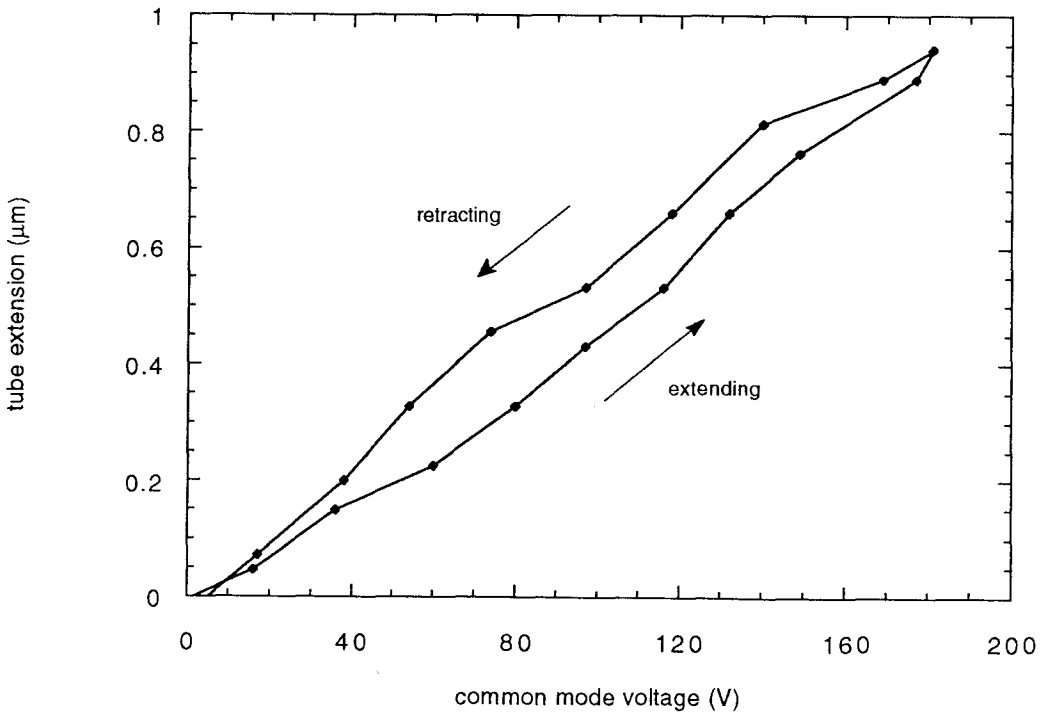

Fig. 2.5. Hysteresis loop of vertical deflection of the piezo tube, with applied common mode electrode voltage. Each deflection measurement was made 5 seconds after resetting the voltage.

enough to image the bottom of the hole. The depth of the hole, based on the calibration factor above, is approximately 850 nm (±10%), about 15% less than the nominal value of 1 μm.

An attempt was made to obtain a small-scale calibration based on scan lines across atomic steps on the graphite samples. This technique is used in UHV STM, for example using atomic steps on silicon surfaces.[25] Fig. 2.7 shows an air STM image of steps on the (100) graphite surface. A scan line across these steps, as well as two others across different steps on the same surface, appear in Fig. 2.8. The spacing of the atomic planes is known to be 3.5 Å from X-ray measurements.[23] Although the smallest steps observed were roughly 4 Å in height, step height was found to be an essentially continuous quantity (ie. not an integer multiple of 3.5 Å). Before imaging, the top few layers of graphite are peeled away to expose a fresh surface. It is likely that this procedure results in terraces which have been partially lifted off, so that the height of the terraces is ill-defined at the terrace edges (steps). This interpretation is consistent with the result that the height (based on 50 Å/volt) of the smallest steps agree with the known atomic spacing.

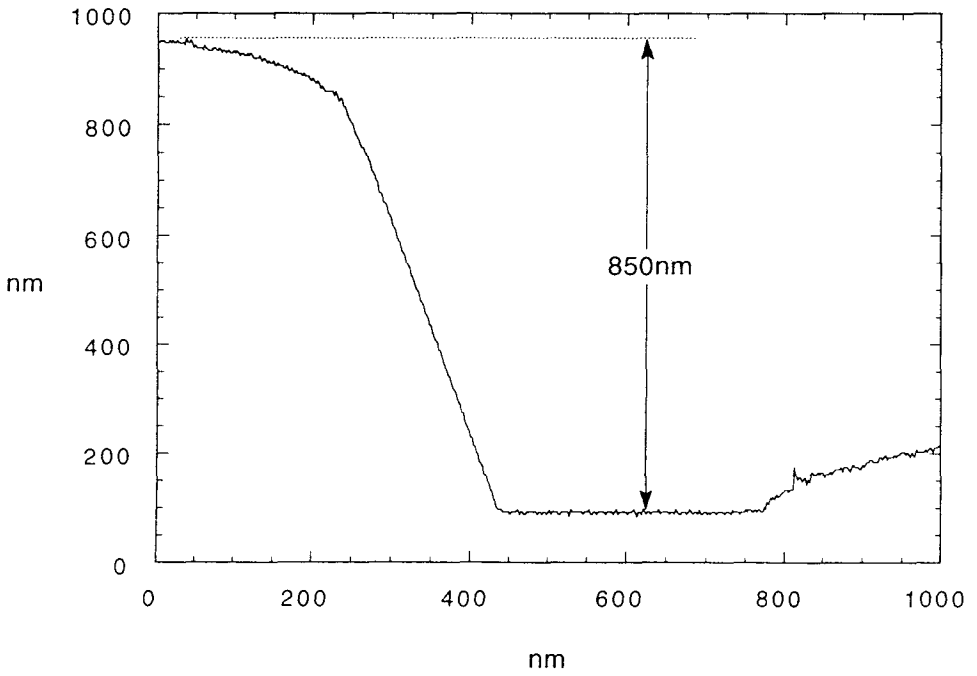

Fig. 2.6. Topographic scan line over a via contact hole. The nominal depth was 1 μm and the dimension shown (850nm) is based on the calibration factor determined from Fig. 2.5.

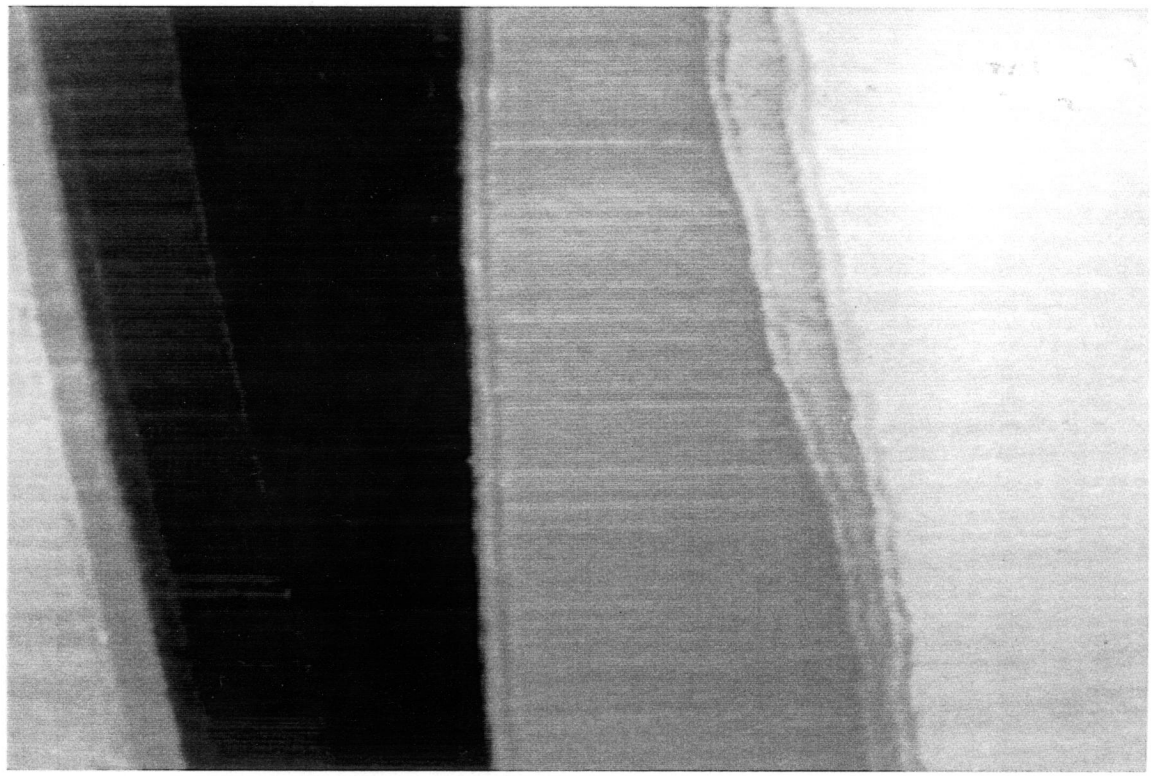

Fig. 2.7. Stepped terraces on graphite. The terraces are atomically flat.

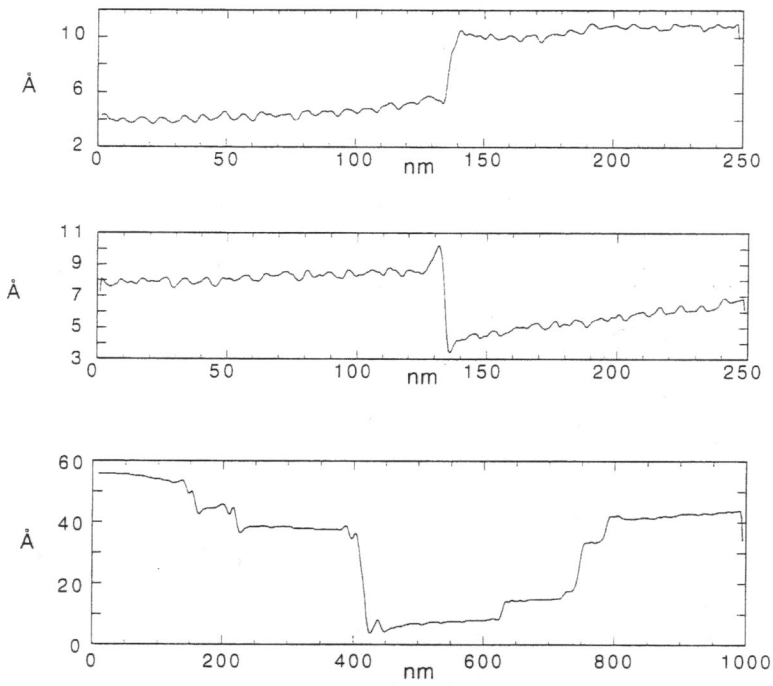

Fig. 2.8. Topographic scan lines obtained at atomic steps on graphite (top two scan lines), and across the terrace steps in Fig.2.7, above (bottom).

2.3c. Comparison with Theoretical Model

The longitudinal (Δz) and lateral (Δx) deflections of a piezoelectric tube (with this electrode geometry), with electrode voltage (V), can be described by a simple model[12],

$$\Delta z = \frac{L}{t} d_{31} V$$
$$\Delta x = \frac{L^2}{2rt} d_{31} V,$$

where L, t, and r are the tube length, wall thickness, and radius respectively. The piezoelectric constant, $d_{31}=2.74*10^{-10}$ m/volt for PZT-5H. For this tube geometry (see §2.1), these equations predict ($\Delta z/V$) = 6 nm/volt and ($\Delta x/V$)=14 nm/volt. The actual lateral scan range also depends on the length of the probe, λ, which extends beyond the end of the tube. If the curvature of the deflected tube is approximated to be zero, the scan range is increased by a factor of $((L+\lambda)/L)$ where λ is 5 mm typically, resulting in a lateral scan range of 17 nm/volt. These values are in rough agreement with the measured calibration factors reported above. This model is expected to over estimate the deflections by about 10% [12], and the tube dimensions are uncertain by roughly 5%.

3. Surface Preparation

STM measurements at ambient pressure were attempted on the untreated cleaved surfaces of GaAs and Si substrates. However, it was found that stable and reproducible images could only be consistently obtained after the surfaces had been passivated against oxidation by chemical treatments.

The goal of the preparation procedures described here is to produce a smooth surface, ideally atomically flat, which is stable enough to permit imaging at ambient pressure. The general approach for both the silicon and gallium arsenide substrates is to cleave the wafer along an atomic plane, followed by an immediate wet chemical treatment in which the surface is stabilized against oxidation. The stability of the treated surface depends critically on producing a smooth cleave, with no steps visible under an optical microscope. The cleave is produced by first scratching a small tick at the edge of the wafer with a diamond scribe, and then forcing the scribe 'open'. This is achieved by laying the wafer, scribed side down, on a rubber mat and applying pressure at the point on the edge of the wafer directly above the scribed tick with a tapered metal rod until the cleave is initiated. The cleave propagates away from the scribe, becoming smoother as it gets further along. For samples with epitaxially-grown layers, the scribe is made on the epitaxial side.

3.1 Imaging on Chemically Treated Surfaces

Image quality for both GaAs and Si surfaces was found to be dependent upon the tunneling current and tip bias. In particular, ambient pressure imaging was not possible with the tip bias at negative polarity, as this always resulted in a very noisy current signal. This effect is not observed in experiments performed in UHV, in which stable imaging is possible at both polarities[9,13]. It is believed that the electric field associated with a negative

tip promotes the chemisorption of an atmospheric species at the surface (perhaps oxidation). This interpretation is consistent with an early study[26] of the electric field dependence of Si oxidation. Large positive tip bias also tended to produce a noisy image and resulted in damage to the sample surface. The best images were obtained with the tip at +3 to +4 volts for GaAs and +1 to +2 volts for silicon.

It was necessary to keep the tunneling current low (about 0.2nA) and to scan at slow speeds (approximately 2seconds for a 1μm scan line or 8 minutes for a full 256-line image), with high gain in the feedback loop (RC=300μs). These settings represent a compromise between minimizing damage to the surface and achieving reasonable data acquisition rates. The concern is that scanning too close to the surface (by increasing the current set point or reducing the tip bias), or scanning at a high rate, increases the frequency and severity of tip crashes, in which the feedback control servo is unable to respond to sudden changes in surface topography. The result is either a sudden increase in the electric field as the tunneling gap narrows or actual tip-sample contact.

3.2. Silicon

3.2a Surface Preparation Procedure

Before resorting to chemical passivation treatments, an attempt was made to image the untreated, freshly cleaved (110) silicon surface. (100)-oriented silicon substrates were cleaved along the (110) direction. In order to produce surfaces with step-free regions, it was necessary to either cleave a large sample (greater than 1cm in length) or to thin the samples to less than 100 μm before cleaving. Fig. 3.1 is a scan taken in air immediately after cleaving a sample which had been thinned to 100 μm. Images acquired on the untreated surface were noisy and deteriorated with time. Moreover, scanning became very unstable or impossible within an hour of cleaving, presumably due to the build up of oxide.

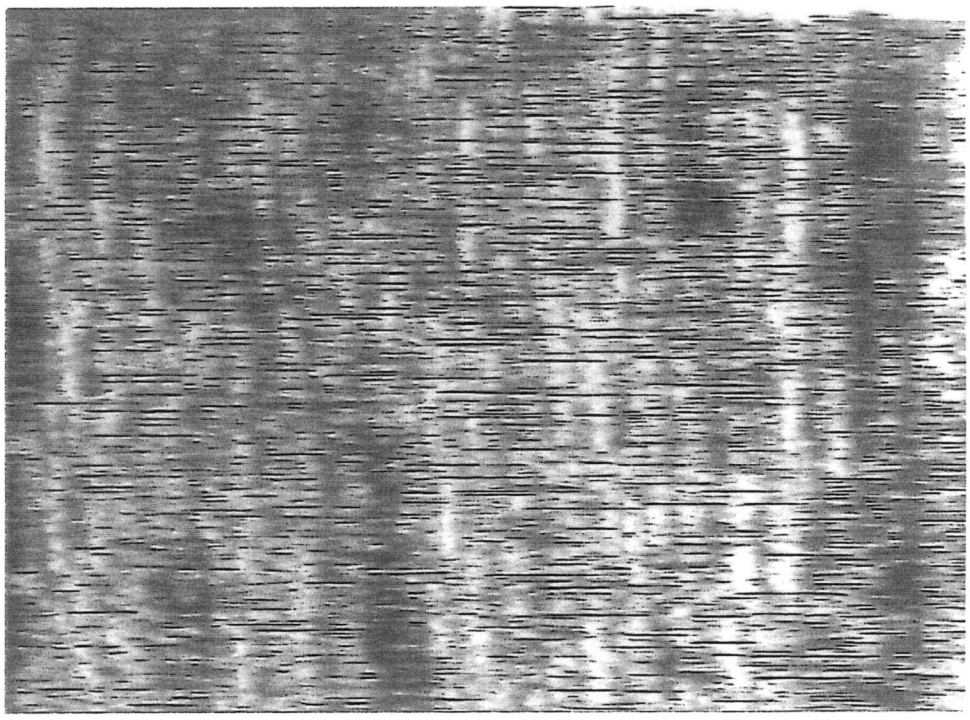

Fig. 3.1. STM image of freshly cleaved, untreated (110) silicon surface. The tunneling set point was +1 V on the tip and 0.1 nA tunnel current. Horizontal scan range (x) =1 μm. Vertical greyscale (z) =180 Å (white to black).

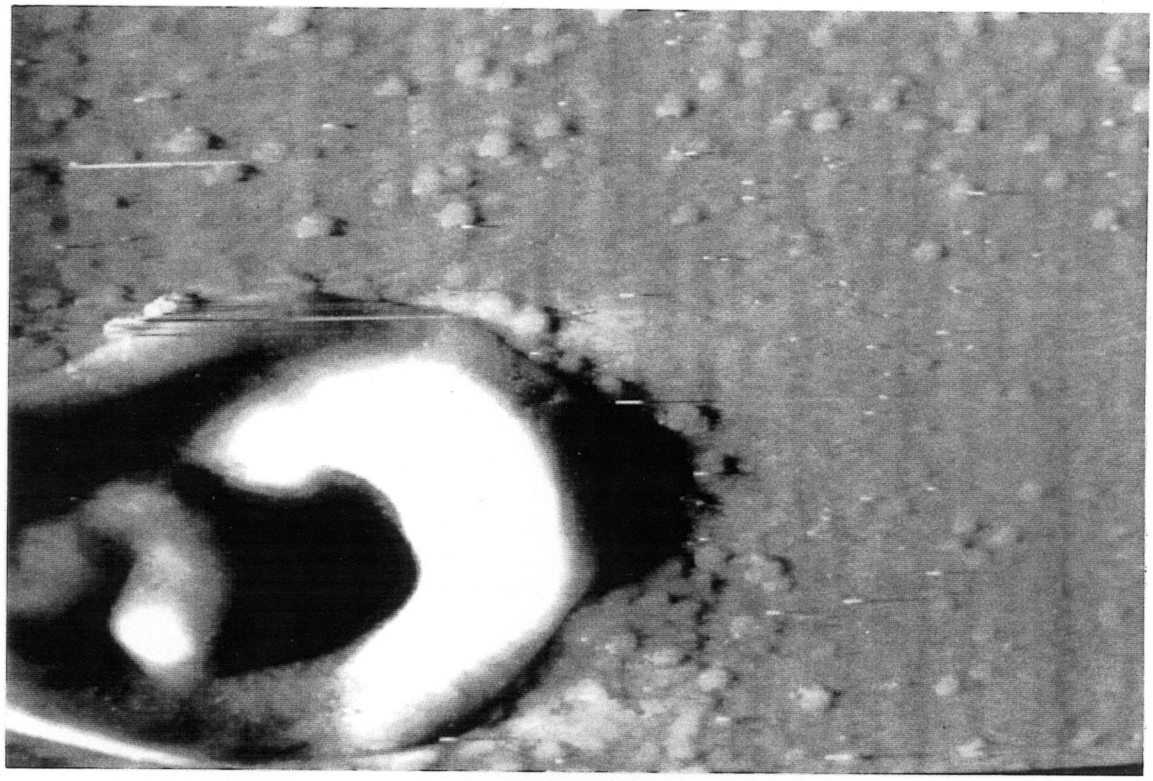

Fig. 3.2. Image of same surface as in Fig. 3.1., after etching in HF. The small, identically shaped features are tip images. Set point = (+2 V, 0.1 nA). x-range=2.0 μm, z-range greyscale=90 Å.

Fig. 3.2 shows an image taken on the same surface, with the same probe, as Fig. 3.1, following a dip in concentrated (49%) hydrofluoric acid (HF) for several seconds to remove the oxide. The cleaved surface had been exposed to room air for about 20 minutes prior to this treatment, which is known[13] to terminate the silicon surface with hydrogen. Following the HF dip, imaging was reproducible and stable for several hours. The prominent feature in the image may be surface damage resulting from a tip crash while positioning the probe. The image also contains many smaller identically shaped features, which were not observed prior to the chemical treatment. These features indicate the presence of sharp points on the surface which image the tip, as described below (§4.1). It is likely that the HF had etched the surface nonuniformly, producing these points.

Silicon surfaces treated with ammonium fluoride (NH_4F) solution have been imaged with atomic resolution in UHV STM.[27] Accordingly, this procedure was applied to imaging in air. The freshly-cleaved surface was dipped into concentrated (40%) NH_4F for about 30 seconds, followed immediately by a 5 minute soak in de-ionized (DI) water. The NH_4F solution is also believed to hydrogen-passivate the silicon surface.[27] The thorough DI water soak is necessary to prevent further etching of the surface. Exposure to the NH_4F for more than a few minutes resulted in non-uniform etching and a rough surface. Following the DI water soak, the sample was removed from the water and blown dry with nitrogen. In some experiments this last step was done in a nitrogen-filled glove bag which contained the STM, in order to minimize exposure to room air.

Fig. 3.3. shows an image acquired on an unthinned silicon substrate, which had been dipped in NH_4F for about one minute immediately after cleaving. The surface roughness is less than 15 Å, suggesting that the etch is much more uniform than in the HF treatments. Such surfaces imaged reproducibly after several hours in air, and up to 24 hours in nitrogen ambient. It was also found that it was possible to 'refresh' the surface once it had oxidized, by repeating the etching procedure. The image in Fig. 3.4 was taken on such a refreshed surface. Atomic resolution of the treated surfaces was not

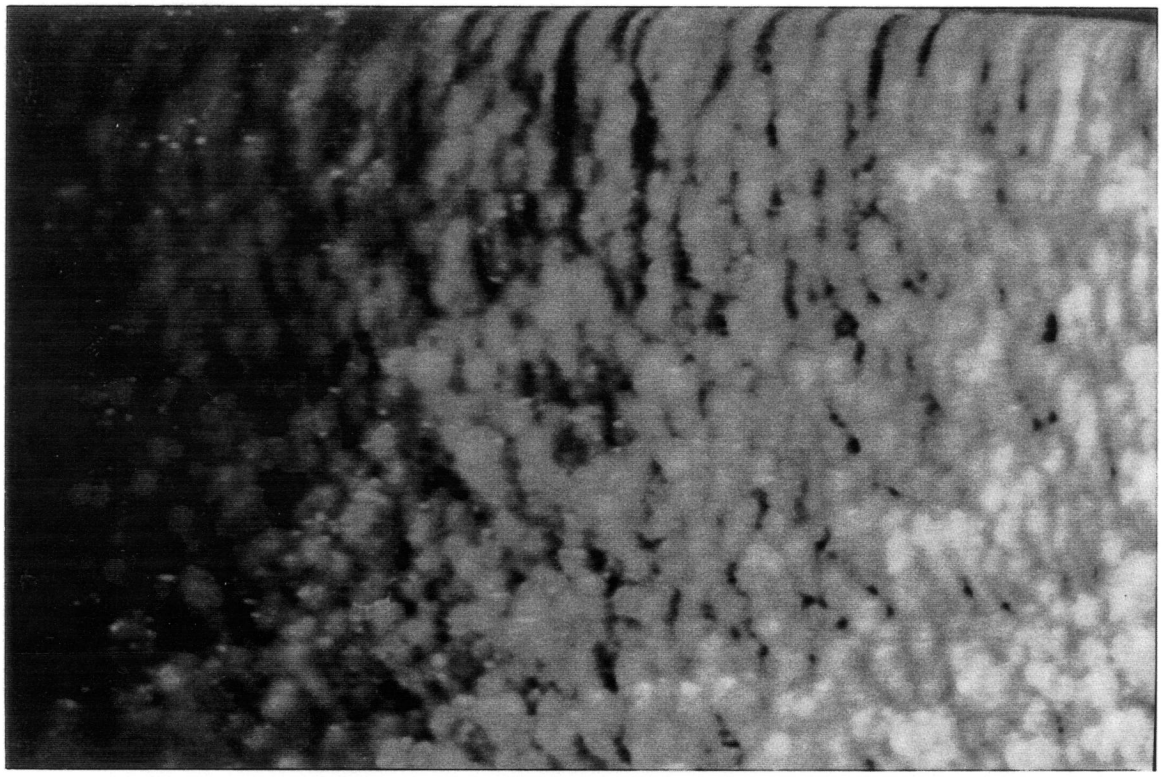

Fig. 3.3. Image acquired on a cleaved (110) n-type Si surface after etching in NH_4F. Set point = (+1 V, 0.3 nA). x-range=1 μm, z-range=100 Å.

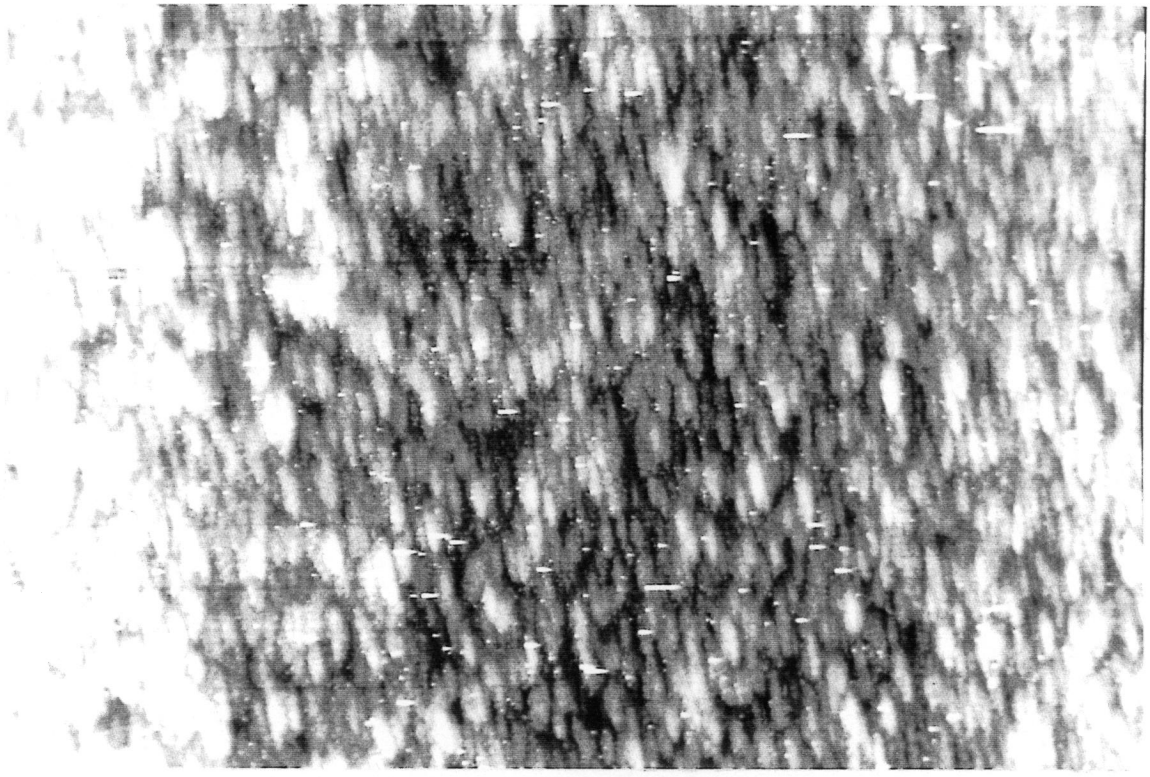

Fig. 3.4. Image of the same surface as in Fig. 3.3. following a 'refresh' treatment, 24 hours after the inital cleave. The surface roughness is about 15 Å. Set point=(+1V, 0.1 nA). x-range=1.5 μm, z-range=60 Å.

achieved in air or in the nitrogen-filled glove-bag. Etching times in the range of 10 seconds to 5 minutes were tried and all produced similar results.

3.2b. Tunneling-Induced Surface Modification

As discussed previously (§3.1) scanning conditions were chosen to reduce the probability of mechanical contact of the tunneling probe with the surface. Even with these precautions, modification of the surface due to scanning was observed on the NH_4F-treated samples. This damage occured to varying extents on different samples. A possible explanation is that the stability of the passivation treatment is dependent on the quality of the cleave, which varies among samples. Surface modification was enhanced as exposure of the surface to tunnel current increased, so that scans over smaller areas resulted in more damage than larger scale scans taken at the same rate per scan. One would expect that the opposite would be true if the damage were due to mechanical interaction of the tip and sample. The effect appears to be stronger at larger tunneling voltages, which is also inconsistent with a mechanical interaction mechanism. These observations suggest that the surface modification is caused by a chemical reaction, likely oxidation, assisted by the tunneling process. This effect has been studied on both cleaved and polished silicon surfaces by Dagata et.al.[28], who obtain similar results.

Fig. 3.5 shows an image of a cleaved p-type (dopant concentration=$1x10^{17}$ cm^{-3}) substrate. The image was acquired at a set point of (+3 V, 0.1 nA) following repeated scans over 3 successively increasing areas, with each scan taken in a time of 5 minutes, at that set point. The smaller area scan regions appear as progressively darker squares within the larger area scan regions. If this tunneling-induced surface modification were controlled, it could be used to fabricate device structures, enabling submicron control of lateral geometries.[28] Fig. 3.6 shows the results of an attempt to 'write' a sideways 'H' on

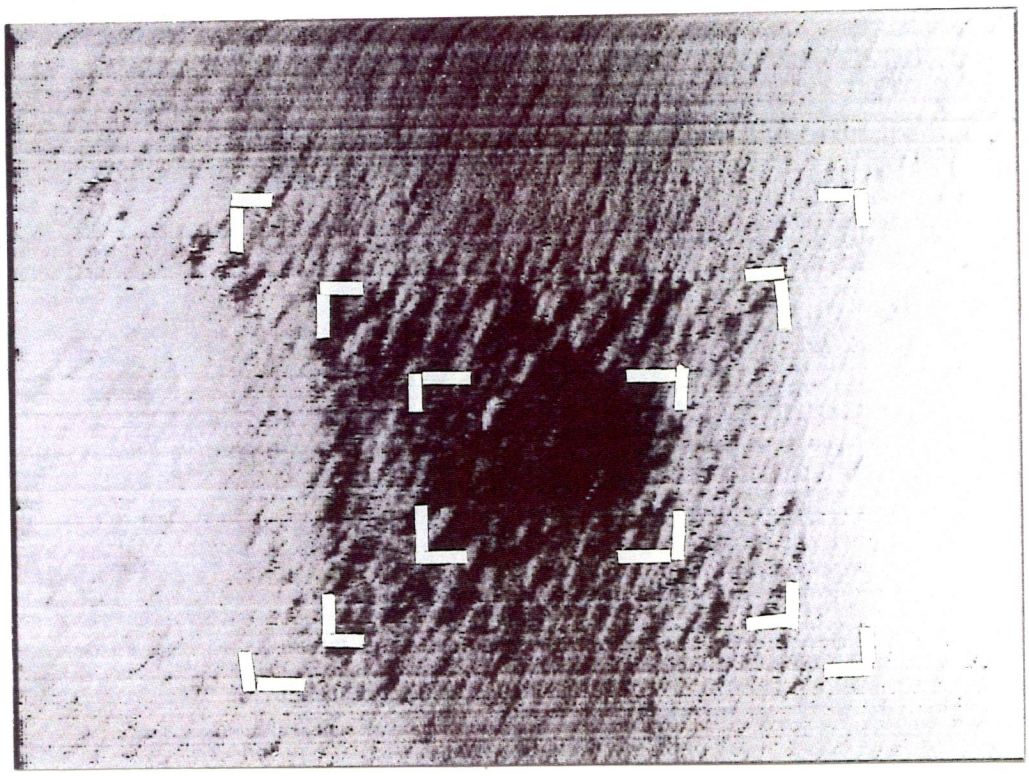

Fig. 3.5. Squares on the treated p-type silicon surface produced by successively larger range scans at (+3 V, 0.1 nA). x-range=3.0 μm, z-range=200 Å.

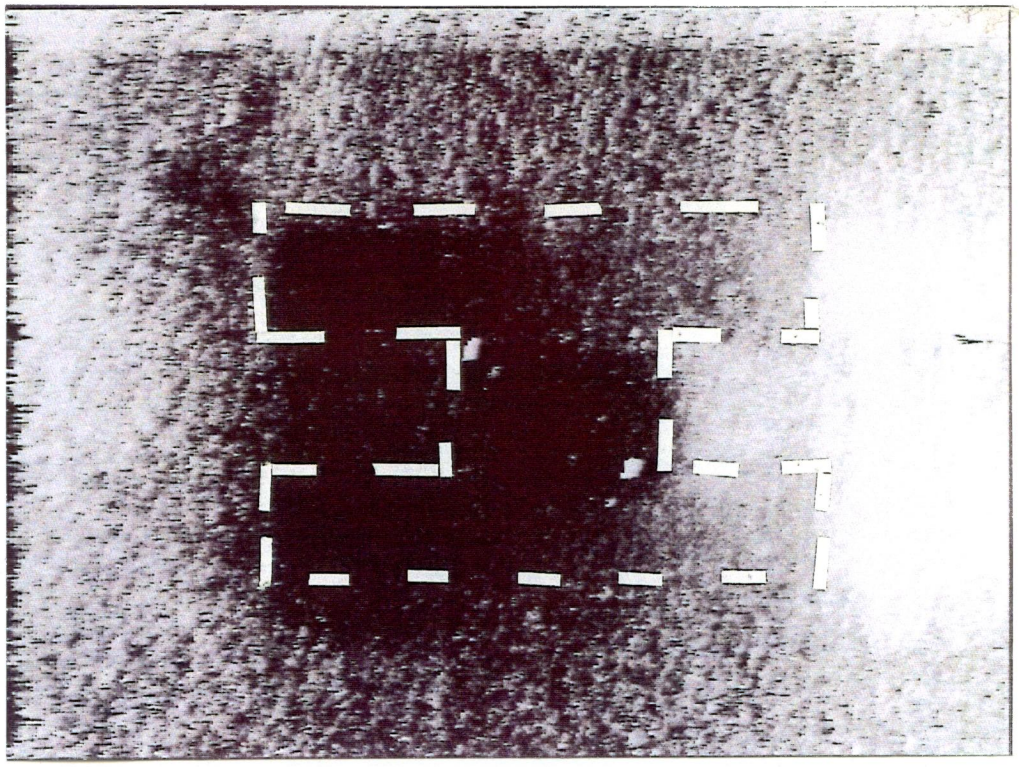

Fig. 3.6. Sideways 'H' pattern on treated p-type silicon. The dark pattern was produced by scanning the selected areas at (+4 V, 0.1 nA). The scanning set point was switched to (+2 V, 0.1 nA) in the regions surrounding the 'H'. x-range=2.5 μm, z-range=50 Å.

a different area of the same p-type surface. The central square was written by scanning that area three times at a set point of (+4 V, 0.1 nA). The sides of the 'H' were written by scanning a larger square area three times at (+2V,0.1nA), switching to (+4V,0.1nA) at the top and bottom of regions of the scan. Due to hysteresis in the piezo tube response (see §2.3), the area to the right of the resulting dark pattern appears saturated white in the image, and the left half of the pattern is darker than the right half.

Fig. 3.7 is a scan taken on an n-type region, the substrate of a sample on which a Si/Ge multilayer structure (§5.2) was grown. Successive scans on the substrate sometimes resulted in the appearance of tip images, as in this example, which had been scanned 3 times at (+3 V, 0.1 nA). Further scanning resulted in more tip images until the whole surface was covered. This effect, which suggests that the tunneling process is producing

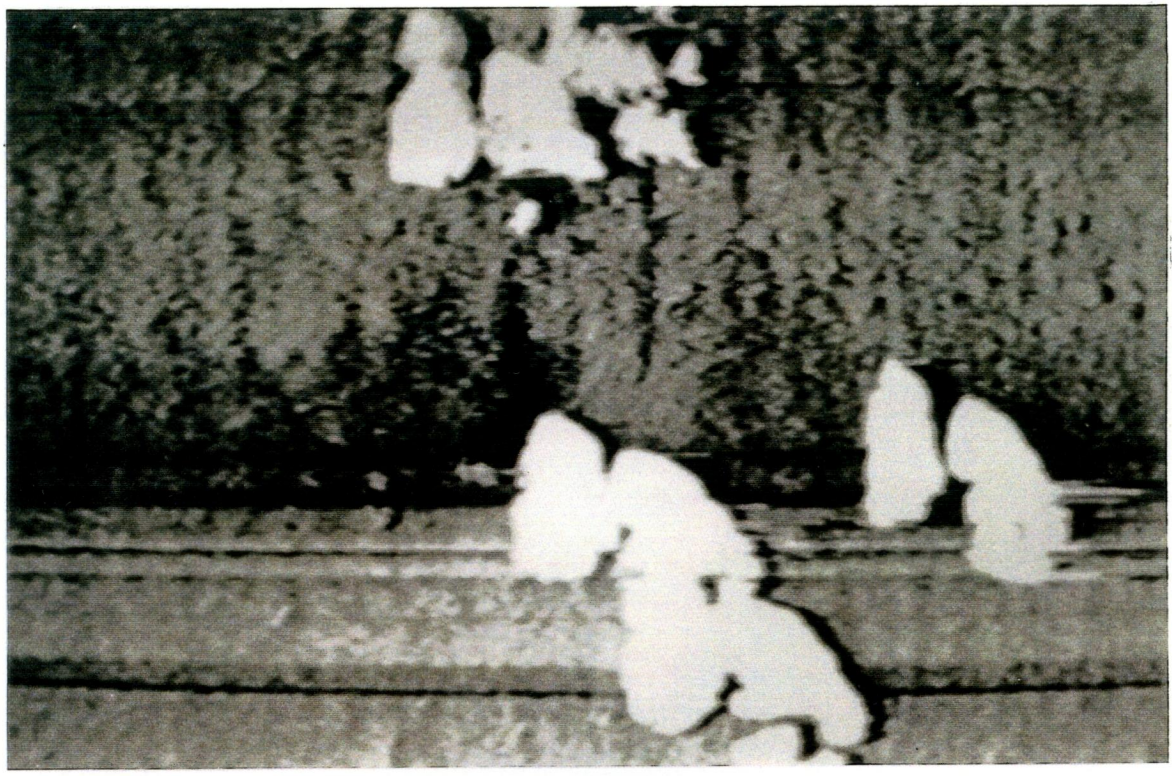

Fig. 3.7. Surface roughening on n-type silicon, induced during three successive scans at (+3 V, 0.1 nA). The roughening has produced four sharp features which image the tip. The horizontal lines are due to creep in the piezo tube (see Fig. 2.4). x-range=2.0 μm, z-range=80 Å.

sharp points on the surface, was not observed on the p-type capping layer grown above the Si/Ge multilayers. Also, the effect observed on the p-type substrates described above was not observed on these n-type substrates.

3.3. Gallium Arsenide

The GaAs-AlGaAs epilayers imaged in these experiments are grown on semi-insulating and conductive n-type (100)-oriented GaAs substrates. The dopant concentration of the conductive substrates is $2x10^{18}$ cm^{-3}.

Attempts to image the freshly cleaved GaAs samples without chemical passivation were unsuccessful, due to oxidation of the cleaved surface. As with the untreated silicon surfaces, imaging often became impossible within a few hours of imaging, perhaps due to the build up of oxide picked up by the tip.

3.3a. Imaging on Unpassivated GaAs Surfaces - Oxide Desorption Study

Some success was achieved in imaging the polished (100) substrate surfaces following a 5 minute etch in 3M HCl to remove the native oxide. This was followed by a rinse in DI H_2O and nitrogen blow off. No further chemical treatments were performed to passivate the surface against oxidation. This procedure did not work consistently, however, and always produced a rough surface.

The HCl treatment was used to prepare samples for imaging in an STM study of roughness induced by oxide desorption on GaAs substrates. The thermal desorption of a protective oxide is the final cleaning step for the GaAs substrates, prior to epitaxy.[29] This oxide is grown by exposing the wafer to ozone in an RF plasma and is desorbed in the (UHV) MBE growth chamber by radiative heating of the substrate. The desorption results in roughening of the surface, which can be detected by in-situ optical monitoring of the

substrate.[30] In order to investigate the nature of this roughenning, STM images were acquired on the (100) surface after desorption. These were compared to images obtained on polished substrates which had not undergone the MBE cleaning procedure.

Figs. 3.8 shows images acquired on (a) a polished GaAs substrate and (b) a substrate following desorption of an oxide grown by a 20 minute exposure to ozone. It was necessary to scan at slow speeds (8 minutes/image), positive tip bias (+1 V typically), and small tunneling currents (0.2 nA). Both of these images were acquired reproducibly for three successive scans of the surface. The criss-crossing lines on the polished substrate (a) may be polishing scratches. The surface roughness in this image is about 50 Å. By contrast, the large features on the desorbed surface (b) have an associated topography of more than 500 Å. In particular, three large holes appear in this image. The surface density of these holes is in agreement with that of features observed on the same sample using a Nomarski phase-contrast optical microscope (roughly $0.3/\mu m^2$). Three-dimensional renderings of regions of these images appear in Fig. 3.9. The lateral and vertical scales in these renderings are in angstroms. Higher magnification images acquired on the polished and desorbed surfaces showed the roughness to be greater than 100 Å and comparable for both surfaces, for lateral ranges of about 200Å. Possibly this roughness on small scales results from the HCl etching.

Although the results above were acquired during stable imaging, many of the images were unstable and noisy. In general it was found that reproducible images could not be obtained for more than an hour following the HCl etch, due to oxidation of the surface. However, a passivation step involving the solution used on the freshly cleaved surfaces as discussed below has been shown to permit stable imaging of the etched surfaces.[17]

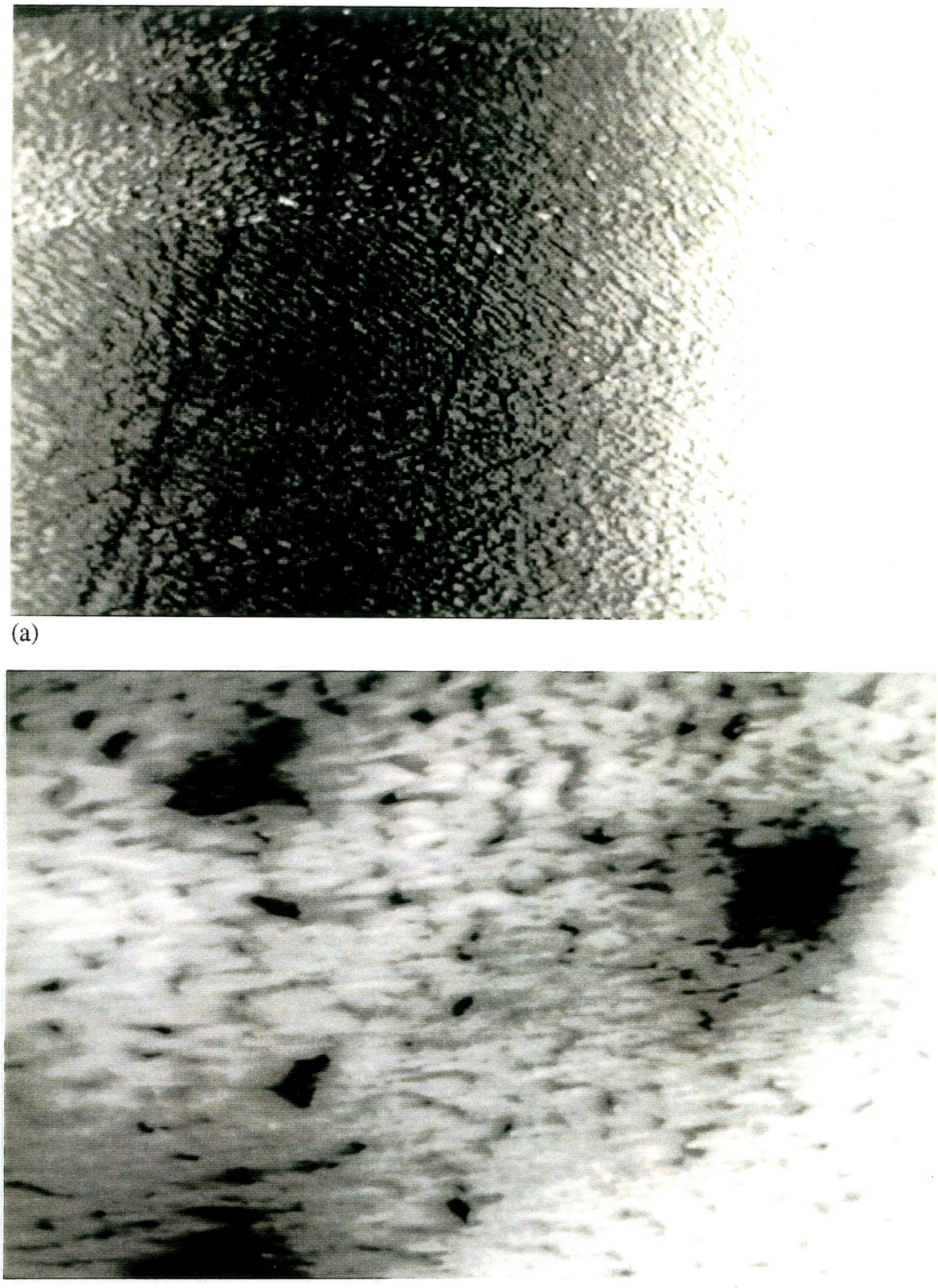

(a)

(b)

Fig. 3.8. STM images of (a) a polished (100) GaAs substrate and (b) a (100) substrate following oxide desorption as described in the text. The desorption produces large holes spaced apart by about 1 μm. x-range=2.7 μm for both images.

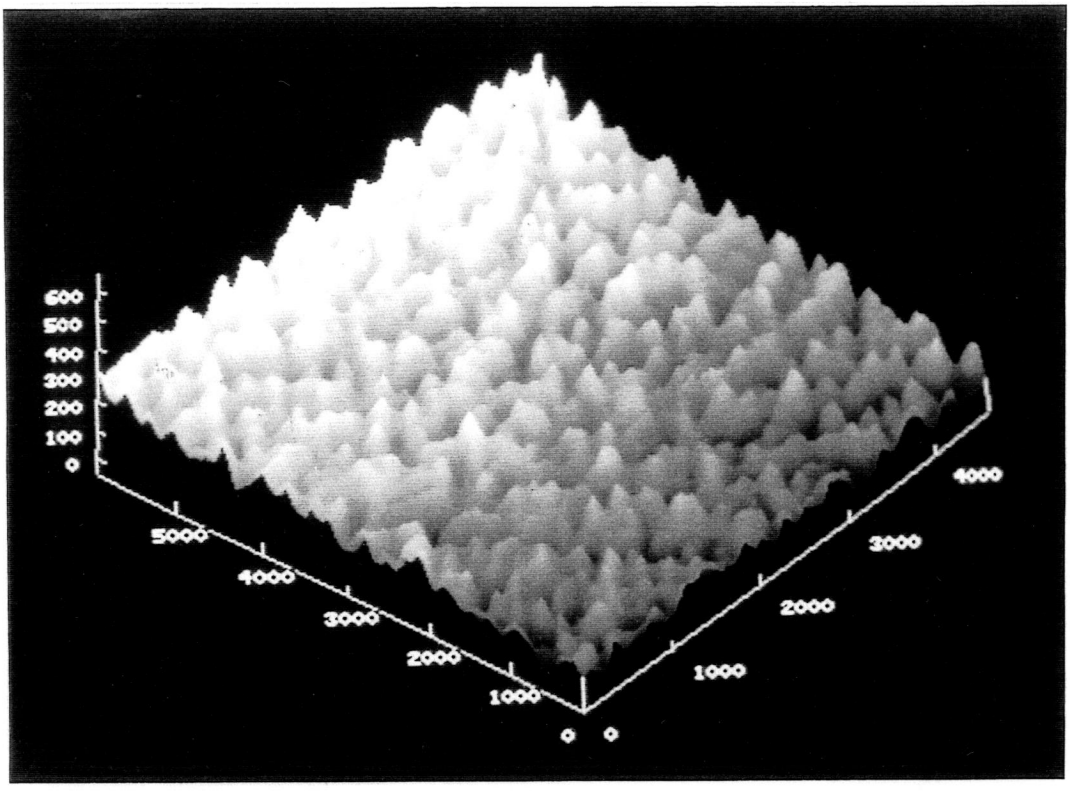

(a)

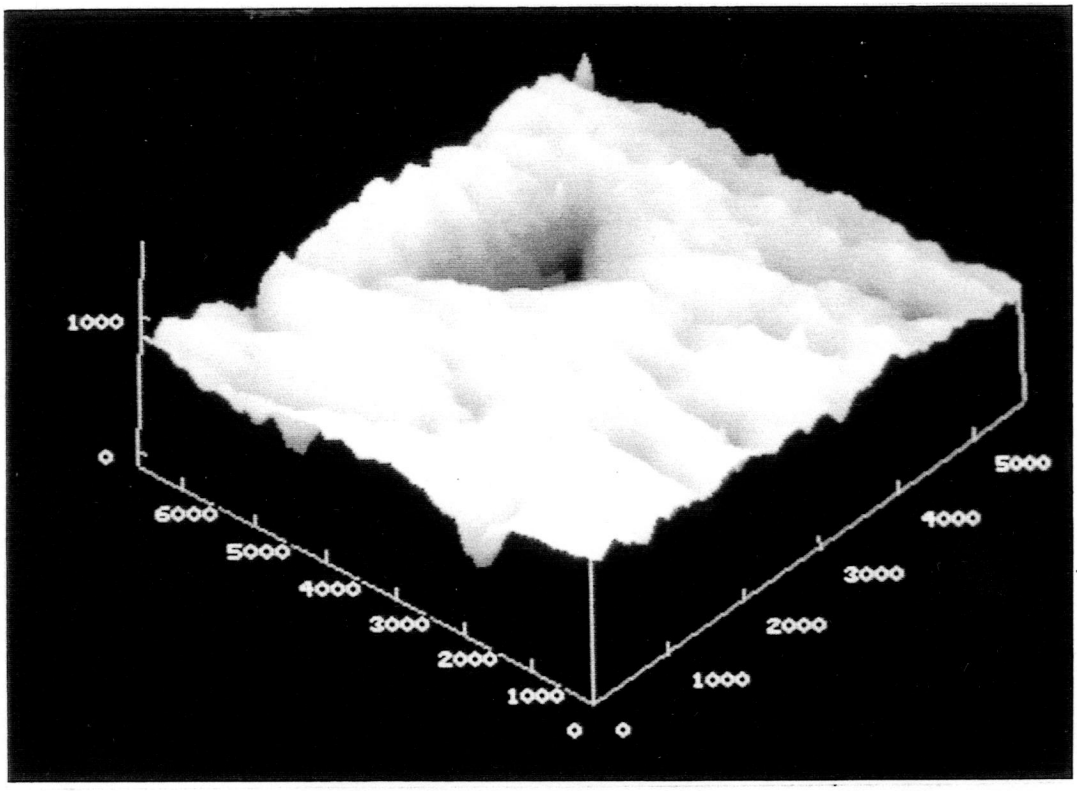

(b)

Fig. 3.9. Three-dimensional renderings of (a) polished surface and (b) desorbed surface, from portions of the images in Fig. 3.8. The hole in (b) corresponds to the large feature near the bottom left corner of Fig. 3.8b. Both the lateral and vertical scales are in angstroms.

3.3b. Surface Passivation Procedure

Due to its compound nature, the GaAs surface is much more difficult to passivate than silicon. Wet-chemical passivation treatments involving sulfide-based solutions have been investigated for purposes of device processing.[31] These treatments are believed to form a sulfur-terminated surface on polished (100) GaAs surfaces.[32,33] Accordingly, attempts were made to prepare samples for imaging by dipping the freshly cleaved (110) surfaces in Na_2S solution, followed by an H_2O rinse and nitrogen blow dry. However, this treatment did not permit stable imaging. It is possible that the tunneling process damages the insulating passivation layer, either because the layer is unstable or because it is thick enough that it is in mechanical contact with the the probe during scanning.

It has been shown[17] that stable STM imaging of GaAs is possible using a treatment in a 1g/20mL/60mL $P_2S_5/(NH_4)_2S/H_2O$ solution, heated to over 50°C. This procedure is believed to remove the surface arsenic atoms and leave a stable GaO termination.[17] Following this method, the freshly cleaved samples were quickly dipped into the heated solution (60°C) for 30 to 60 seconds, rinsed in DI water (5 min.) and blown dry with nitrogen. Stable imaging was achieved for up to 3 days on freshly-cleaved samples, following the P_2S_5 treatment.

Fig. 3.10 is an image taken in air, at a tunneling set point of (+4 V, 0.1 nA), 15 hours after this chemical passivation treatment. The scan is on the n-type substrate of a sample on which epitaxial layers had been grown. The surface roughness is less than 30 Å. The image quality did not deteriorate noticeably with repeated scanning over the same area, and stable images were obtained on this sample even after 30 hours exposure to room air. The stability and longevity of samples prepared in this way varied among samples, and appear to be strongly dependent on the quality of the cleave. It was found that the passivating solution, which is typically prepared in 32 mL quantities, generally

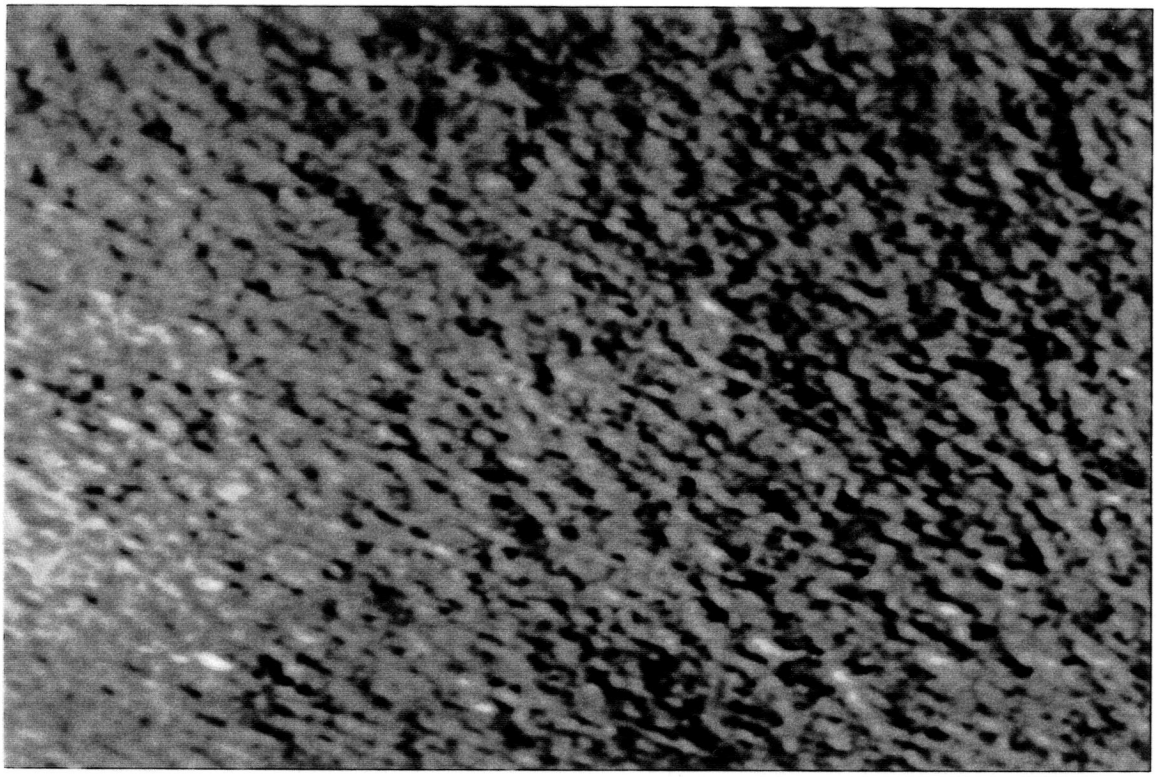

Fig. 3.10. STM image of a (110) n-type GaAs surface which had been passivated in P_2S_5 solution. The surface imaged stably after more than 30 hours exposure to air. x-range=500 nm, z-range=50 Å.

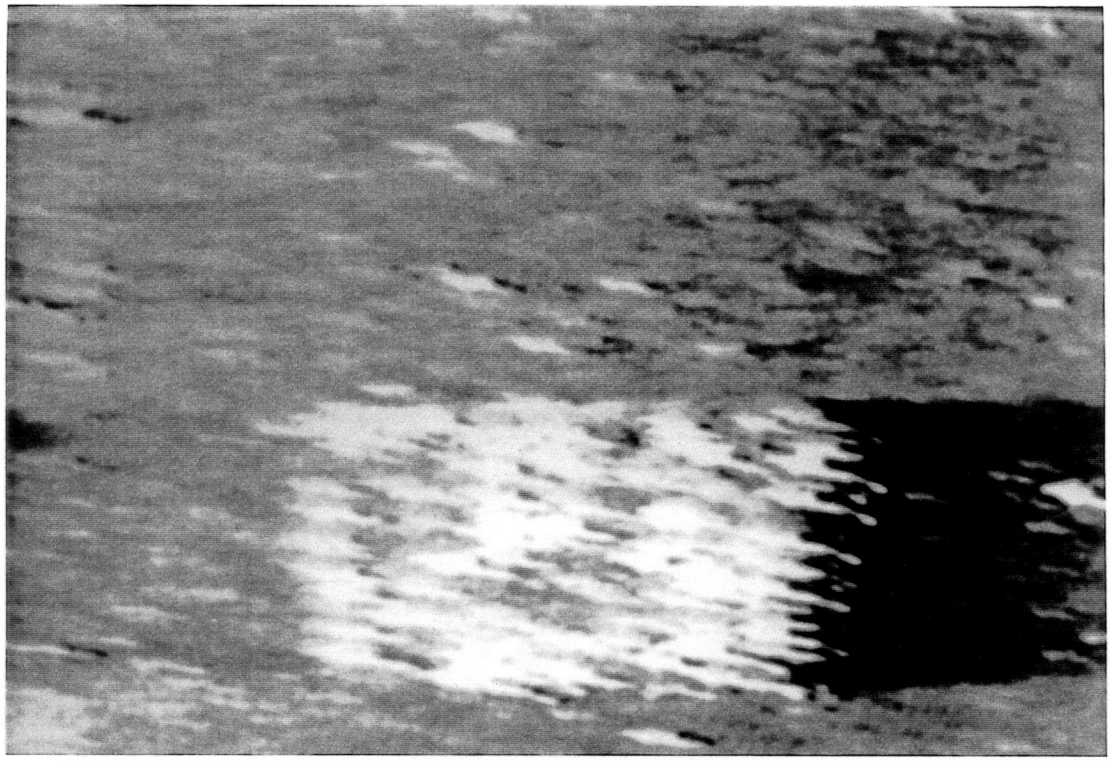

Fig. 3.11. Image acquired on a treated n-type surface, following a previous smaller scale scan which resulted in the formation of sharp points. The dark area on the right is due to hysteresis in the piezo tube. x-range=1.5 μm, z-range=25Å.

becomes ineffective after storing for more than two days in a stoppered volumetric pyrex flask. The solution turns from a straw-yellow to a dark, orange-yellow color after this time, possibly due to the formation of polysulfides.

3.3c. Tunneling-Induced Surface Modification

As in the case of silicon, damage due to mechanical tip-surface interaction was minimized by appropriate choice of scanning voltage and current, as discussed in §3.1. Nevertheless, surface modification in the form of sharp points was sometimes observed while scanning on the n-type substrates, or in n-type regions of the grown layers. As with silicon, this damage was found to increase with exposure to tunnel current and varied in extent among samples. By contrast, no noticeable surface modification occurred during repeated scans on p-type material.

Fig. 3.11 shows an image taken on an n-type substrate, following a smaller scale scan at the same set point. The surface had been prepared in the same way as that in Fig. 3.10 and was imaged at the same tunneling set point. The image acquisition time was 8 minutes for both the small scale scan and the larger scale scan, which means that the smaller area has substantially higher exposure per unit area to the tunneling current. In contrast with the smooth surface in Fig. 3.10, the previously scanned area appears to be covered with sharp points, resulting in identical tip images.

Fig. 3.12 shows two successive scans taken on a 16-period GaAs/AlGaAs multilayer structure. The first 8 periods of the superlattice are n-type and the remaining 8 periods are p-type. To the left of the structure is the semi-insulating substrate on which the epilayer was grown. The material to the right of the multilayers is n-type GaAs. Note that the n-type regions, both in the superlattice and in adjacent n-layer, are covered with sharp points. The density of the points increases during the next scan. By contrast, the p-type material in the superlattice is essentially undamaged by scanning. This preferential

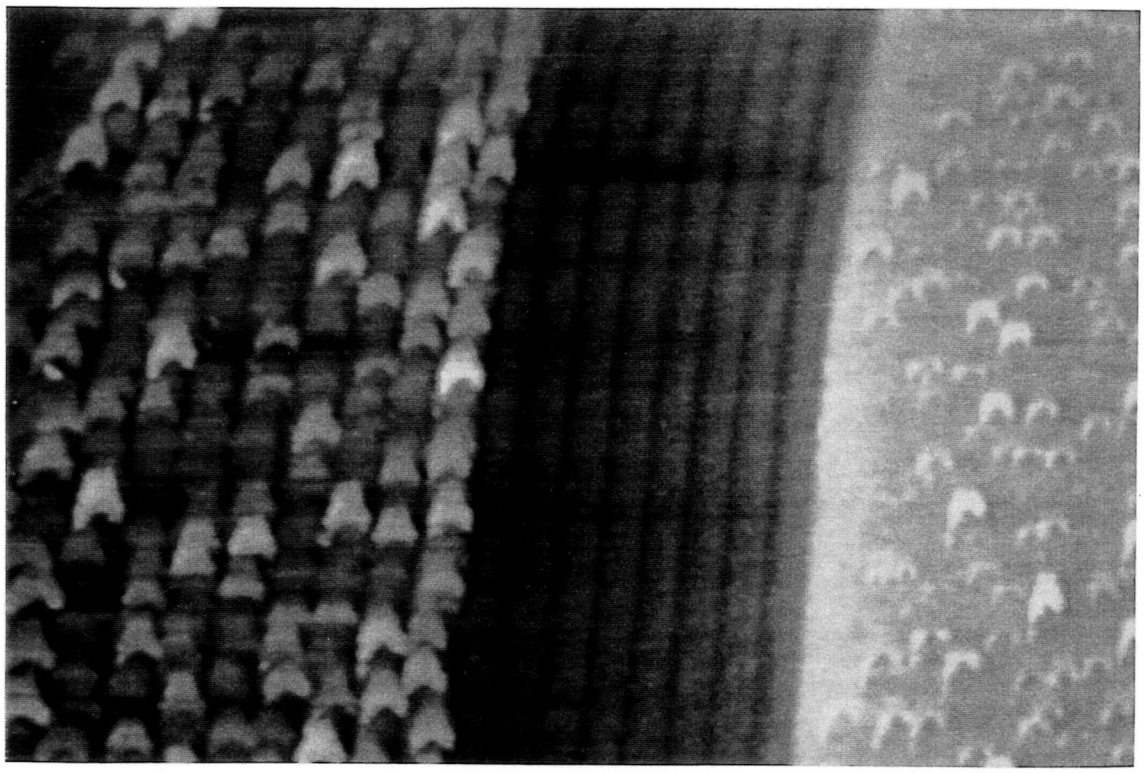

(a)

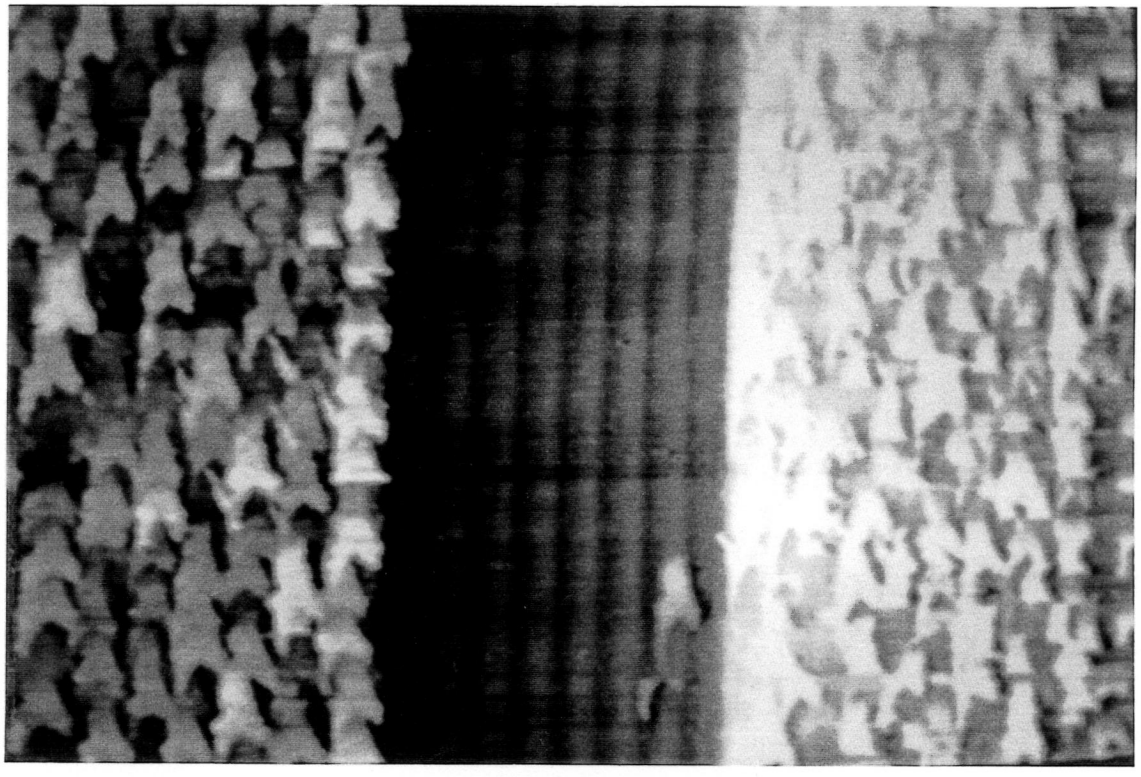

(b)

Fig. 3.12. Preferential roughening of n-type material during two successive scans on a structure consisting of a p-type layer (middle dark band) between two n-type regions. No significant surface modification of p-type material was observed during constant current scans. x-range=1.5 μm, z-range= 30 Å.

roughening of n-type material was observed on many occasions, but the p-type material seemed to remain smooth. One explanation of this effect is that the roughening is caused by oxidation of the surface, which is presumably enhanced by the tunneling process. The surface Fermi level in the n-type material will be higher than the surface Fermi level in the p-type material by almost the full band gap (1.4 eV) in the absence of surface states. In this case the p-type material has a correspondingly higher work function than the n-type material, and hence a higher affinity for electrons. Because the oxygen must remove electrons to bond with the gallium or arsenic atoms, this electron affinity represents a barrier to oxidation, which is significantly higher for oxidation of p-type material, and hence the p-type regions are likely to oxidize at a lower rate.

3.3d. Photoemission Spectroscopy of Chemically Treated (110) GaAs

In order to investigate the chemical passivation mechanism which permits the stable imaging of GaAs in air, photoemission spectroscopy[5] (PES) of the Ga and As core level chemical shifts was performed on the cleaved (110) GaAs surfaces. Semi-insulating substrates, which are slightly thicker (0.8mm) than the conductive substrates, were used to improve the measurement sensitivity. Treatments with two chemical solutions were investigated: $P_2S_5/(NH_4)_2S$, and $(NH_4)_2S$. Both treatments were identical to that described previously (§3.2b), with the single exception that no P_2S_5 was added to the passivating solution for the latter treatment. An untreated sample cleaved from the same substrate was used for comparison.

Figs. 3.13 and 3.14 show X-ray photoemission (XPS) measurements[34] of the cleaved surfaces obtained with a Leybold MAX200 spectrometer, using an Al K_α x-ray source ($h\nu$=1486.6 eV). All three samples had been exposed to room air for about 1 hour following surface preparation before being loaded into the spectrometer vacuum chamber ($6x10^{-9}$ Torr operating pressure). The measurements shown correspond to the As2p and

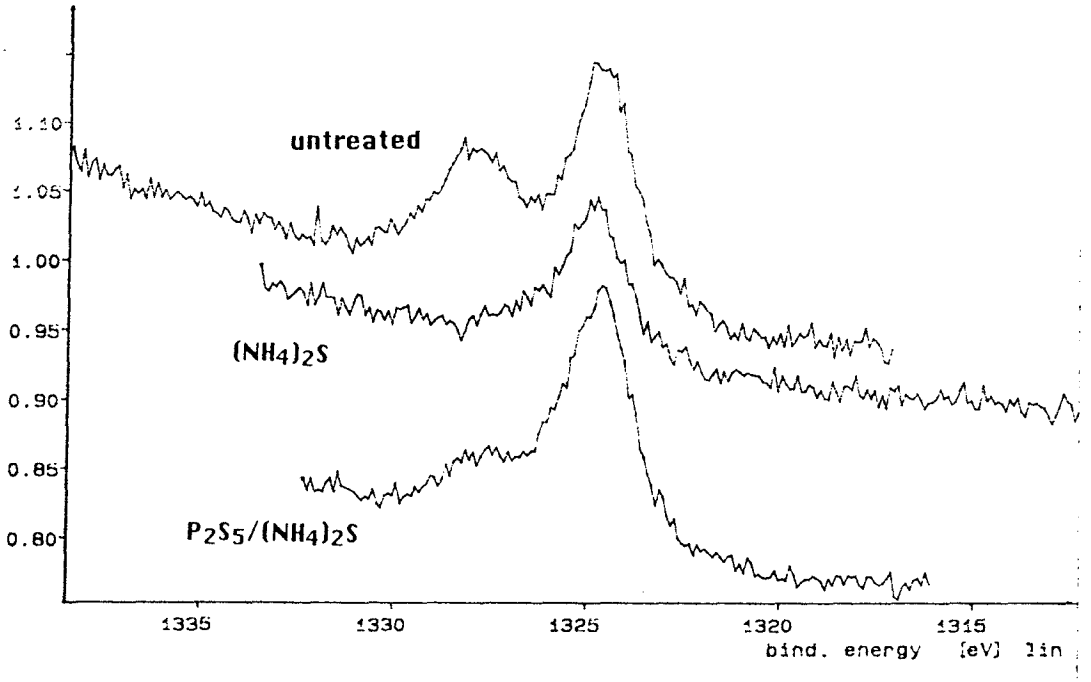

Fig. 3.13. XPS (arbitrary units) at the binding energy of the As2p core level for cleaved (110) GaAs surfaces. Results for an untreated (oxidized) cleave are shown for comparison with the chemically treated surfaces. The magnitudes of the chemically shifted components (higher binding energy), relative to the magnitudes of the bulk peaks indicate that relatively little arsenic oxide is present on the treated surfaces.

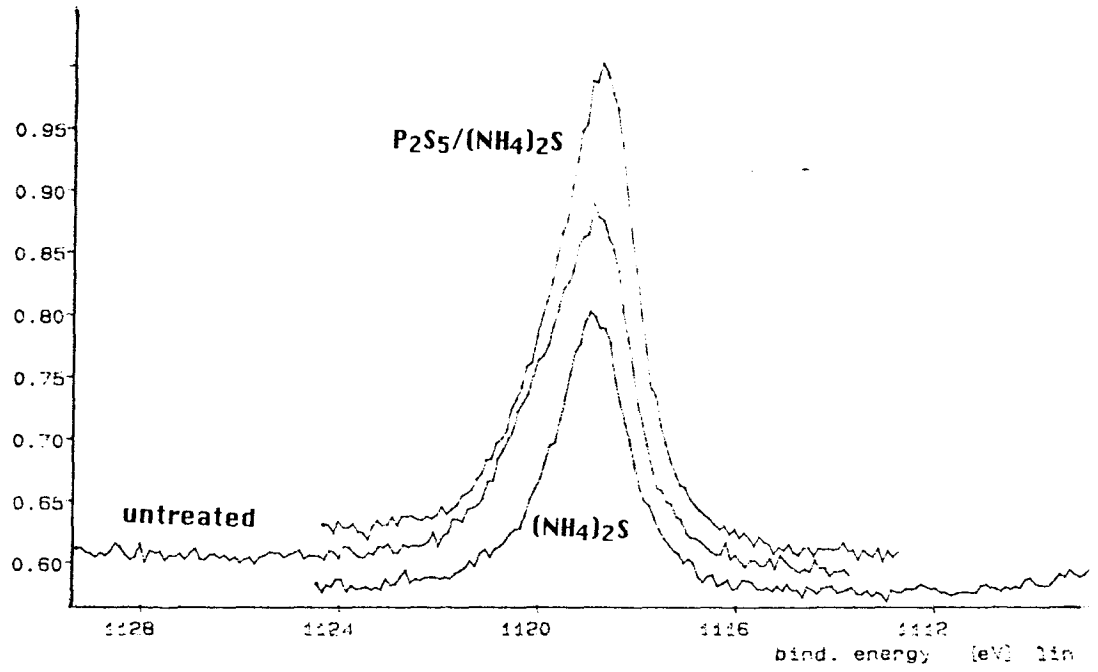

Fig. 3.14. XPS results for the Ga2p core level for the same three samples in Fig. 3.13 (arbitrary units). The untreated and P_2S_5-treated spectra are asymmetric due to oxidation of the Ga whereas the treatment without P_2S_5 has resulted in a symmetric peak.

Ga2p core level binding energies. The higher binding energy of the 2p levels makes these spectra more sensitive to surface composition than those of the 3d levels: photoelectrons ejected from the 2p levels have a lower kinetic energy and hence a smaller escape depth than those ejected from the 3d levels. For the As2p core level, chemical shifts of +3 eV and +2 eV respectively are associated with bonding to oxygen and sulfur.[35] The relative intensities of the spectral peaks corresponding to the chemically shifted (higher binding energy) and the unshifted As2p binding energies show that the P_2S_5-treated surface has significantly less arsenic oxide than the untreated cleave. The chemical shifts associated with the formation of gallium oxide and sulfide are small (+1.3 eV and +0.6 eV respectively[35]), and result in an asymmetric peak, rather than distinct peaks, at the Ga2p binding energy. The Ga2p peak corresponding to the P_2S_5-treated surface appears more symmetric than the untreated peak, indicating that the gallium oxide/sulfide content is less than the gallium oxide content of the untreated surface. Better resolution is needed to determine if the asymmetry in the P_2S_5-treated peak is due to sulfide or oxide, however.

Analysis of the spectra obtained on the surface treated in $(NH_4)_2S$ solution (with no P_2S_5 added) reveals that no detectable oxidation of either the arsenic or gallium has occurred: the Ga2p peak is symmetric, and no oxide peak is detected in the As2p spectrum. A slight shoulder on the As2p peak of the $(NH_4)_2S$-treated surface, corresponding to the sulfur chemical shift, is barely detectable above the background. One interpretation is that a thin sulfur passivation layer has inhibited the oxidation of this surface. Auger emission spectroscopy was also performed[34] on surfaces treated in $(NH_4)_2S$ solution, with and without P_2S_5 added, and confirmed the presence of sulfur in both cases. In these measurements, which were made with the same spectrometer as the XPS, sensitivity was improved by stacking several cleaved samples together after the treatment, to increase the edge area.

To further clarify the XPS results, PES using synchrotron radiation was performed[36] on the $P_2S_5/(NH_4)_2S$-treated surface. The low energy ($h\nu$=100 eV) radiation

used makes these measurements sensitive to chemical composition extending only 6 Å below the surface as opposed to about 20 Å below the surface for the XPS data (hν=1.4 keV) above, based on the universal curve[37] of electron mean free path. The samples had been exposed to air for three days before the measurements, which were carried out at the University of Wisconsin. The chemical shifts associated with bonding to oxygen and to sulfur respectively are +3 eV and +1.5-2 eV for the As3d core level and +1.3 eV and +0.6 eV for the Ga3d core level.[38] Overview spectra which included the Ga3d and As3d peaks in the same scan were taken on the treated and untreated surfaces. Based on these scans, the ratios of the intensities of the bulk Ga3d and As3d peaks are the same within 10% for both surfaces. Higher resolution scans at the binding energies of each core level were taken individually (Figs 3.15 and 3.16). The fit to each spectrum represents a sum of two Gaussians, separated by the energy shown in the figure. The As3d peak (Fig. 3.15) reveals that for the untreated surface, the arsenic has oxidized significantly more than the arsenic on the P_2S_5-treated sample: for the treated sample, the intensity of the bulk As3d peak is about the same as the chemically shifted component; for the untreated sample the chemically shifted component is approximately twice as intense as the bulk peak. By contrast, the relative amplitudes of the chemically shifted and bulk Ga3d peaks (Fig. 3.16) are similar for both the treated and untreated samples. These results are consistent with the XPS results above, and with previous XPS results[17] which indicate that the chemical treatment selectively removes arsenic atoms from the surface. No peaks associated with the sulfur chemical shift are observed for Ga3d or As3d, although the presence of the oxide obscures the smaller sulfur chemical shift. Possibly the passivation layer had deteriorated, permitting oxidation to occur, or the passivation treatment produces primarily a surface oxide rather than a sulfide. The deterioration interpretation is consistent with the observation that STM imaging of the treated surfaces became unstable within a few days of treatment.

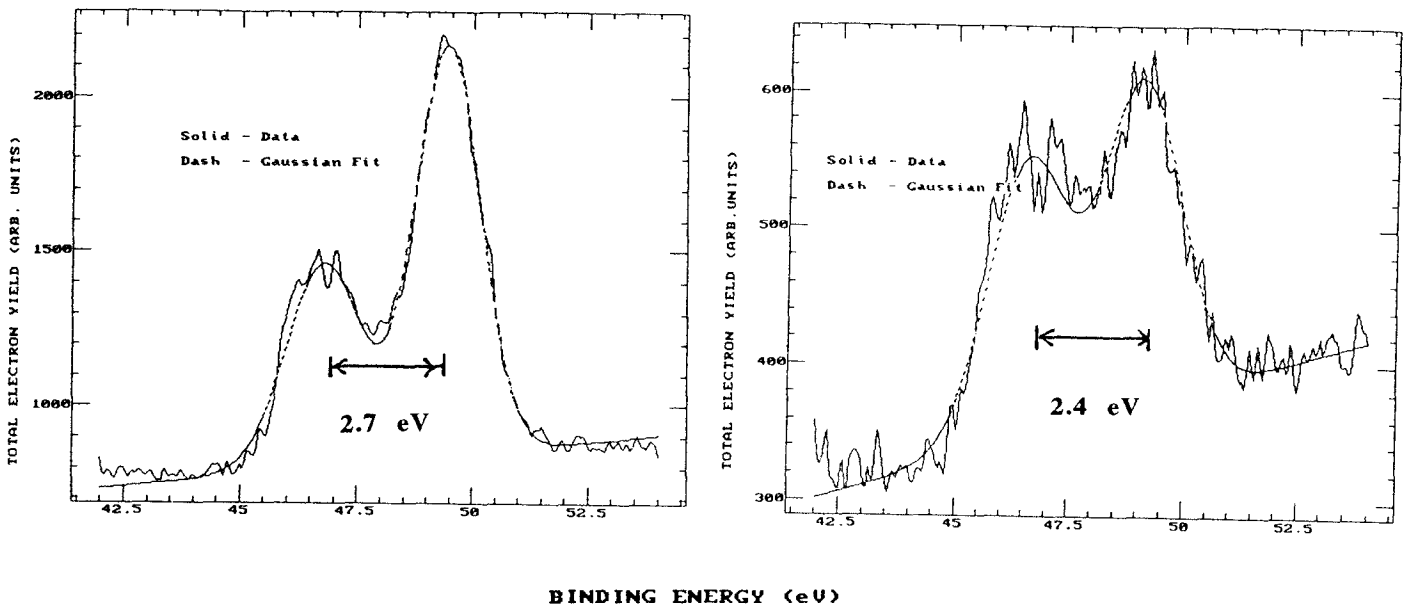

Fig. 3.15. Raw data from PES measurements of the As3d core level for an untreated cleave (a) and a cleaved surface passivated in P_2S_5 soloution (b). The peak for the treated cleave is smaller and has a considerably reduced chemically shifted (higher binding energy) component than the untreated cleave. Both samples had been exposed to air for 3 days after preparation.

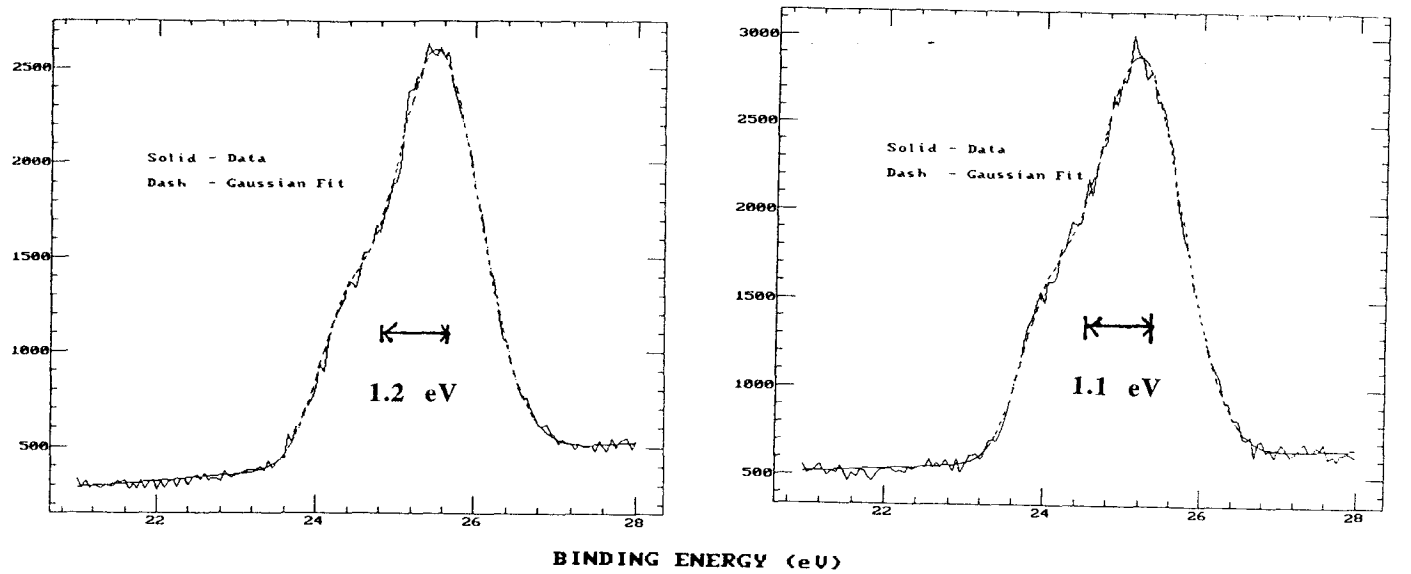

Fig. 3.16. PES of the Ga3d core level. The untreated (a) and treated (b) peaks in this raw data are of nearly equal intensity and both have large chemically shifted components (higher binding energy), corresponding to oxidation of the Ga.

Note that oxygen is present in both passivating solutions, owing to the dilution with DI H_2O. The $(NH_4)_2S$ treatment seems to inhibit oxidation of both arsenic and gallium, apparently by formation of a thin sulfide layer. By contrast, The XPS and synchrotron PES results above suggest that the P_2S_5 treatment used in preparing the cleaved surfaces for imaging selectively removes the surface arsenic. Selective removal of arsenic atoms may be a key factor in producing a surface stable against imaging in air: Arsenic oxides are more unstable than gallium oxide, in the sense that they evaporate at a lower temperature than gallium oxide[29] and assume various chemical stoichiometries such as AsO and As_2O_3. Possibly the arsenic oxides are removed or chemically altered by the tunneling process, resulting in surface damage and a noisy current signal.

4. Tip Effects

Even when the chemical treatments had resulted in a stable surface, resistant to modification due to tunneling, imaging was sometimes inconsistent, due to irregular tip geometry or mechanical instability of the tunneling probe. In order to interpret the STM images, it is necessary to evaluate how these non-ideal tip structures affect the data. Various kinds of tip artifacts were observed and are discussed below.

4.1. Tip Instabilities

Images acquired on the semiconductor surfaces treated as previously described were sometimes noisy, with large apparent z-range, as if the surfaces were very rough. After a new tip was installed however, the images were often immediately improved, revealing a stable and smooth sample surface. It is most likely that the effect is due to some mechanical instability of the tip. This instability might arise from insulating adsorbates, left on the end of the tip as it was prepared, or picked up from the sample while scanning. Mechanical contact of this insulating material with the sample surface would result in a noisy current signal. As the scanning continued, adsorbates swept off the tip would be replenished by insulating debris from the damaged passivation layer. The same effect was not observed while scanning on graphite or gold samples, which consistently imaged stably. Presumably any tip adsorbates are removed during scanning of these more robust, oxide-free surfaces.

Fig. 4.1a shows an image of a cleaved silicon (110) surface, which had been passivated by dipping in NH_4F. The image is noisy and suggests that the surface is rough. During acquisition of the next image, the image quality suddenly changed, and a larger scale scan was taken immediately, shown in Fig. 4.1b. Here, the white blob in the center

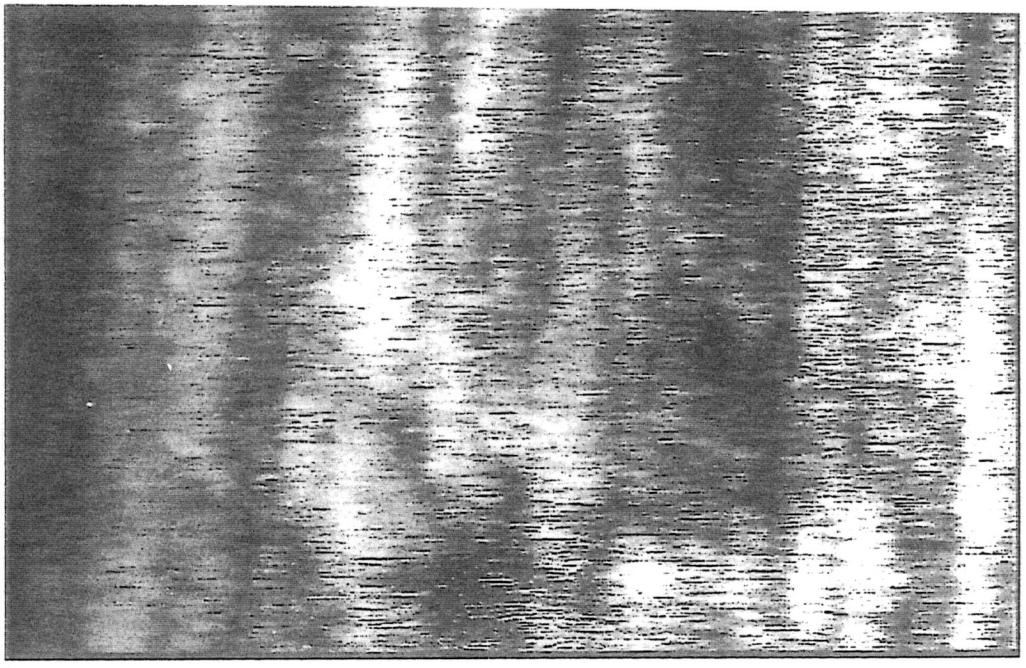

(a) x-range=250 nm, z-range=50 Å

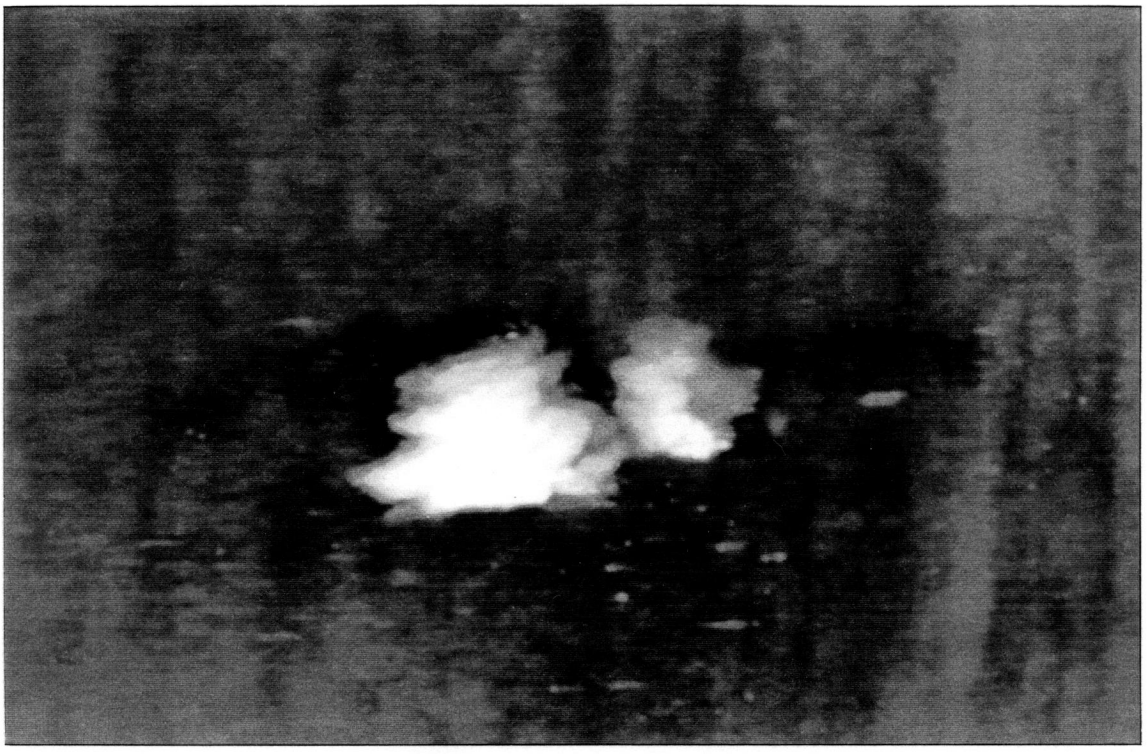

(b) x-range=500nm, z-range=100 Å

Fig. 4.1 Effect of mechanical tip stability on image quality. It is believed that the noisy imaging in (a) was caused by a mechanical instability in the tip, which was no longer present in (b). The irregular white feature in the centre of the second scan is possibly a metal fragment deposited by the tip during the change.

of the image is believed to be a tip fragment deposited on the surface. The image is no longer noisy and the surface appears smooth, probably because the remaining tip is mechanically stable. The dark circular area surrounding the tip fragment may be electronic contrast, since the deposition of metal could result in local pinning of the Fermi level[8] and the tunnel current is sensitive to the surface Fermi level position (see Chapter 6).

4.2. Tip Images

If features on the sample surface have a higher aspect ratio than that of the tip, those surface features will image the structure of the tip as it scans the surface. This effect is well known and has been observed on many different surfaces.[25,39] Careful consideration of the orientation of the tip images can sometimes provide information about the crystallographic orientation of the surface structures responsible.[39] Tip images are observed while imaging on the chemically treated semiconductor surfaces discussed in this work, as shown above (§3.2,§3.3). The tip images scale with scan range as would true surface features.

It is possible that the white blob in Fig. 4.1b is also a tip image, if the deposited fragment is sharper than the remaining tip. The spatial extent of the electronic contrast discussed in connection with this image should be comparable to the depletion width (see Chapter 6), which is roughly 80 nm for the dopant concentration of this sample ($1x10^{17}$ cm^{-3}), assuming the Fermi level is pinned midgap by the metal deposition. The radius of the dark region in the image is about 50 nm, although only about 10 nm is visible. An interpretation is that the small metal fragment responsible for the electronic contrast produces an image of the irregularly shaped tip, which partially obscures the circular depletion region.

4.3. Multiple Tips

Often the tunneling probe will consist of many sharp points, particularly in the case of probes prepared by mechanical shearing as shown in §2.2. If, while scanning, more than one of these tips is within tunneling range , the resulting image will be a sum of the contributions from each tip. The tunnel current is expected to be reduced by an order of magnitude for each angstrom increase in tip height (see Chapter 6). This result, and the low probability of two tips being at almost precisely the same separation (within 1 Å) means that multiple tips are rarely a concern for atomically flat surfaces. High relief surface features, however, will be imaged multiple times.

The steps of the atomically flat terraces on the graphite surface shown previously in Fig. 2.7 (§2.3) are each imaged twice, presumably due to a double tip. Note that the vertical separation of these tips must be less than 10 Å, the height of the smallest steps in the image. In Fig. 4.2, an image of a GaAs/AlGaAs superlattice is presented. The sample had been prepared as described above. The superlattice structure appears as alternating light and dark vertical bands in the image, and is imaged twice due to a double tip. From the image the lateral separation between the tips is estimated to be about 200 nm.

An image of another GaAs/AlGaAs superlattice appears in Fig. 4.3. At the top of the scan, the individual layers of GaAs (light bands) and AlGaAs (dark bands) are well resolved. Midway through the scan, however, the resolution is suddenly lost, clearly due to a change in the tunneling probe. Several tip images are present after the change, and from these we see that the probe is in fact a double tip. From these tip images, the lateral tip separation is seen to be almost exactly the same as the layer thickness (20nm). The thin dark lines in the remainder of the scan (after the change in the probe), correspond to the brief instances when both tips are simultaneously over the AlGaAs regions.

Fig.4.4 shows two successive scans over the same area of a portion of a GaAs/AlGaAs superlattice. Again, the AlGaAs layers appear narrower than the GaAs

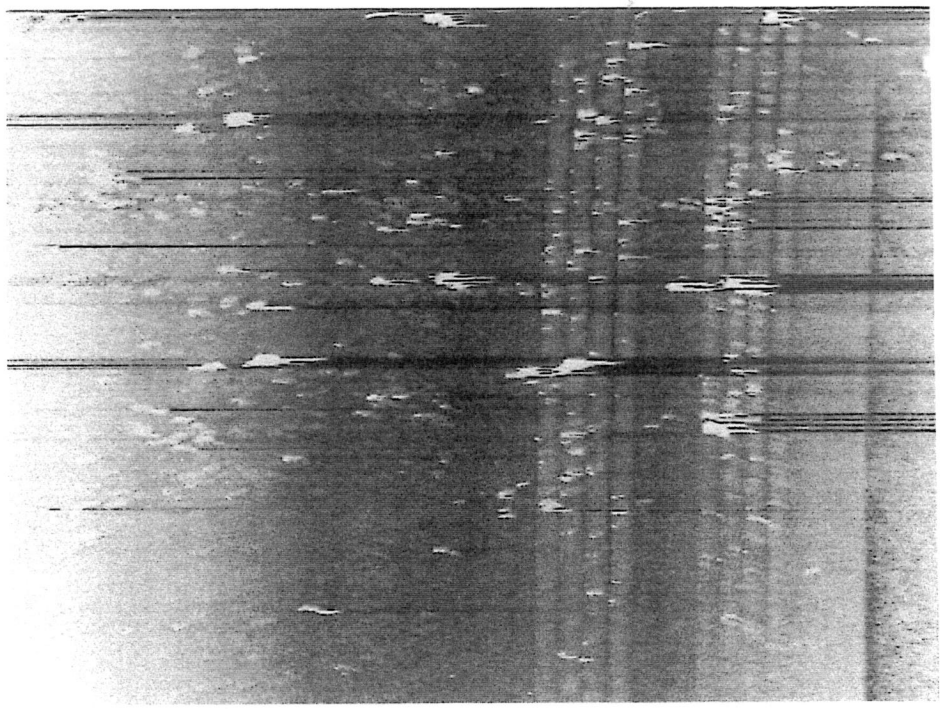

Fig. 4.2. Double-tip image of a GaAs/AlGaAs multilayer structure consisting of four GaAs layers (bright bands) and three AlGaAs layers (dark bands). The entire structure is imaged by two tips on the same probe, separated laterally by 200nm. x-range=2 μm, z-range=55 Å.

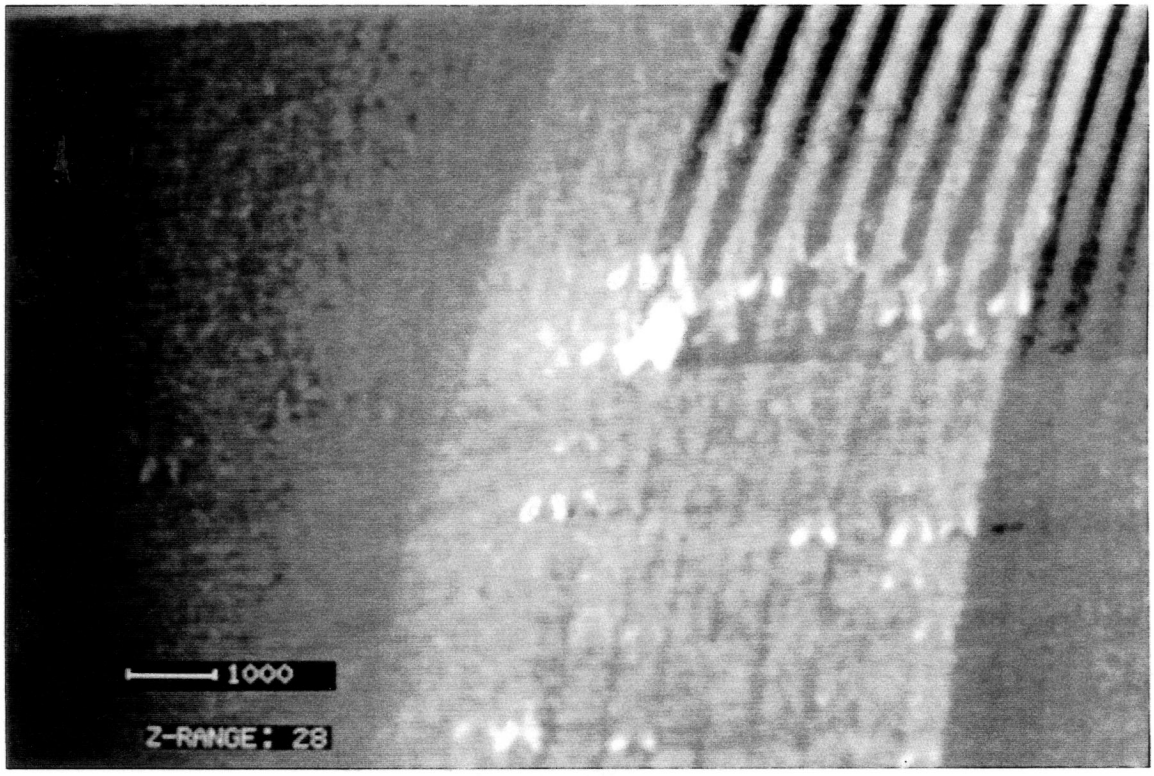

Fig. 4.3. Change in tip geometry midway through a scan on a GaAs/AlGaAs multilayer structure. The tip images (bright dots) reveal that the change has produced a double tip, in which the lateral separation of the tips is nearly identical to the layer thickness (20nm). x-range=1.5 μm, z-range=28 Å.

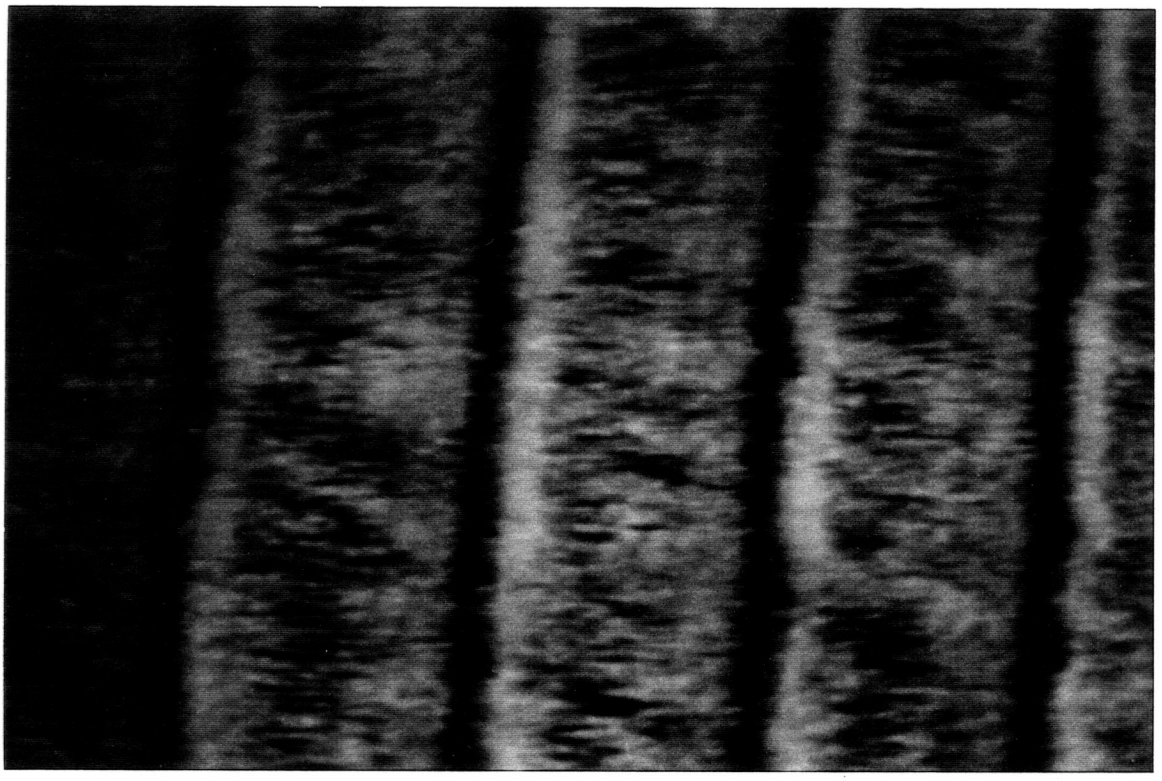

(a)

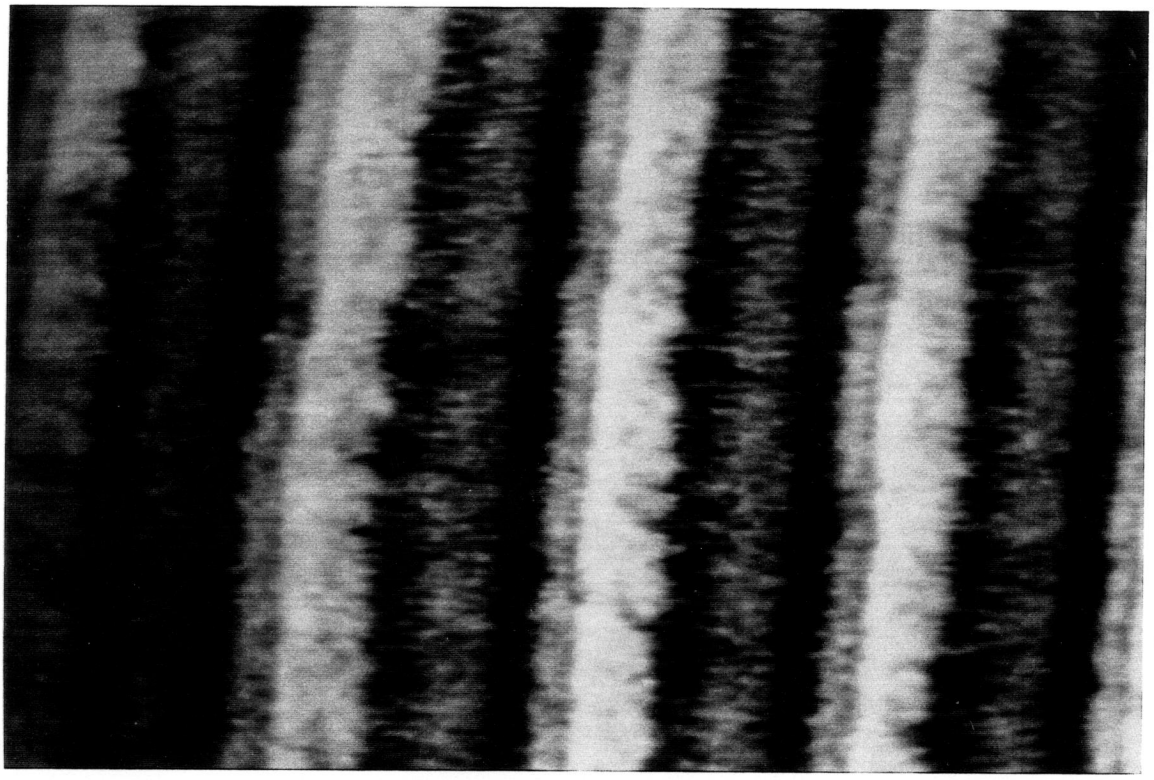

(b)

Fig. 4.4. Change in tip structure between two successive scans of the same portion of a GaAs/AlGaAs superlattice. The contrast in the image is enhanced (b) after the change. x-range=270 nm, z-range=140 Å in both images.

layers in both images, probably due to multiple tips. The apparent topography of each of the layers changed identically in the second scan. This suggests that the higher GaAs layers are imaging the structure of the tip, which changed between the scans.

Clearly these multiple tip effects complicate the interpretation of the images, and of the spatial dependence of the IV characteristics obtained at selected locations in the epitaxial layers (§7.4). It is therefore necessary to ensure that multiple tips are not present, for example by comparing the layer thicknesses in the STM multilayer images with the thicknesses predicted by the MBE growth rate calibration or determined from SEM measurements. Alternatively, several measurements using different tips can be made, since tip artifacts will materialize as inconsistencies in the data.

5. Crossectional Imaging of Epitaxial Structures

5.1. Positioning of the Tunneling Probe

In the case of the samples imaged in cleaved crossection, the scanning direction is perpendicular to the polished surface, as shown in Fig. 5.1. The tip is positioned over the MBE grown layers by moving the sample using the mechanical translation device described previously (§2.1), until the layers are observed in the image. Often this procedure involves first locating the edge of the sample, evidenced by huge topographical contrast as the tip falls off the edge, and then moving the tip away from the edge by applying an appropriate voltage offset to the scanner electrodes. During sample translation it is necessary to either retract the tip using the piezolelectric tube or to back the sample off with the micrometer stage adjustment, to prevent tip crashes.

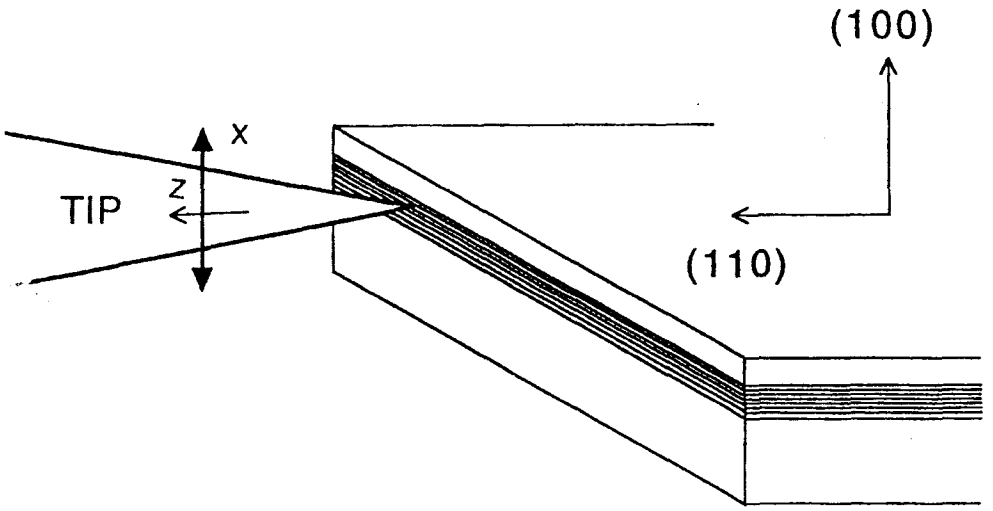

Fig. 5.1. Orientation of scanning probe and cleaved surface for crossectional measurements. The scanning direction is across the layers, perpendicular to the plane of the polished surface.

5.2. Imaging of Si/Ge Multilayers

Fig. 5.2 is a field-emission scanning electron microscope (SEM) micrograph of the epilayer shown schematically above it.[40] The multilayer structure consists of twenty, 5-period Si/Ge superlattices (5 nm wide), separated by 20 nm Si spacer layers, and appears as alternating light and dark bands in the SEM image. It is not clear from the micrograph which bands correspond to the Si layers and Ge-containing layers. The cleaved sample had not been chemically treated, so the contrast is not due to selective etching. Possibly the contrast is electronic in origin, due to the smaller band gap of the Ge. The individual Si and Ge layers in the superlattices are 0.5 nm thick, and are not resolved.

An STM image[41] of the same sample is shown in Fig.5.3. The surface had been passivated by an HF treatment and was imaged in air at a tunneling set point of (+1 V, 0.2 nA). The vertical contrast to the left of the multilayer was not present in all the samples, and might be associated with a topographic step at the interface between the substrate and the buffer layer, caused by the cleaving process. The p-type capping layer appears saturated black in the image, presumably because it had cleaved at a lower height. The 20-period multilayer is resolved in the centre of the image as a series of alternating light and dark bands. The bright bands are interpreted as the Ge-containing layers and the dark bands as the Si spacer layers, as discussed below. Contrary to this identification, the bright bands are wider than the dark bands, which is attributed to the finite aspect ratio of the tip: the side of the tip images the adjacent Ge-containing layer when the probe is positioned over a Si spacer layer. In higher magnification images, which failed to resolve the 0.5 nm layers, the bright bands appeared to be lined with white balls which limited the resolution. These might be tip images resulting either from tunneling-induced oxidation (§3.2b) or non-uniform etching by the HF (§3.2.a).

A scan line taken across the same multilayer structure on the same surface at a different location in the epilayer, is shown in Fig. 5.4. The cleavage plane of the epilayer

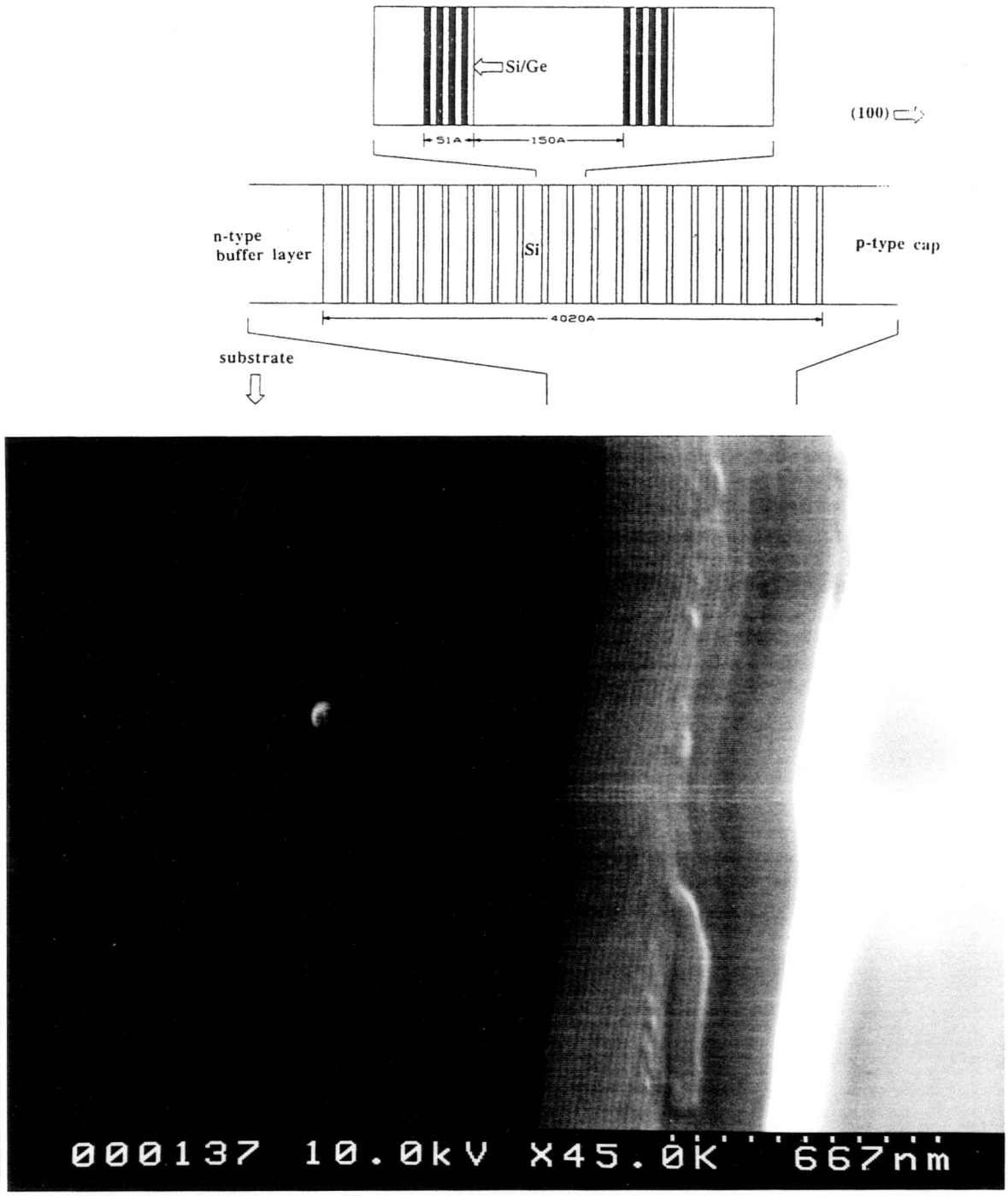

Fig. 5.2. Field emission SEM micrograph of a group of 20 Si/Ge superlattices.

Fig. 5.3. STM image of the epilayer containing the Si/Ge multilayers, showing a topographic step at the substrate/epilayer interface. The bright bands are interpreted as the Ge-containing layers. x-range=1.4 μm, z-range=350 Å.

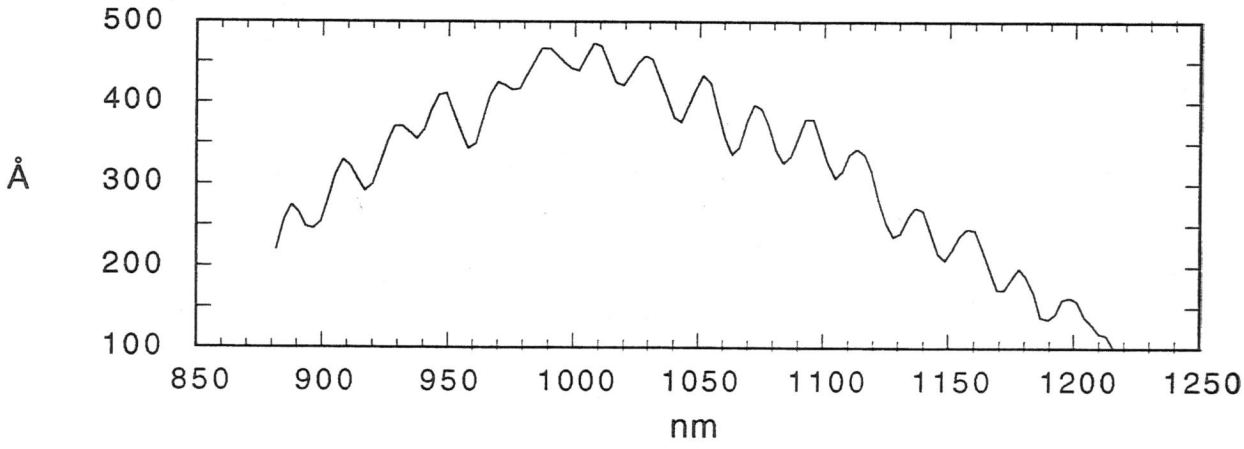

Fig. 5.4. Topographic scan line across the Si/Ge multilayers. The modulation associated with the multilayer periodicity is attributed to strain relaxation of the Ge-containing layers.

is not quite perpendicular to the probe tip, resulting in the 400 Å bulge in the scan line. The higher frequency modulation in the scan line is due to the multilayer topography. The magnitude of the topographic modulation is roughly 40 Å and is attributed to bulging of the compressively stressed Ge-containing layers at the cleavage surface. The equilibrium lattice constants of Ge and Si are 5.66 Å and 5.43 Å respectively. This lattice mismatch results in large compressive strrains in the Ge layers grown on the Si substrate.

Fig. 5.5 is a higher magnification image taken of the same multilayer structure. This sample was etched in NH_4F and imaged in nitrogen ambient. No tip images are present, consistent with smoother etching of this treatment over HF. However, the individual Si and Ge layers are still not resolved.

Another multilayer structure, consisting of four alternating periods of 40 nm silicon and $Si_{0.8}Ge_{0.2}$ alloy layers,[42] is shown in Fig. 5.6. This image was acquired in nitrogen ambient following a treatment in NH_4F. The multilayer structure is imaged more than

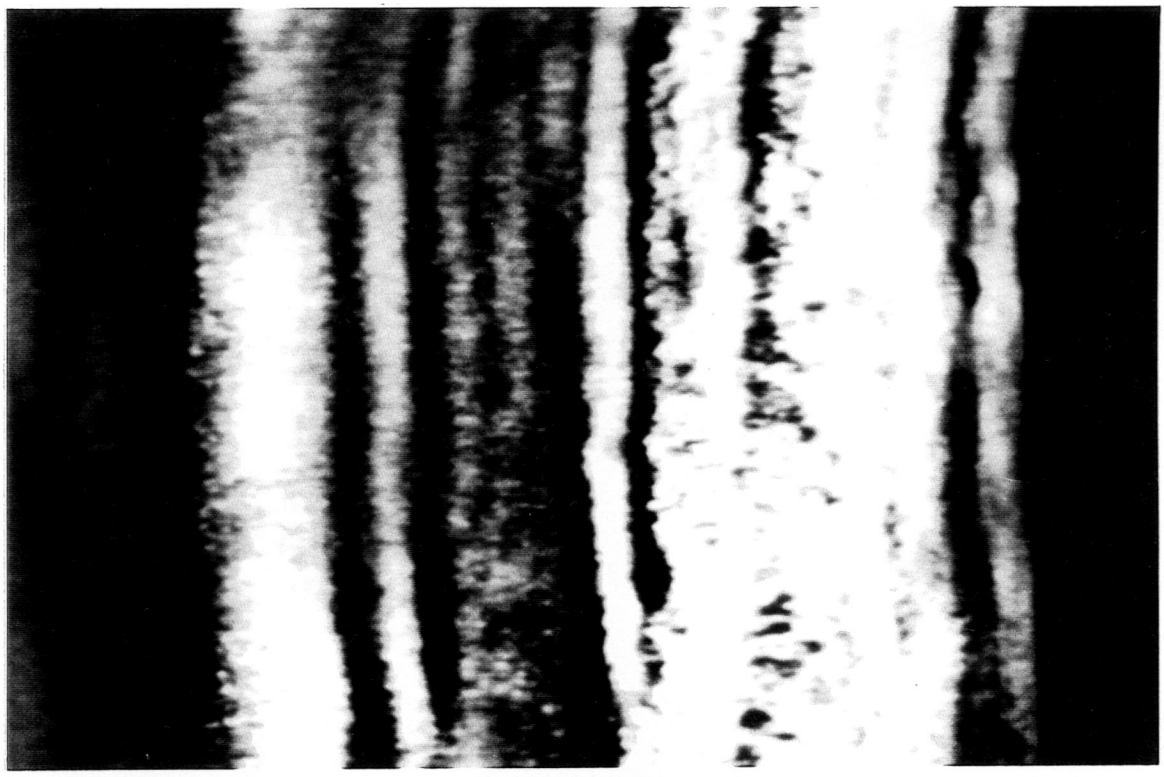

Fig. 5.5. Higher resolution STM image of a portion of the Si/Ge multilayer structure. x-range=500 nm, z-range=26 Å.

once, due to multiple tips on the scanning probe. Four of the layers are brighter than the Si substrate on the left and the Si cap immediately to the right of the multilayers. Based on this observation, the bright layers are deduced to be the Ge-containing layers, which is consistent with the designation in the previous images. A scan line across this image is shown in Fig.5.6b. The topographic contrast associated with the strain relaxation of the SiGe is about 30 Å.

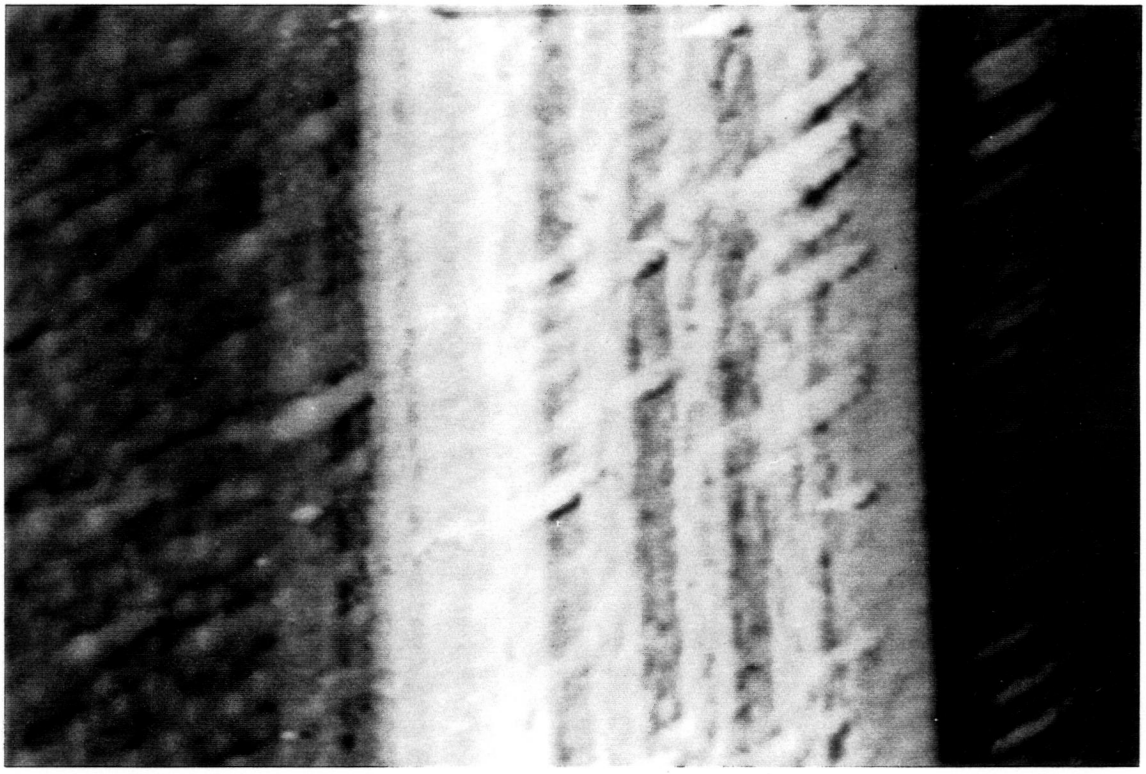

(a)

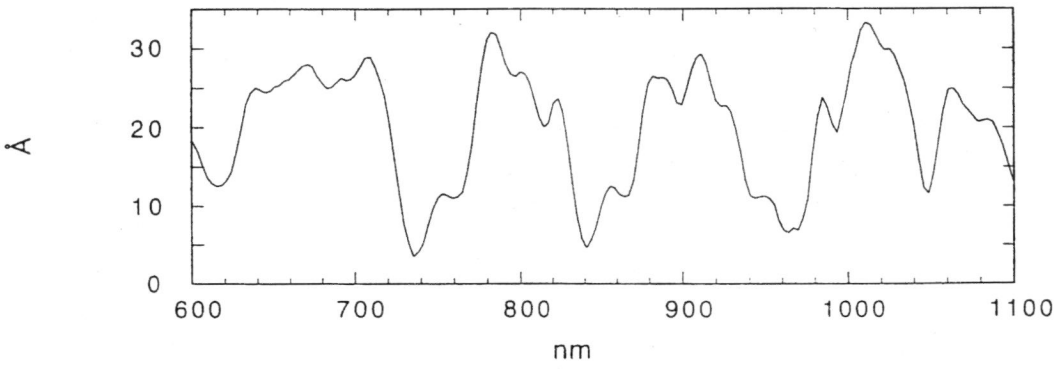

(b)

Fig. 5.6. (a) STM image of Si/SiGe multilayers and (b) topographic scan line (different lateral scale) across the layers. The Si capping layer is at the top edge of the sample, just before the black region on the right. The layer thickness is 40nm. Set point=(+1.5 V, 0.1 nA), x-range=1.0 μm, z-range=116 Å.

5.4. Imaging of Epitaxial GaAs/AlGaAs Multilayers

Fig. 5.7 shows an air STM image of a group of n and p GaAs layers[43] which had been grown on an AlGaAs buffer layer, which is on the far left. The contrast at the AlGaAs/GaAs interface is likely due to a cleavage step along the interface, with the AlGaAs cleaving higher than the adjacent GaAs layer. In the higher magnification image of this interface (Fig. 5.7b), taken at a different location on the same cleave, the AlGaAs has cleaved at a lower height. The horizontal drift in this image is due to creep in the piezoelectric tube scanner. The roughness observed in the AlGaAs region is likely due to selective removal of the aluminum during the chemical treatment. Similar roughening was observed in SEM micrographs obtained on samples in which the aluminum had been selectively etched in $K_3Fe(CN)_6$ solution to enhance the contrast between the AlGaAs and GaAs layers.[44] Presumably the selective etching is nonuniform and roughens the aluminum-containing regions.

In Fig. 5.8, an image of four periods of a GaAs/AlGaAs multilayer structure, grown on an n-type substrate, is shown. The individual GaAs and AlGaAs layers are 50 nm thick. The steps visible on the substrate are oriented in the (111) direction, and are caused by imperfect cleaving. Such steps would degrade the performance of GaAs/AlGaAs quantum well lasers, in which the mirrors of the laser cavity are the cleaved (110) facets. The substrate/epilayer interface apparently acts as a barrier to step propagation, since only one of the cleavage steps has propagated into the grown layers.

A large scale scan of the sample containing the 16 period multilayer structure (far left) described in §3.3 is shown in Fig. 5.9. Immediately to the right of the multilayer structure is a 1 μm wide layer of n-type GaAs followed by 1 μm of p-type GaAs. Another smaller (n-type) multilayer structure consisting of three AlGaAs layers and two GaAs layers is visible on the far right. The material to the right of these multilayers is n-type GaAs. The dc component of the data was removed by high pass filtering during image

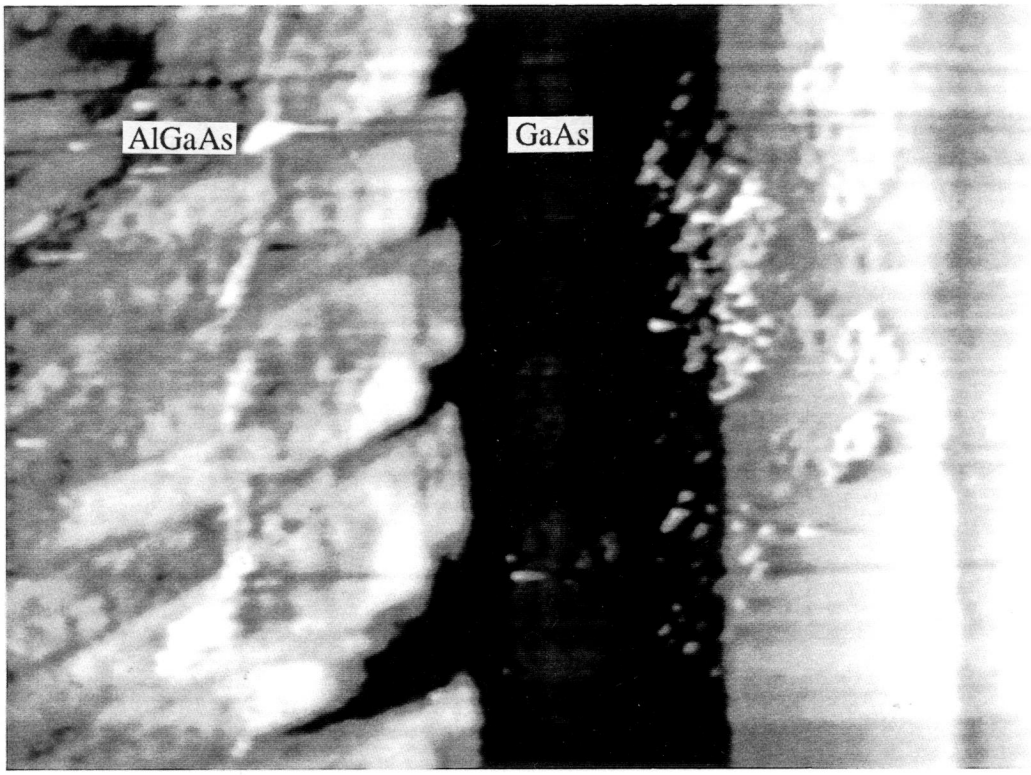

(a) x-range=3 μm, z-range=200 Å

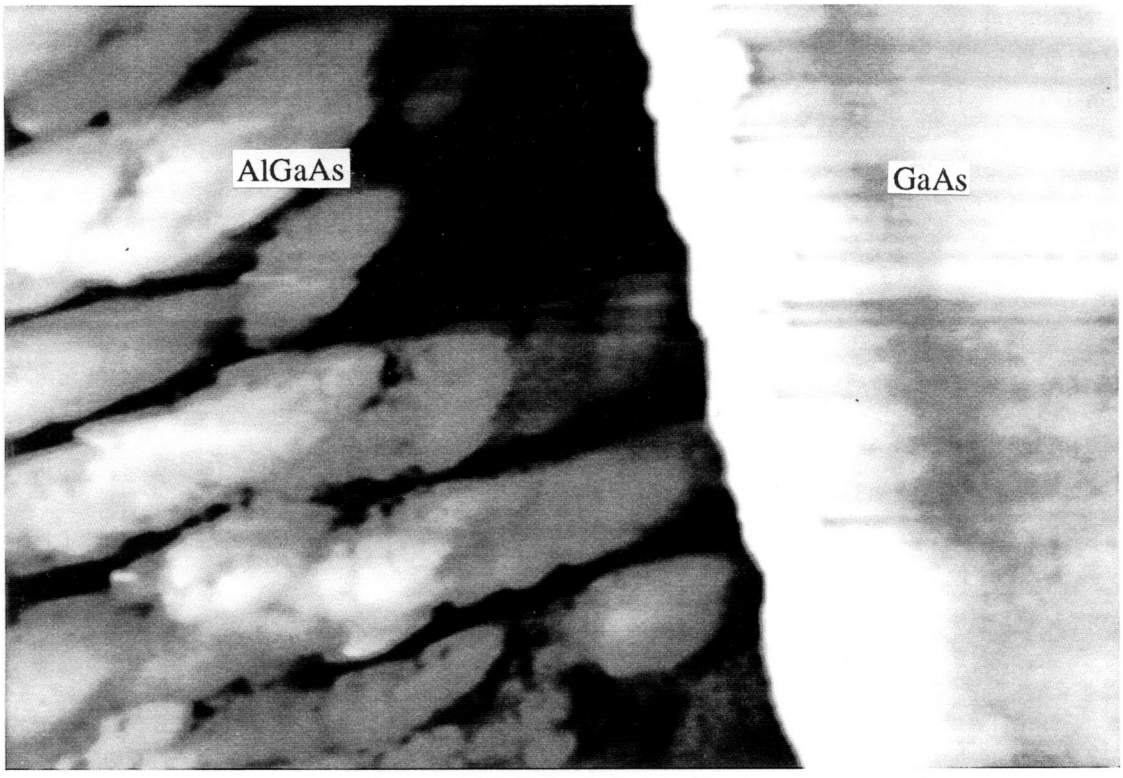

(b) x-range=1.3 μm, z-range=110 Å.

Fig. 5.7.(a) and (b) Topographic contrast at the GaAs/AlGaAs interface, attributed to preferential cleaving along the interface.

Fig. 5.8. Cleavage steps on the (110) GaAs surface, oriented in the (111) direction. A GaAs/AlGaAs multilayer structure is on the right. x-range=1.8 μm, z-range=80 Å.

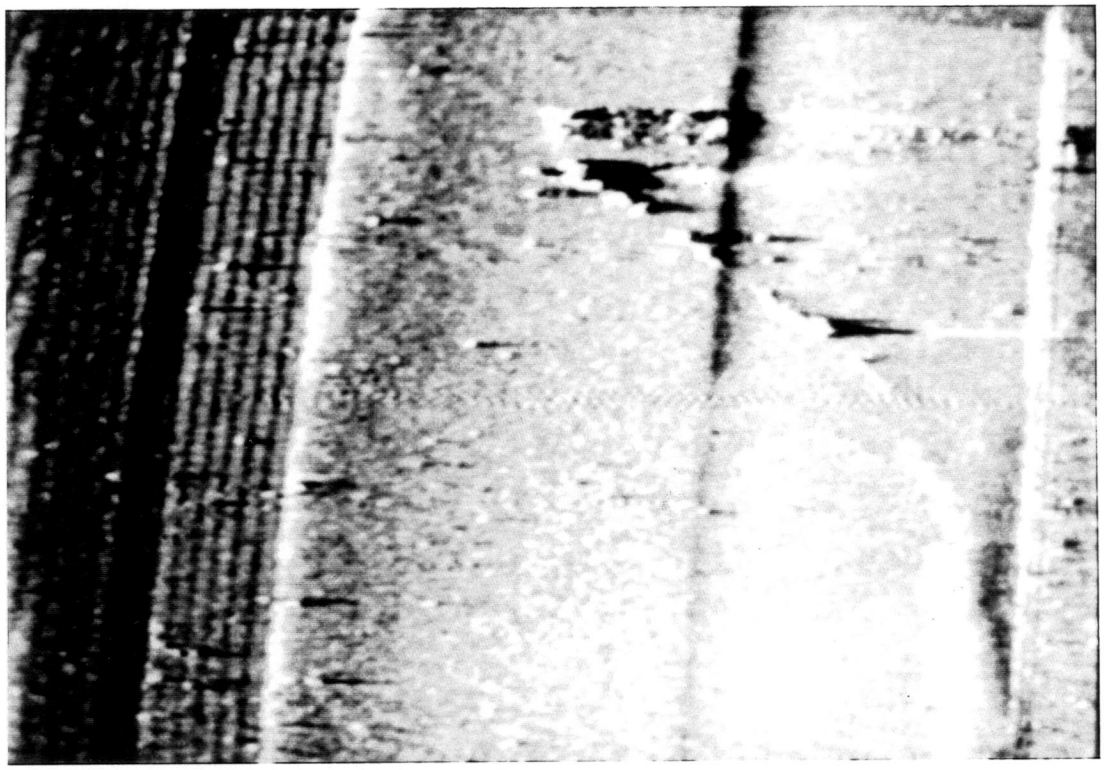

Fig. 5.9. STM image of a group of n and p layers grown on a semi-insulating GaAs substrate. A pn junction is sandwiched between the two multilayer structures. x-range=3.3 μm, z-range=10 Å.

acquisition, so that the image appears as if it was illuminated from the left. Nonlinearity in the piezo tube response (see§2.3) has distorted the lateral scale in this image. The topographic contrast associated with compositional modulation in both multilayer structures is probably due to selective etching of the Al-containing layers. In addition, there is contrast associated with the dopant type. The p-type regions of the epilayer all appear lower than the n-type regions. This effect is attributed to an electronic contrast mechanism discussed in the next section. [45]

A higher magnification image of the 16 period multilayer structure, acquired at a tunneling set point of (+4 V, 0.1 nA), is shown in Fig. 5.10. These layers were grown directly on the semi-insulating substrate. The MBE cleaning procedure, which involves thermal desorption of a thick protective oxide as discussed previously (§3.3a), roughens the substrate surface. The roughness is manifested in this image by the defect at the substrate/epilayer interface, encountered midway through the scan. This image indicates that the roughness is substantially reduced within one or two of the layers, which are 20 nm thick. A topographic scan line across the layers is also shown. The finite tip radius of the tunneling probe (§2.2) limits the resolution of the AlGaAs layers, which are lower than the GaAs layers. This is because the sides of the tip image the adjacent GaAs layers when the probe is positioned over an AlGaAs layer. The resolution of the the individual GaAs layers is about 1 nm in the p-region, based on the edge definition in the image. The relative thicknesses of the GaAs and AlGaAs layers can be deduced from the width of the flat portion of each peak in the p-type region of the scan line, which is interpreted as the GaAs layer thickness. Note that this may not be true for the n-type multilayers, where tip images due to roughenning of the n-type GaAs (§3.3c) obscure the resolution. Based on this assumption the GaAs and AlGaAs layers are found to be 23 ±2 nm thick. This is in rough agreement with the nominal values of 20 nm and 19 nm for the GaAs and AlGaAs respectively[46], deduced from the growth rate calibration of the molecular beam fluxes.

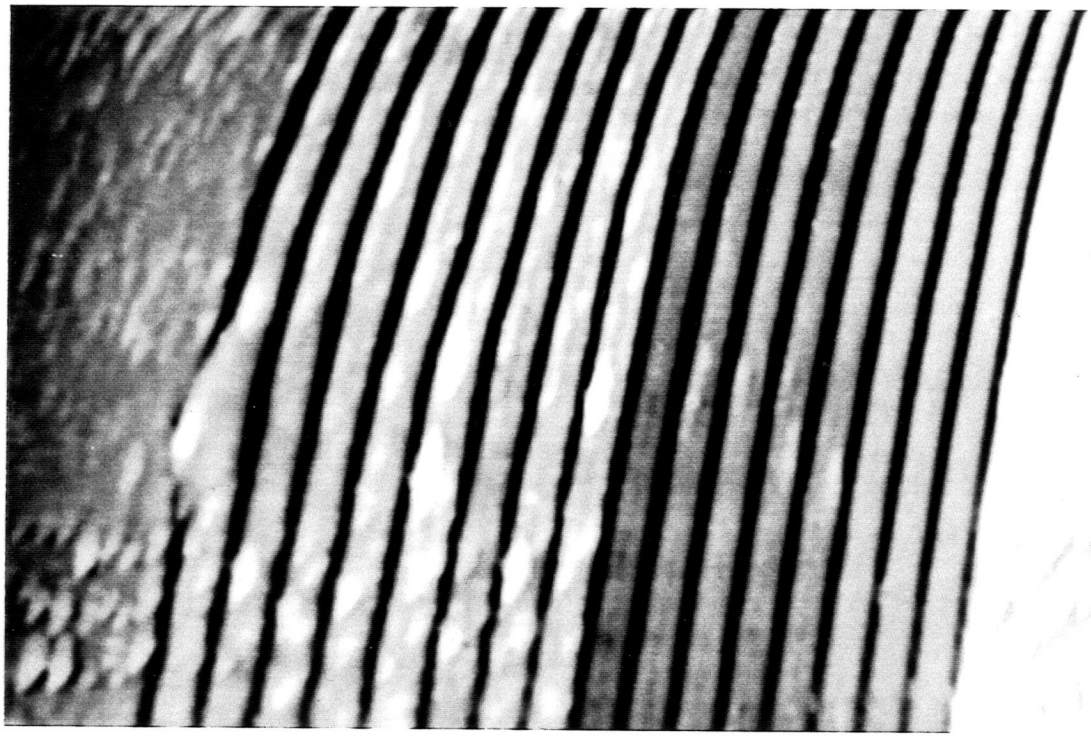

(a)

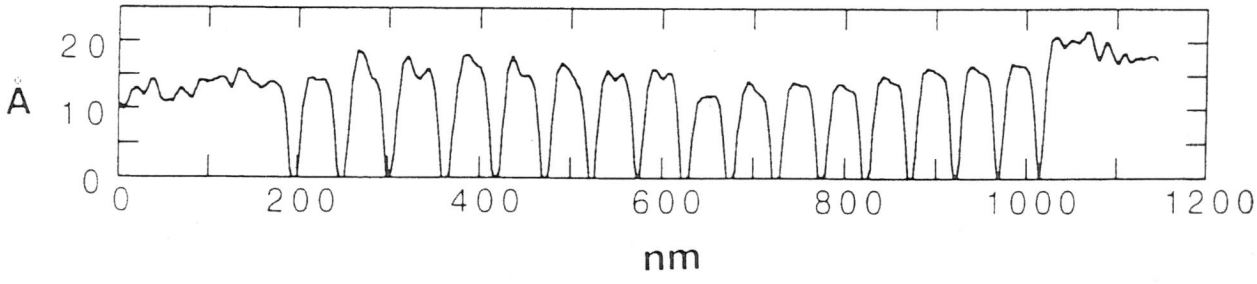

(b)

Fig.5.10. (a)Higher resolution image of the 16 period GaAs/AlGaAs multilayer structure and (b) topographic scan line (same lateral scale) across the multilayers. The first 8 periods are n-type and the remaining 8 periods are p-type. The p-type region is lower than surrounding n-type material by about 5 Å. From the p-type region of the scan line, the GaAs and AlGaAs layers are determined to be ≈23 nm thick.

5.5. Carrier-type Contrast in Images of GaAs np Structures

The image in Fig. 5.10 had not been high-pass filtered, and so the lower p region of the superlattice appears darker than the adjacent n-regions. The scan line shows this n-p contrast to be about 5 Å. The transition from n to p-type occurs within one layer thickness, so the junction position is located with at least 20 nm resolution. This is less than the depletion width, which is about 30 nm for this doping ($2x10^{18}$ cm^{-3}). Possibly the resolution is enhanced by the wider bandgap of the AlGaAs material in the depletion layer. The three-dimensional rendering (Fig. 5.11) of a pnp structure is taken from an image obtained on a different sample, at the same tunneling set point. The doping concentration for these layers was $\approx 5x10^{17}$ cm^{-3}. Again the p regions appear about 5 Å lower than the n-region. The contrast is attributed to the different electrical properties of the

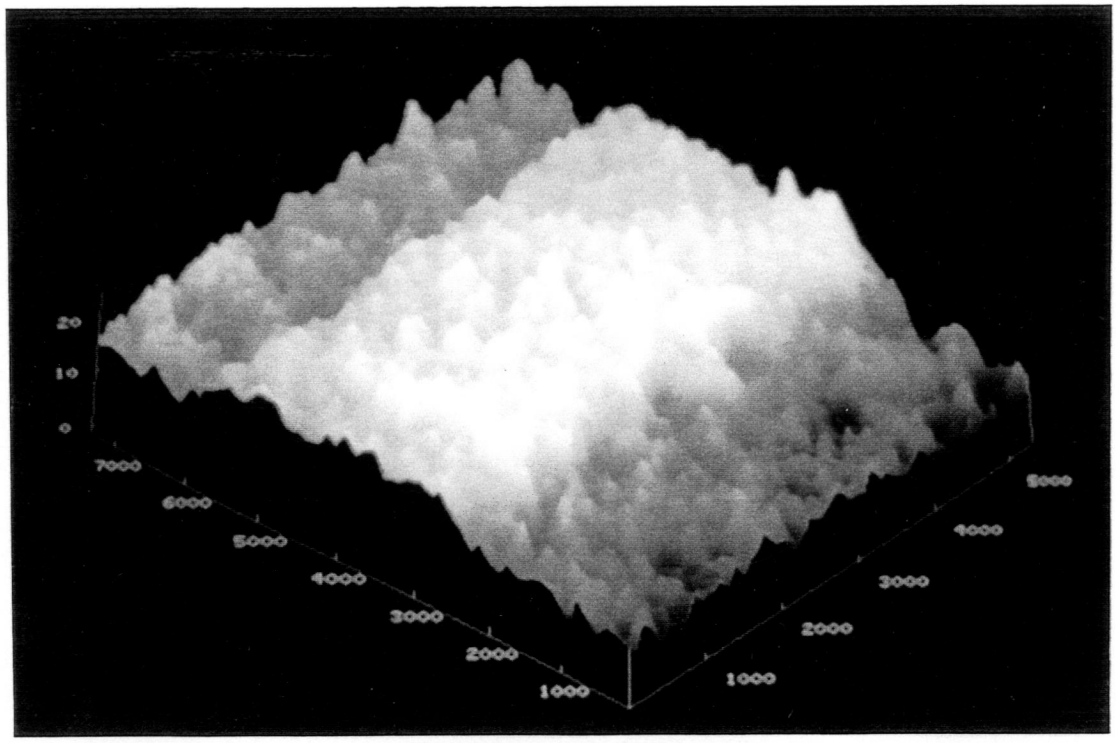

Fig. 5.11. Three-dimensional rendering of a pnp structure on GaAs, showing apparent topographic contrast of about 5Å. Lateral and vertical scales in angstroms.

p and n layers. This interpretation is consistent with the fact that the observed height change is about the same as that observed in recent UHV measurements[10] of an untreated GaAs pn junction cleaved in situ and imaged at a tip bias of +3 V. Also, atomic force microscopy measurements, which are insensitive to electronic structure, find[47] that topographic images of the chemically treated surface exhibit no contrast which correlates with layers of alternating dopant type.

To better understand the apparent topographic contrast in the STM images between the p and n type material, the current-voltage characteristics for the STM tunnel junction are calculated, using a model similar to that proposed by Feenstra and Stroscio[9]. The fitting parameters of the model are the sample surface affinity, the tip work function, the tunneling distance and the tunneling area. The surface band bending is determined from a one dimensional solution to Poisson's equation using degenerate statistics to accommodate inversion and accumulation at the surface.[48] Surface states in the bandgap are neglected consistent with the chemical passivation of the samples. Conduction is by direct tunneling from filled states on one side of the barrier to empty states on the opposite side, or by thermionic emission over the surface Schottky barrier followed by vacuum tunneling. The tunneling current through the vacuum barrier is calculated from the Bardeen expression[49] using the WKB approximation, including image force lowering. Tunneling through the space-charge region is neglected. For applied voltages large compared to the bandgap, the known bulk band structure of GaAs[50] along lines of symmetry is used in order to evaluate the phase space integrals which define the tunneling current. The energies of carriers not on a symmetry line are interpolated. The phase space integrals are computed by performing a direct Monte-Carlo summation over the Brillouin zone.[51]

Using this model, the tunneling distances at the imaging set point (+4 V, 0.1 nA) were found to be 15 Å and 12 Å over the n-type and p-type regions respectively. An effective tunneling area of 100 $Å^2$ was used along with an affinity of 4.1 eV for the semiconductor and a work function of 5.3 eV for the metal tip. The difference between the

two tunneling distances is in rough agreement with the 5 Å contrast we observe at the (+4 V, 0.1 nA) set point, and is consistent with the qualitative explanation[10] of this contrast presented elsewhere. For the p-type case, conduction is due to tunneling from occupied states in the valence band to empty ones in the tip. For the n-type case this conduction mechanism is also present, but the major current contribution comes from that part of the conduction band which bends beneath the Fermi level at the surface, as shown in the band diagram in Fig. 5.12. This is because the vacuum barrier height for conduction band tunneling is lower by the bandgap energy (1.4 eV) than the barrier for valence band tunneling. This explains why the vacuum gap must be reduced over the p-type regions in order to maintain the same current.

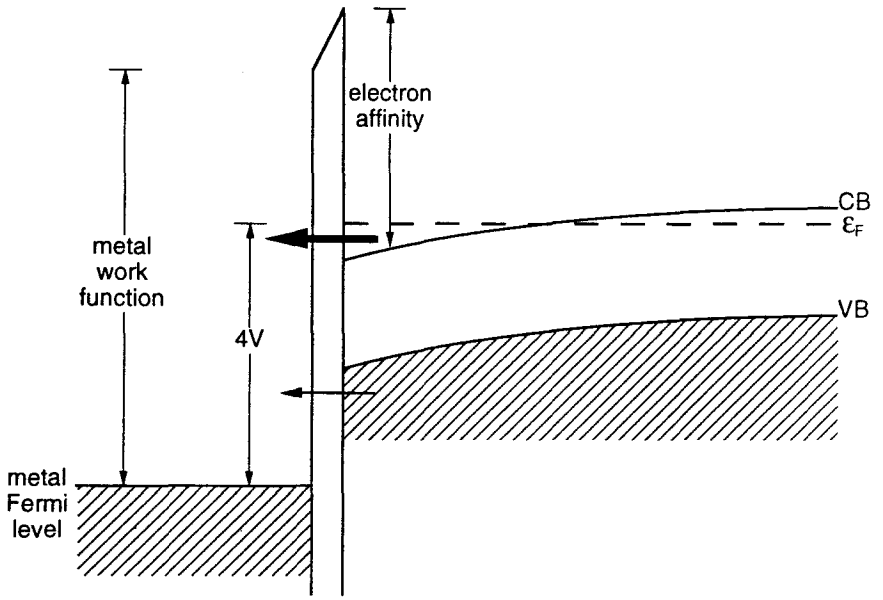

Fig. 5.12. Energy band diagram showing conduction mechanisms on n-type material at the scanning set point voltage (+4 volts on the tip). The barrier for tunneling through the vacuum is less for electrons in the conduction band (CB) than for electrons in the valence band (VB) by the bandgap energy.

5.6. Scanning Electron Microscopy of GaAs Epilayer Structures

Field emission SEM micrographs of the epitaxial structures were obtained[44] on the cleaved (110) surface and compared with the crossectional STM measurents of the same structures. It was found that the GaAs/AlGaAs multilayers were well resolved by the SEM, following the same chemical treatment used in preparing the samples for STM imaging. Fig. 5.13 shows a high resolution SEM micrograph (a) of a multilayer structure, accompanied by an air STM image (b) of the same structure. Since the SEM is not sensitive to topographical modulation of a few nanometers the contrast in the multilayers is believed to be electronic in origin. A lower magnification micrograph of the epilayer containing the 16-period multilayer discussed previously (§3.3.c.), is presented in Fig. 5.14. A cleavage step is present in the multilayer structure, which is on the far left side. Note that the SEM is also able to resolve the n and p layers. In contrast with the STM measurements, the n regions appear darker than the p regions, indicating that fewer secondary electrons are emitted from the n-regions. This contrast was present even for samples which had not been subjected to any preparatory etch, indicating that the contrast mechanism is electronic. Better contrast was achieved when the sample was scanned with 5 keV electrons as compared to 20 keV.

An explanation for the dopant-type contrast in the SEM micrographs is as follows: The Fermi level is pinned near the middle of the band gap at the surface. This pinning arises from surface states in the band gap, which might be induced by damage from the scanning electron beam. Surface pinning results in a depletion layer at the surface for both dopant types. The band-bending associated with the depletion layer in the n-type material would act as a barrier for the emission of the secondary electrons, whose energies are of the order of an electron volt. In the p-type material, the band-bending is such that a hot electron in the conduction band will encounter a reduced barrier for escape from the surface, compared to an electron in the same state in the n-type material.

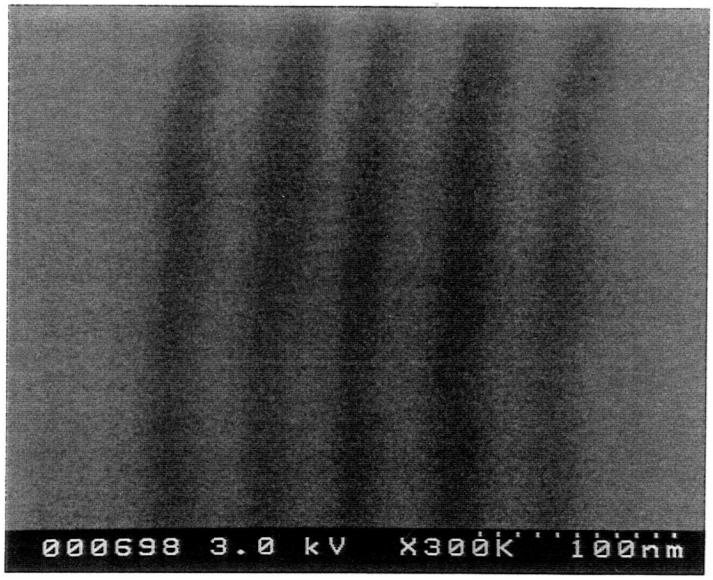

(a)

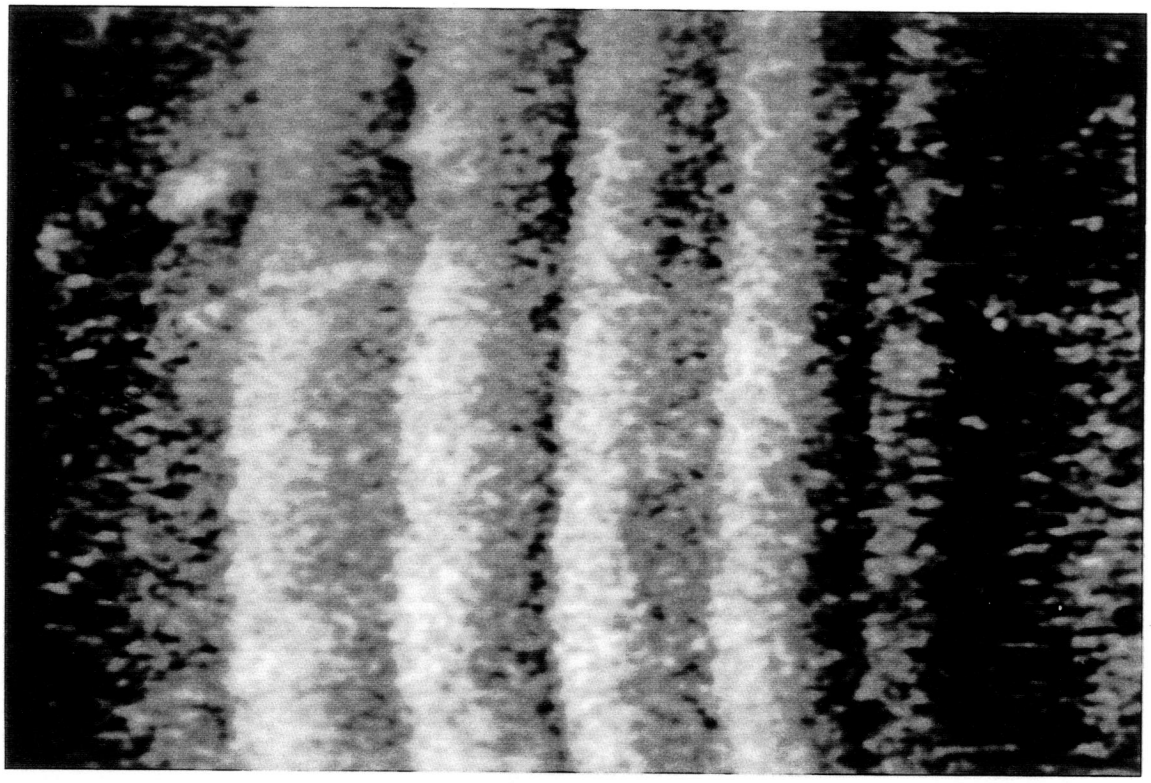

(b)

Fig. 5.13. Comparison of high resolution (a) SEM and (b) STM images of the same GaAs/AlGaAs superlattice. The layer thickness is 20nm and the z-range in the STM image is 30Å.

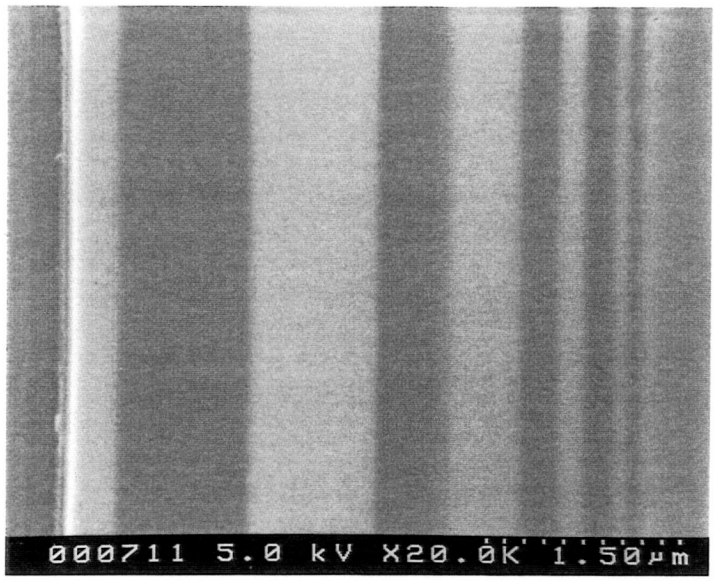

Fig. 5.14. SEM micrograph of epilayer containing the 16-period multilayer structure. The contrast between the n and p-type material is believed to be electronic in origin (see text).

6. Model for Current-Voltage Characteristics

The essential physics of the tunneling process is described by a model which assumes that the only conduction mechanism for electrons from the semiconductor to the metal tip is by thermionic emission over the Schottky barrier, followed by elastic tunneling through the vacuum barrier. This model is only applicable for small values of applied bias, when the Fermi level of the metal is within the bandgap of the semiconductor. At larger applied voltages, direct tunneling occurs, either from filled states in the metal to empty ones in the conduction band of the semiconductor, or from filled states in the valence band to empty ones in the metal. A more general model which includes these conduction mechanisms is then needed, such as the one discussed on p. 55. The description given here is similar to the metal/insulator/semiconductor (MIS) theory of Card and Rhoderick.[52]

Energy band diagrams at the surfaces of the metal probe tip and an n-type semiconductor surface are shown schematically in Fig. 6.1. The semiconductor surface is assumed to be free of states in the band gap, so the Fermi level is not pinned. In these diagrams, the horizontal axis represents distance in the direction perpendicular to the plane of the surfaces. The vertical dimension is potential energy in volts, with the convention that negative voltage (corresponding to higher electron potential energy) is up. ϕ_m is the metal work function, and χ_s and E_g are the semiconductor electron affinity and band gap, respectively. ξ is the difference between the bulk conduction band minimum, CB, and the semiconductor Fermi level, ε_{fs}, which decreases as the doping concentration is increased. ψ_m, ψ_{CB}, and ψ_{VB} represent the probability amplitudes which describe the wavefunctions in the vacuum for electrons originating from the metal Fermi level, semiconductor conduction band minimum, and valence band maximum respectively. The decay of these wavefunctions with distance, s from the surface, due to the vacuum energy barrier, ϕ_{vac} is given by $\psi \sim e^{-ks}$ where $k=\sqrt{\frac{2m\phi_{vac}}{\hbar^2}}$ and m is the free electron mass. From the diagram,

ϕ_{vac} is given by ϕ_m, χ_s, and χ_s+E_g respectively for electrons originating from the metal Fermi level, conduction band minimum and valence band maximum.

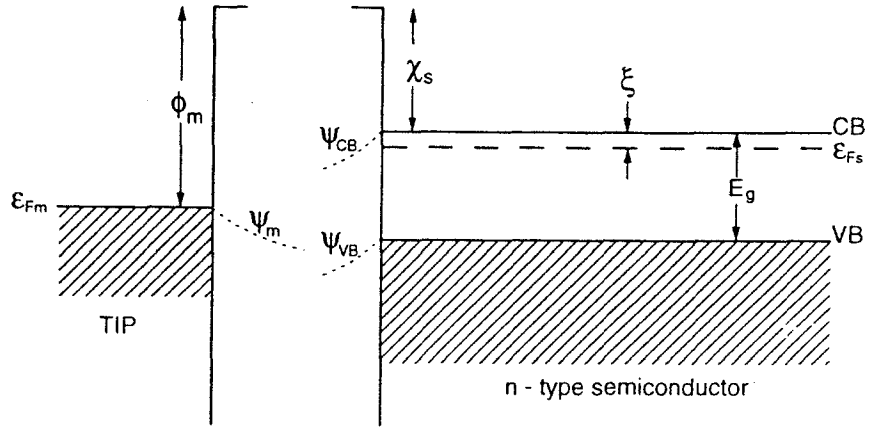

Fig. 6.1 Energy band diagrams for a metal surface and n-type semiconductor surface.

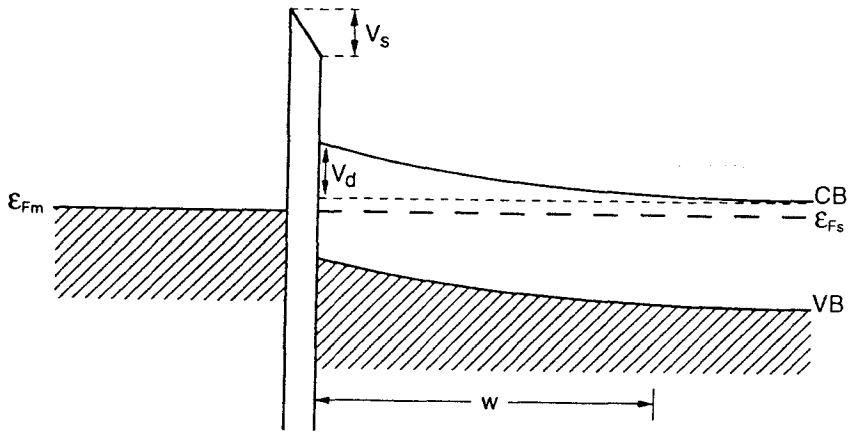

Fig. 6.2. Band-bending in the semiconductor induced by the tip. Zero bias case.

Fig. 6.2 illustrates the situation when the metal and semiconductor wavefunctions overlap (ie. when the tip is within tunneling range of the sample surface). No external voltage is applied between the probe and sample so the Fermi levels must align. In this case, $\phi_m>\chi_s+\xi$ so electrons in the semiconductor transfer into the metal, establishing a

space-charge region of uncovered donor ions at the semiconductor surface. This results in a voltage drop, V_d in the semiconductor due the band-bending in the space-charge region. Continuity of the normal component of the displacement field at the surface means that an additional voltage drop, V_s exists in the air gap, s, between the tip and the sample. If the metal and semiconductor surfaces are assumed to be planar,

$$\frac{V_s}{V_d} = \frac{2\varepsilon_{sc} s}{\varepsilon_{gap} W}, \qquad \text{where } W = \sqrt{\frac{2\varepsilon_{sc} V_d}{qN_D}} \; . \tag{1}$$

ε_{sc} is the semiconductor dielectric constant ($\varepsilon_{sc} \approx 13$ for GaAs and 11 for Si) and q is the magnitude of the electronic charge. ε_{gap} is the dielectric constant in the air gap, and is assumed to be unity. W is the width of the space-charge region calculated using the depletion approximation, which assumes that the space-charge density is just the donor density, N_D.

Fig. 6.3 shows the voltage drops in the gap and semiconductor when tunneling on n-type material at positive tip bias, V. The difference in the metal and semiconductor Fermi levels is seen to be:

$$V = \phi_m - \chi_s - V_s - V_d - \xi \; . \tag{2}$$

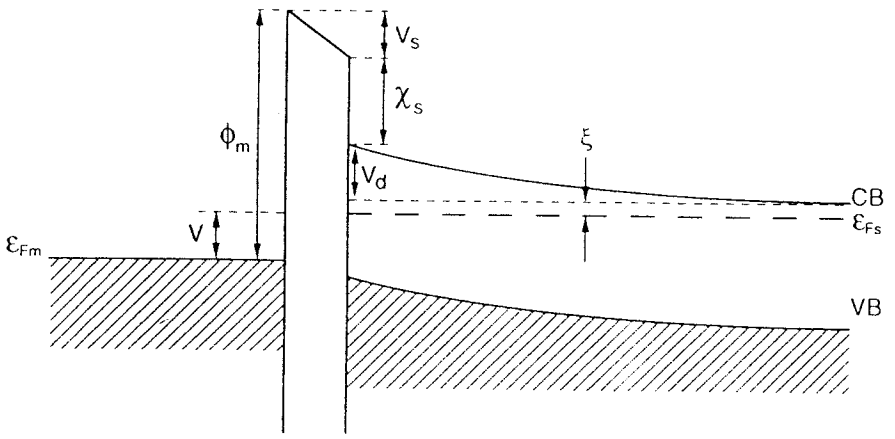

Fig. 6.3. Voltage drops in the vacuum gap and semiconductor with the tip positively biased.

This result holds only if the Fermi level remains constant in the space-charge region. This is a reasonable approximation to make provided the transmission coefficient through the vacuum gap is much less than unity. The net elastic tunneling current density, J_{ms} from the metal to the semiconductor is found by summing over the contributions at each energy, ε:

$$J_{ms} = -q \sum_{\varepsilon} T(\varepsilon)\cdot\rho^{m}(\varepsilon)\cdot\rho^{sc}(\varepsilon)\cdot[f^{m}(\varepsilon)\cdot\{1-f^{sc}(\varepsilon)\} - f^{sc}(\varepsilon)\cdot\{1-f^{m}(\varepsilon)\}], \qquad (3)$$

where $\rho(\varepsilon)$ is the density of states and $f(\varepsilon)$ and $\{1-f(\varepsilon)\}$ are the probabilty a state is occupied or unoccupied, respectively. The superscripts m and sc designate metal or semiconductor states. The summation over momentum states at each energy is not explicitly shown. For elastic tunneling, the transverse component of momentum must be conserved. Eq. 3 simply states that each component of the current density is the product of occupied initial states on one side of the junction and unoccupied final states on the other side, weighted by the transmission coefficient, $T(\varepsilon)$ for tunneling through the vacuum barrier.

The calculation of the current density is greatly simplified for small applied voltages, when the metal Fermi level is within the semiconductor bandgap, if one approximates the expressions for occupied states in the conduction band and unoccupied states in the valence band by delta functions located at the conduction band minimum and valence band maximum respectively. This approximation is reasonable because the decay of the Fermi-Dirac distribution, $f(\varepsilon)$ with energy above the Fermi level (exponential in the Boltzmann limit), is much more rapid than the increase in the density of states $\rho(\varepsilon)$, with energy above the conduction band minimum or below the valence band maximum (a square-root dependence in the effective mass approximation). With this approximation, the sum over energies in Eq. 3 is reduced to two terms. The first term, due to the contribution

from the conduction band, becomes:

$$J_{CB} \propto f(V_d)\{1-f(V_d-V)\} - f(V_d-V)\{1-f(V_d)\}$$
$$= f(V_d) - f(V_d-V)$$
$$\approx \exp\{-\frac{qV_d}{kT}\}[1-\exp\{\frac{qV}{kT}\}],$$

where the transmission coefficent and density of states prefactors have been omitted and f(ε) has been approximated by the Boltzmann distribution in the last step. Including the s-dependence of the transmission coefficient and converting to the standard convention (V positive for positive tip bias and J_{CB} positive for electrons flowing into the tip):

$$J_{CB} \propto e^{-2ks} \cdot \exp\{-\frac{qV_d}{kT}\}[\exp\{\frac{qV}{kT}\}-1], \quad \text{where } k=\sqrt{\frac{2m\chi_s}{\hbar^2}} \qquad (4)$$

In this expression, the trapezoidal vacuum barrier for conduction band tunneling has been approximated as a rectangular barrier of height $\phi_{vac}=\chi_s$, to estimate the s-dependence of the transmission coefficient. Using χ_s=4 eV, the affinity of (110) GaAs, this exponential prefactor can be written as $\exp\{-\frac{s}{s_0}\}$, where $s_0\approx$0.5 Å. This results in an order of magnitude attenuation in tunnel current per angstrom increase in tip-sample separation.

Eq. 4 is the same as that for a planar metal-insulator-semiconductor (MIS) Schottky diode. A large tip-sample separation corresponding to a thick insulating layer in the MIS diode results in a 'leaky' diode characteristic: as s increases, $V_d\rightarrow 0$ by Eq. 1, so that in reverse bias the metal Fermi level is raised above the conduction band minimum of the semiconductor, resulting in a large reverse current. For very small tip-sample separations ($s\rightarrow 0$), $V\rightarrow V_d$+constant (according to Eqs. 1 and 2), and the expression approaches that of an ideal Schottky diode: $J(V)=J_0\{\exp(\frac{qV}{kT}) - 1\}$. In this case, all of the applied voltage drop is in the semiconductor.

An expression similar to Eq. 4 can be obtained for valence band tunneling. For an n-type semiconductor, this term can become important when the tunnel junction is reverse biased (negative tip voltage), so that the valence band maximum approaches the Fermi

level. In this case electrons in the metal can tunnel directly into the empty states in the valence band, but must be thermally excited over an energy barrier in order to tunnel into the conduction band, if the metal Fermi level is below the conduction band minimum. Note that the barrier height for valence band tunneling ($\phi_{vac} \approx E_g + \chi_s$) is larger than the barrier for conduction band tunneling, however, resulting in a smaller transmission coefficient, so either process may dominate, depending on the details of the band-bending. For far forward bias, as discussed in §5.5, conduction band tunneling dominates when the surface is accumulated so that the conduction band minimum dips beneath the Fermi level. In this case, direct tunneling to empty states in the metal occurs from filled states in both the valence and the conduction bands, but the transmission coefficient is higher for the conduction band electrons. Note that Eq. 1 does not apply in this case, because degenerate statistics must be used to determine the band-bending when the Fermi level approaches either band.

7. Two-Dimensional Characterization of Electronic Structure

In order to learn more about the electronic contrast observed in the constant current images, current-voltage (IV) measurements were performed at selected regions in the cleaved epilayers. IV curves acquired at n and p-type regions resemble those of MIS Schottky barrier diodes, discussed in Chapter 6. The contrast between the n and p type characteristics is enhanced as the tip-sample separation is reduced.

The n/p contrast in the IV curves is exploited in a new current-voltage imaging (IVI) technique[45], which is designed to separate the electronic contrast in the STM images from the topography. In this technique, the current is measured at a preselected sampling voltage after setting the tip height independently. Various combinations of tip-sample separation and bias voltage were tried. Contrast between p and n regions was improved when the set point voltage which determines the tip-sample separation was kept small, consistent with the reduction in lateral band-bending described at the end of this chapter.

7.1 Electronic Characterization Methods

As discussed above, two methods — acquisition of current-voltage (IV) characteristics, and current-voltage imaging (IVI) — were used to identify and investigate electronic contrast in the epilayer structures. For both methods the current readings are made with the tip positioned at a constant height over the sample, using the method described in Appendix A. The tip bias is left at the imaging set point throughout the procedure, and changes in the tip-sample voltage are made by adjusting the sample bias. The tip-sample separation is set by adjusting the sample voltage with the current held constant by the feedback loop. IV characteristics are acquired by ramping the sample voltage and measuring the tunneling current with the feedback loop disabled. Current

readings in the IVI scans are made at the preselected sampling voltage only. In the IV curves the current is plotted as a function of the difference between the tip and sample voltages; typically the data of twenty or more successive voltage ramps are averaged to reduce the noise bandwidth. The tip-sample separation is reset between each voltage ramp. In the IVI scans, the tip translation is done at the imaging set point to minimize damage to the surface.

Because the data acquisition time is long (typically 200 ms per pixel), larger pixels and smaller scan ranges were used in the IVI scans, as compared with the constant current scans. In this sense, the IVI technique is a practical compromise between the higher resolution of the constant current mode, and the electronically richer information in the IV curves. Once the scan is finished, the IVI results are displayed as a greyscale image similar to the constant current images, except that the greyscale represents the range of current readings. Leakage currents between the probe tip and the grounded inner-wall electrode on the piezo tube (see §2.1) are of the order of 30 pA at +3 V on the tip. Because the tip bias remains fixed, the tip leakage current contributes a dc shift to the IV and IVI current readings, which can be subtracted after data acquisition.

7.2. Dependence on Tip-Sample Separation

Fig. 7.1 shows two sets of IV curves, obtained while tunneling on the cleaved (110) surfaces of (a) n-type ($1x10^{17}$ cm^{-3}) Si and (b) n-type ($2x10^{18}$ cm^{-3}) GaAs substrates. The surfaces had been prepared for imaging using the procedures described in §3.2a and §3.3b for Si and GaAs respectively. The curves in both (a) and (b) were obtained at successively decreasing tip-sample separation, s, by reducing the tip-sample voltage of the set point with the feedback enabled. The feedback was disabled while the measurements were made. As with other work[53] on passivated Si, the curves in (a) become more asymmetric as s is reduced, consistent with enhanced rectification as the

junction characteristic approaches that of an ideal Schottky diode (see discussion after Eq. 4 in Chapter 6). The GaAs curves in (b) are all asymmetric, possibly because the band-bending is still significant at the largest tip-sample separations represented in the figure.

(a)

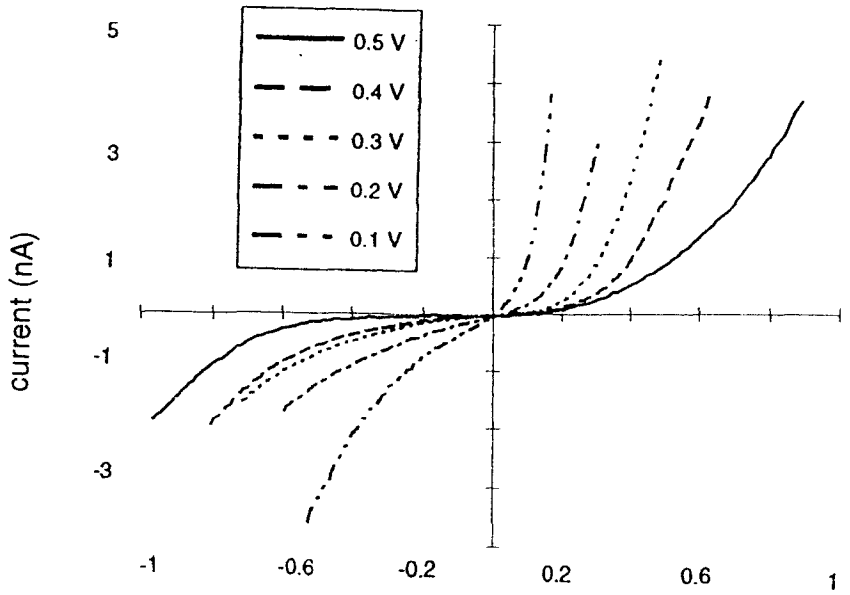

(b)

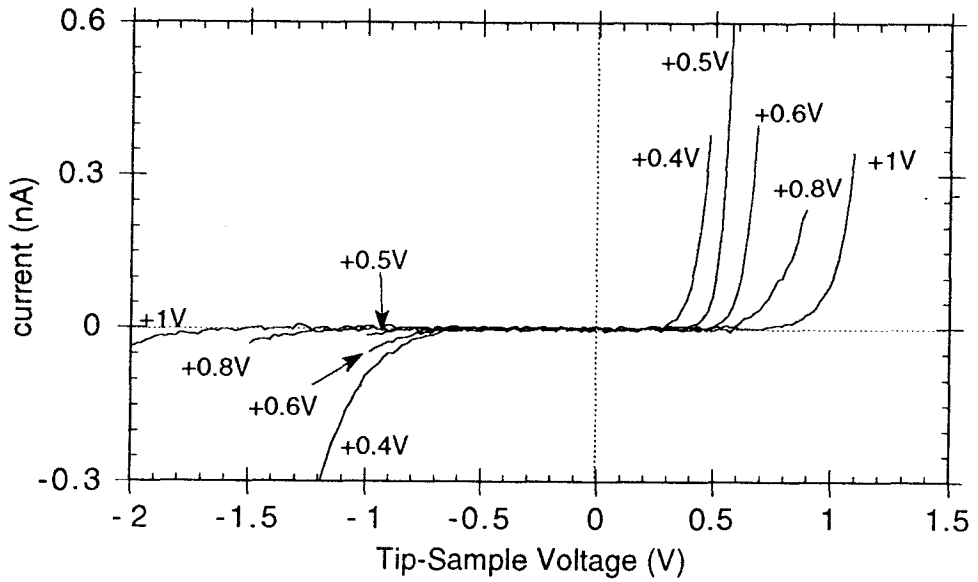

Fig.7.1. Current-voltage characteristics on (a) n-type Si and (b) n-type GaAs obtained in air at various tip-sample separations determined by the operating set point voltage. The current at the set point voltage is 1 nA in (a) and 0.1 nA in (b).

The data also show that breakdown in reverse bias (tip-sample voltage < 0) occurs sooner as s is reduced. The mechanism responsible for this behaviour[54] is illustrated by

the band diagrams in Figs. 7.2 and 7.3 for tunnel junctions with small and large vacuum gaps respectively. At zero bias the band bending associated with the the difference in the metal and semiconductor work functions results in a Schottky barrier which is greater for the junction with smaller s, as expected in the MIS model. As this junction is reverse biased, the band-bending increases until the valence band maximum coincides with the semiconductor Fermi level (Fig. 7.2b). Degenerate statistics must be used to describe the carrier populations in this case, so the model in Chapter 6 does not apply. The result of the inversion is that the band-bending increases at a substantially reduced rate so that the energy difference between the metal Fermi level and the semiconductor conduction band is reduced with increasing reverse bias (Fig. 7.2c), resulting in an increase in tunnel current. Initiation of this effect requires larger reverse voltages for junctions with greater vacuum gaps, because the zero-bias band-bending is smaller (Fig. 7.3a.).

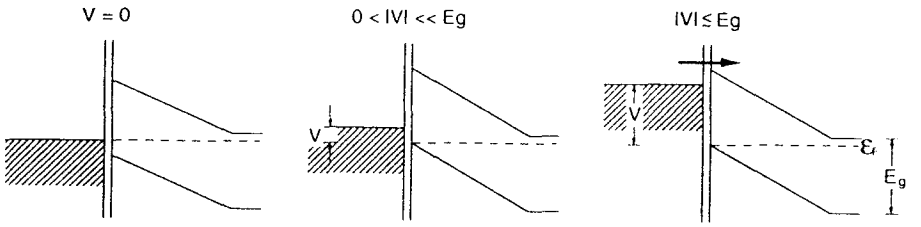

Fig. 7.2. Reverse break down in tunnel junction IV characteristic for the case of small tip-sample separation. The zero-bias band-bending (left) is quite large so that degenerate conditions occur at a small reverse bias voltage (middle). Larger reverse biasing (right) results in reduction of the Schottky barrier and an increase in reverse current.

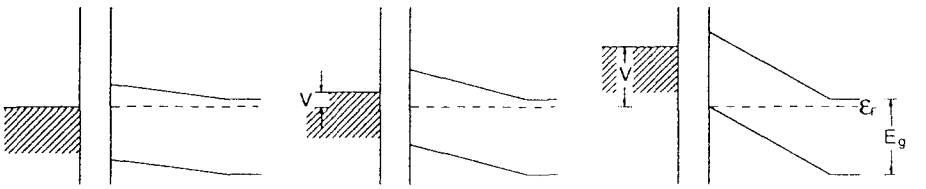

Fig. 7.3. Reverse break down for the case of a large tip-sample separation. The band-bending at zero bias (left) is small due to the drop in the vacuum gap, so degenerate conditions do not occur until a relatively large reverse bias is applied (far right).

7.3. Dependence on Carrier Type

The results of current-voltage measurements performed over n-type and p-type regions of (a) Si and (b) GaAs surfaces are presented in Fig. 7.4. In each case the operating point which sets the tip height is the same for the n and p-type IV curves. The curves intersect at the common set point in the positive quadrant of each graph. The set point voltage for these measurements is smaller than the imaging voltage, in order to enhance the asymmetry in the IV curves as discussed in the previous section. Fig. 7.4a shows IV characteristics obtained at a set point of (+0.5 V, 1 nA), over the n-type substrate and p-type cap (both $1x10^{17}$ cm^{-3}) of the sample on which the Si/Ge superlattices (§5.2) were grown. Fig.7.4b shows IV curves obtained over the n-type substrate ($2x10^{18}$ cm^{-3}) and p-type capping layer ($3x10^{17}$ cm^{-3}) of a GaAs sample, at a set point of (+1 V, 0.1 nA). The acceptor doping concentration of the p-type epilayer in this sample was determined from Hall effect measurements.[55] These IV characteristics are typical of many n-type and p-type curves obtained on Si and GaAs, and can be qualitatively understood in terms of ideal Schottky diode behaviour. When the tip is negative with respect to the sample, the p-type material is forward biased and the n-type is reverse biased. The larger reverse current of the p-type curves in Figs. 7.4(a) and (b) indicates that the the tip is closer to the p-type surface than the n-type surface at the operating set point. Presumably the reverse would hold at a negative value for the set point voltage, although instabilities at negative tip bias (see §2.1) prevented the acquisition of meaningful data to test this.

The curves in Fig.6.4b are accompanied by theoretical fits. The theoretical curves are calculated with the model used in §5.5, using the same values for the semiconductor affinity and metal tip work function. The tunneling area was set equal to 100 $Å^2$ and the vacuum tunneling gaps adjusted to fit the data. The fits shown were obtained for tunneling gaps of 6.5 Å and 3 Å for the n and p-type curves respectively.[51]

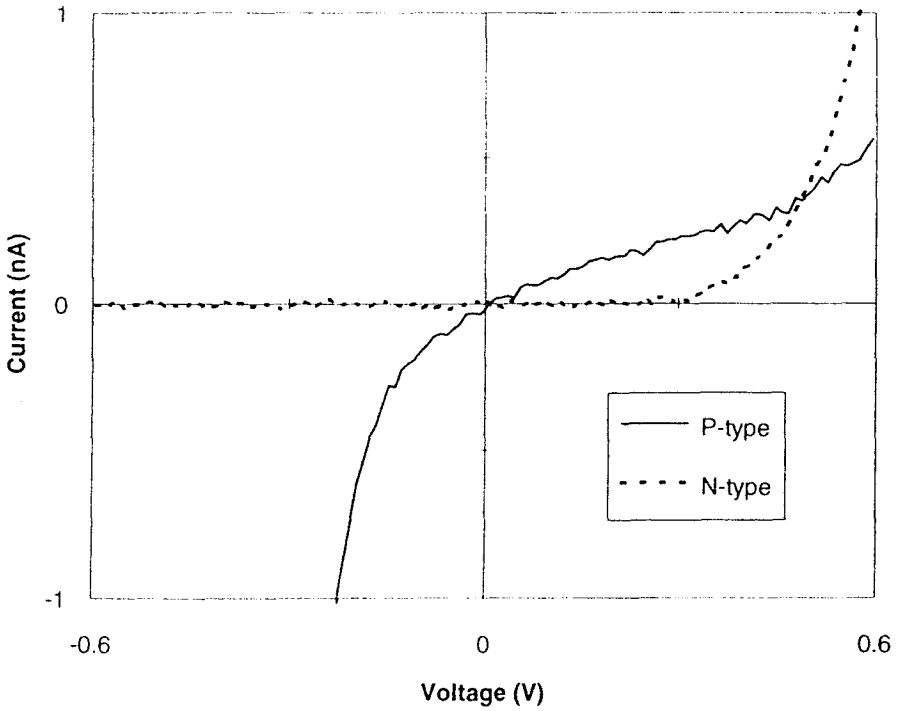

(a)

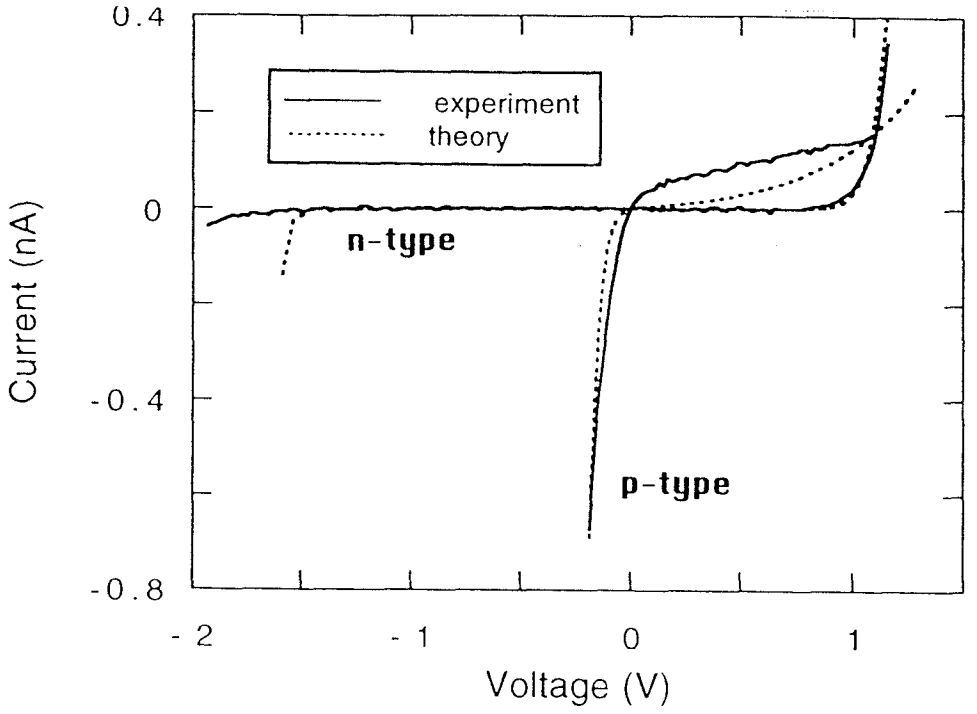

(b)

Fig. 7.4. IV characteristics obtained over n- and p-type regions on (a) Si and (b) GaAs. The n and p curves intersect at the operating set point which is common for both.

7.4. Spatial Resolution

Fig.7.5 is a series of IV curves obtained across the Si/Ge superlattice, following acquisition of the image in Fig.3.16. The image is repeated in the inset for reference. It was hoped that the measurements would reveal electronic contrast in the superlattice, associated with the different band gaps of Si (E_g=1.1 eV) and Ge (E_g=0.67 eV). Data was acquired at equally spaced intervals along a line indicated by the white bar shown in the inset, at a set point of (+1 V, 0.5 nA). These curves are typical of more extensive data taken across these multilayer structures. Although there are differences in the IV curves as a function of position in the multilayer, there are no systematic differences which

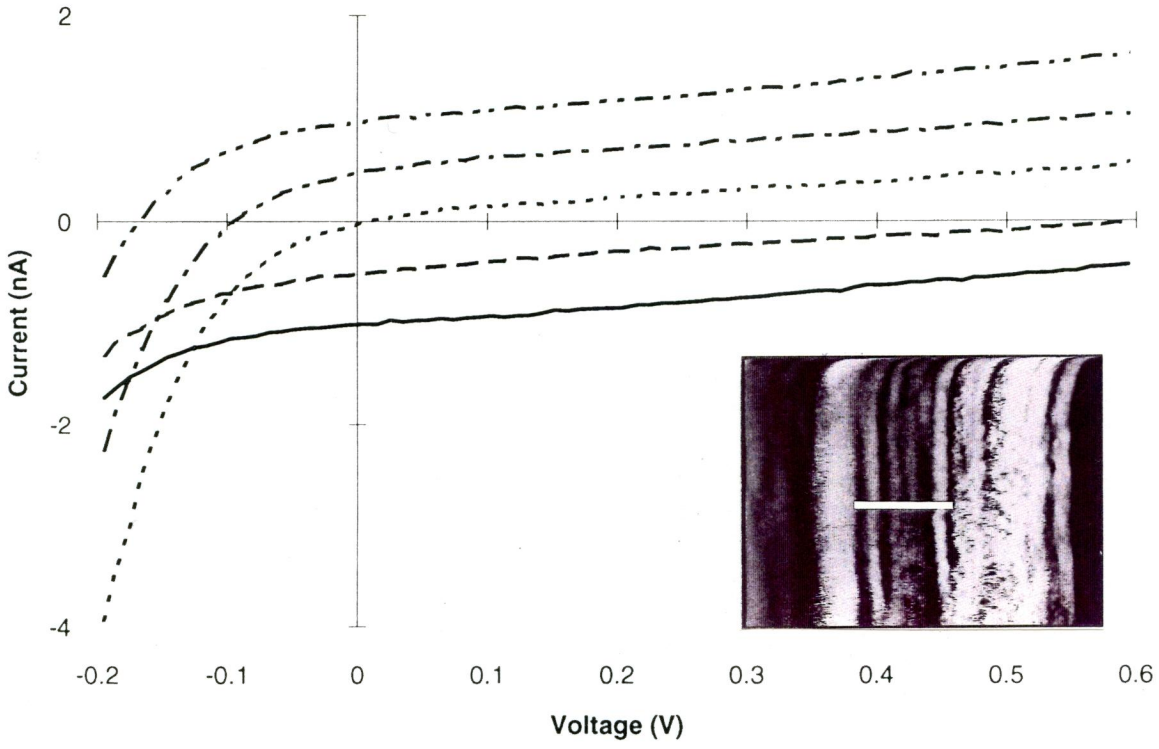

Fig. 7.5. Series of IV curves obtained across the Si/Ge superlattice multilayer structure shown in the inset. The curves, which were obtained at equally spaced points along the white bar in the inset, are spaced apart vertically for clarity. The operating set point was (+1 V, 0.5 nA).

correlate in a simple way with the layer periodicity. The depletion width (Eq.2, Chapter 6) for 0.1 V band-bending at the surface is about 300 nm for these intrinsic layers ($\sim 10^{15}$ cm^{-3}). Most likely the band-bending, which extends laterally across the surface as well as into the bulk, obscures the delineation of the 20 nm thick layers.

A series of IV characteristics obtained at a set point of (+0.5 V, 0.5 nA) across an np junction grown on an n-type Si substrate[56], is shown in Fig. 7.6. The curves, which were acquired sequentially at ≈115 nm intervals along a line perpendicular to the np junction, are spaced apart vertically for clarity, so that the first curve in the sequence is at the origin. The composition of the junction, in the direction of the measurement sequence is: n^+ substrate (5×10^{18} cm^{-3}); 900 nm lightly doped (10^{17} cm^{-3}) n-type; and p+ (2×10^{19} cm^{-3}) capping layer (100 nm). The first three curves, which cover a range of about 350 nm, resemble the n-type curve in Fig. 7.4a, which was acquired at the same set point on a lightly doped (10^{17} cm^{-3}) n-type substrate. These curves are therefore thought to correspond either to locations in the 900 nm n-type layer or in the n^+ substrate. By contrast, the remaining curves in the series are essentially symmetric. Presumably these symmetric curves correspond to the p^+ cap. IV curves (not shown here) on graphite (a semimetal) and gold surfaces were also found to be symmetric. The p^+ material, which is degenerately doped so that the Fermi level in the bulk is below the valence band maximum, might be expected to have a similar IV characteristic.

An IVI-STM image acquired over the same area and at the same operating point as the IV data is shown in Fig. 7.6b for comparison. The image is oriented vertically for ease of comparison with the IV data and has a lateral scale which corresponds to the vertical spacing of the IV curves. The current range greyscale in the image, acquired at -0.5 V, is +1.7 nA (white) to -1.7 nA (black). The bottom region is grey (no current) for about 400 nm, consistent with the reverse bias region of the corresponding n-type curves. There

is a transition to saturated black as the capping layer is approached, again consistent with the IV measurements. Note that more noise is present in the IVI scan than might be expected from the relatively noiseless IV curves. The data in this IVI scan were obtained from a single measurement, whereas the data points in the IV curves each represent the average of 20 current readings acquired over successive voltage ramps.

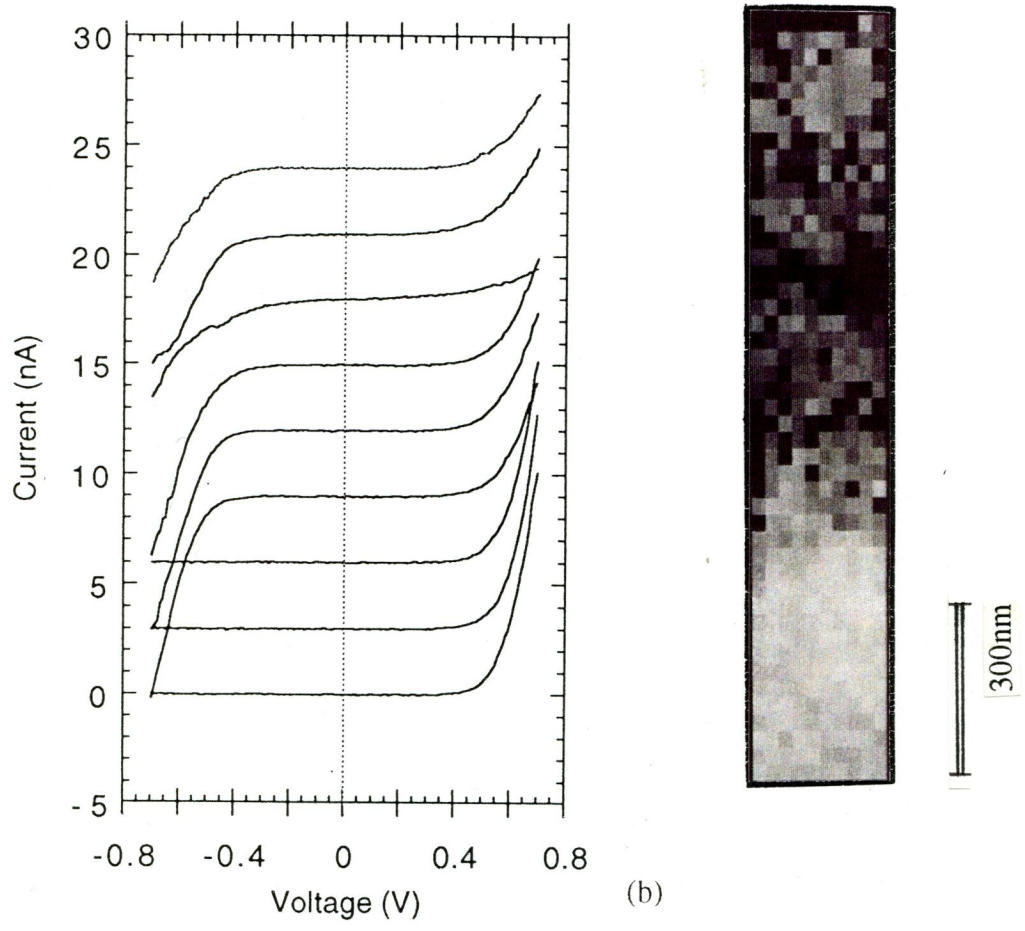

Fig. 7.6. Series of IV characteristics (a) and IVI scan (b) taken across the n-p junction on Si described in the text. The operating point was (+0.5 V, 0.5 nA) for both measurements, and the sampling point for the IVI scan was -0.5V. The current range greyscale in the IVI image is -1.7 nA (black) to +1.7 nA.(white).

The apparent width of the p^+ region indicated by the IV sequence and IVI scan is more than 700 nm. However, only 100 nm of p^+ material was grown in the capping layer. Tip induced band-bending, which would result in a 100 nm depletion region in the n-layer, does not by itself account for the poor spatial resolution. Another mechanism, in which the equilibrium barrier height of the np^+ junction is reduced by lateral band-bending in the plane of the surface, would further affect the spatial dependence of the IV curves. A qualitative description of this effect is given for the case of a measurement made on a p-region in close proximity to an n-region: When the tip is positioned over a p-type region, one would ordinarily expect only a small current to be drawn at positive tip bias (see Fig. 7.4). The situation changes in close proximity with an n-type region, if the lateral band-bending induced by the tip extends into the depletion region of the pn junction (Fig. 7.7). Whent the tip-induced band bending is small, the pn junction is effectively

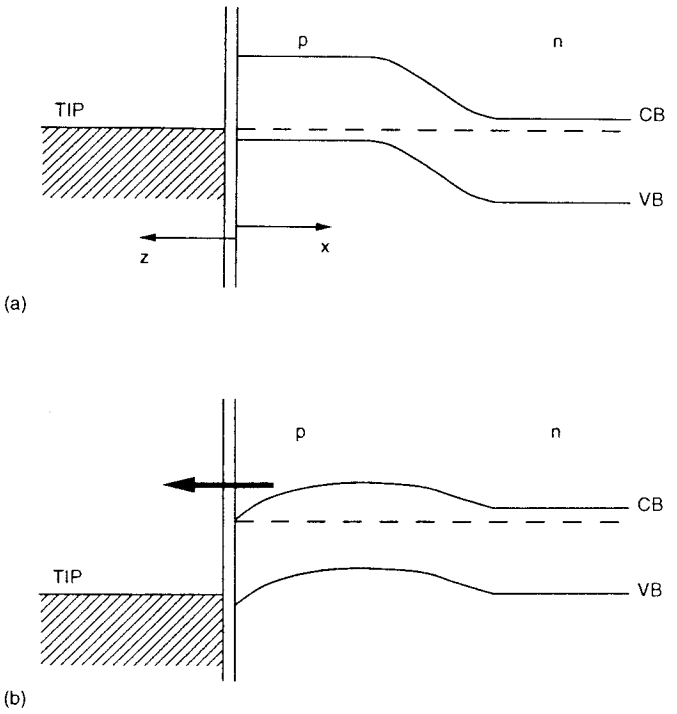

Fig. 7.7. Tip-induced band-bending over a p-layer in close proximity with an n-region. z is perpendicular to the sample surface and x represents a lateral dimension along surface. As the tip voltage is made more positive (reverse bias for p-type), the np junction becomes forward biased (b) due to lateral band-bending effects.

unbiased and no net current flows across the depletion region (a). As the tip becomes more positively biased however, the barrier for transport of electrons from the n-type side of the junction to the p-type side is reduced and a net current flows into the p-region beneath the tip (b). In effect, the pn junction becomes forward biased at positive tip voltages, when the tip is over the p-type side but close to the junction. The contrast between the n and p material is thus limited to the difference between a forward biased MI-n diode (over the n-regions) and a forward biased MI-pn diode (over the p-regions), both of which have exponential IV characteristics. The common set point ensures that the pre-exponential multiplicative factor is the same for both cases, essentially eliminating any contrast. The spatial extent over which this mechanism operates depends on the details of the band-bending, but computer simulations[16] show that it can be many times the depletion width. To improve the resolution, it is therefore necessary to reduce the band-bending at the operating set point.

Fig. 7.8 shows an IVI-STM measurement taken across the GaAs npn structure in Fig. 5.9, in which the p-type region is 1 μm wide, and the doping level is $2x10^{18}$ cm^{-3} for all three regions. The reference tip-sample separation was set by a (+0.5 V, 30 pA) operating point, and the current image was acquired at -0.9 V. The image clearly shows the p-type layer between the two n-type layers. The data indicates that the current over the p-region is approximately -50 pA, while no current is drawn over the n-regions at the sampling voltage. This is consistent with the interpretation that the p-region is forward biased at this voltage. Possibly the voltage at the operating set point is small enough that lateral band bending has not significantly affected the contrast in this image. A scan line taken from a constant current image of the same structure is shown below the IVI image for comparison. The image was obtained immediately before the IVI scan, at a set point of (+4 V, 0.1 nA). The apparent topographical contrast due to the conductivity type is nearly 10 Å in this image.

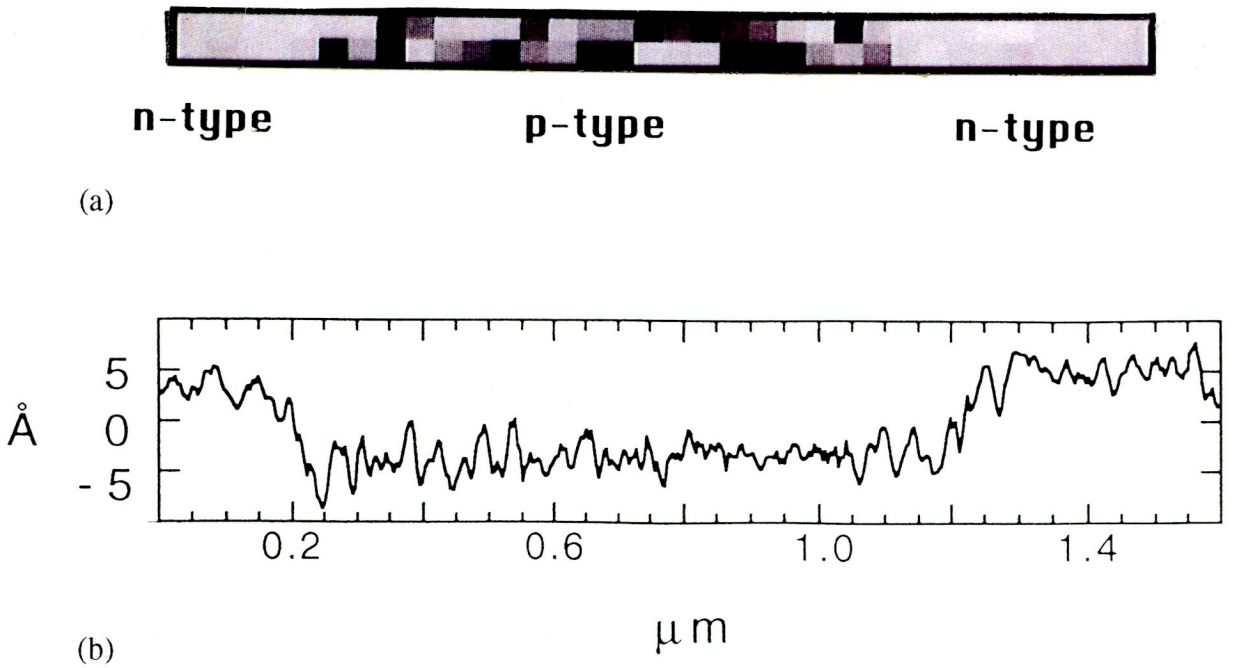

Fig. 7.8. IVI scan (a) and constant-current topographic scan line (b) across an npn structure on GaAs. The operating point for the IVI scan was (+0.5 V, 0.03 nA) and the data acquistion voltage was -0.9 V. The current range greyscale is -0.25 nA - 0.05 nA. The constant current set point in (b) = (+4 V, 0.1 nA).

The IVI data acquired over the forward biased p-regions in these scans is noisy. An explanation is that the tip is not set at the same height above the surface at each point. Tip noise, possibly due to mobile adsorbates on the sample or tip, causes the tip-sample separation to fluctuate in the constant current mode with amplitudes of one or two angstroms (since the control loop servo attempts to maintain a constant current by adjusting the tip height). This fluctuation is a source of random error when the tip feedback control is put on hold. Because changes in tip-sample separation of 1 Å cause the tunneling current to change by approximately an order of magnitude, small fluctuations in the tip elevation will cause large fluctuations in the current-voltage characteristic.

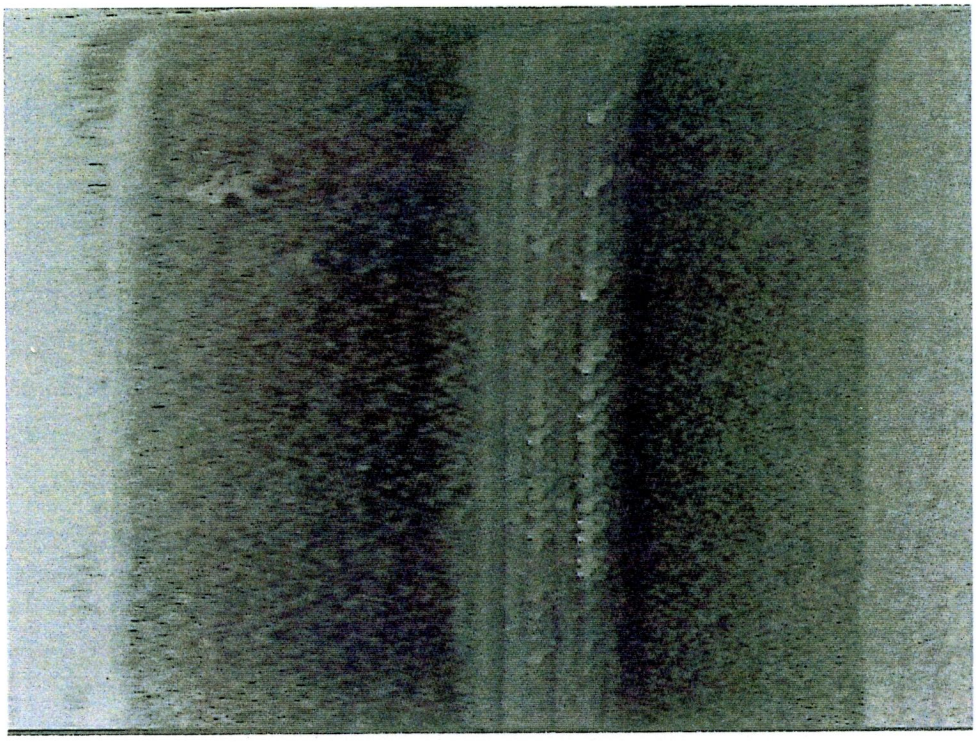

(a)

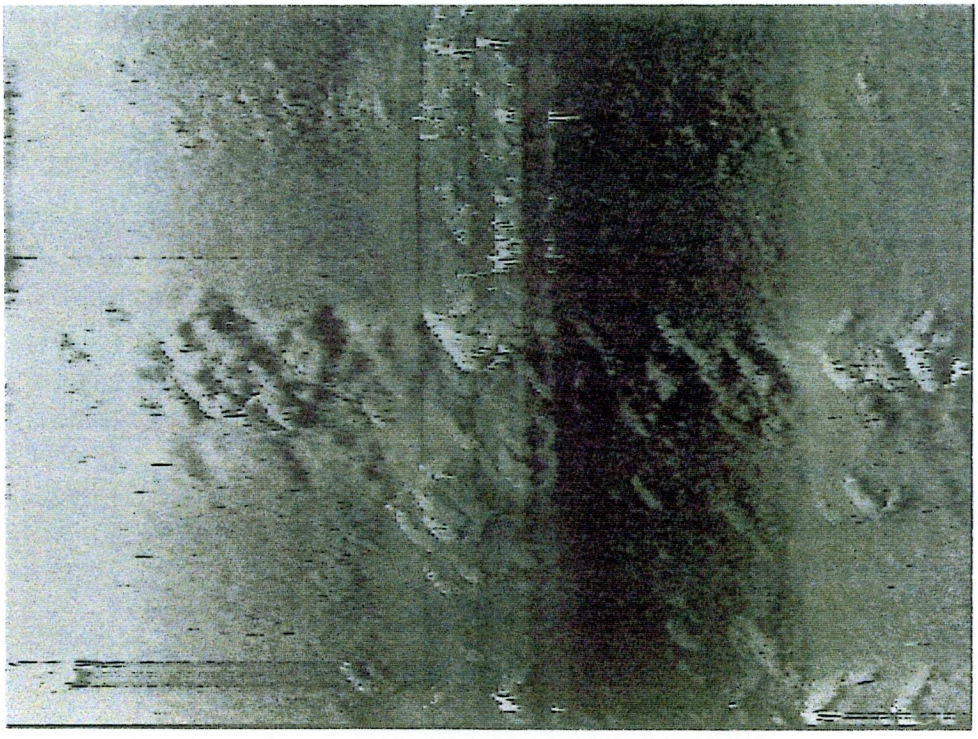

(b)

Fig. 7.9 Constant-current images obtained before (a) and after (b) the acquisition of IV characteristics across the doped layers. The damaged areas in (b) correspond to the locations where the IV measurements were made. x-range=2 μm, z-range= 68 Å.

Fig. 7.9 shows images of a GaAs np structure before and after the acquistion of IV characteristics across it. The constant current image was acquired at (+4 V, 0.1 nA) and the IV operating point was (+1 V, 0.1 nA). The tunneling set point while translating the probe was the same as the imaging set point. The voltage was ramped between -1 V and +1 V during the IV data acquisition. The images reveal that the IV scan has resulted in surface damage at the data acquisition points. Damage of this sort was observed after most such scans, as well as in the IVI scans. As discussed in §3.1, oxidation is believed to be enhanced when the tip is biased negatively with respect to the sample. It is therefore likely that the damage is induced during data acquisition, when the tip-sample voltage is ramped to negative values.

8. Conclusions and Recommendations

The STM is shown to be capable of imaging epitaxial layers on Si and GaAs with resolution of about 1 nm at ambient pressure. In particular, multilayer structures of Si/SiGe and GaAs/AlGaAs with typical layer thicknesses of 20 nm are well resolved. Wet chemical treatments are needed to stabilize the freshly cleaved surfaces for imaging in air. Tunneling-induced surface modification occurs to varying degrees on the treated n-type GaAs surfaces depending on the scanning conditions. The p-type GaAs is found to be resistant to tunneling-induced modification. The STM measurements are sensitive to carrier type, and layers of alternating n and p-type material type are resolved on GaAs for the first time in air. The pn junctions are located in constant current mode with better than 20 nm resolution.

Current-voltage characteristics of the STM tunnel junction obtained on n and p-type regions in the epitaxial layers exhibit rectifying behaviour. The asymmetry in the IV curves is exploited to obtain carrier-type contrast in a new current-voltage imaging technique. This technique makes it possible to separate the electronic contrast in the STM images associated with the doping levels from the contrast associated with surface topography.

More work needs to be done to determine appropriate values for the model parameters, in order to obtain more quantitative information from the IV curves. For example, the metal work function and semiconductor electron affinity need to be measured for these surfaces, since it is unlikely that they are the same as the values for the 'clean' surfaces in UHV. Also, it is conceivable that the dielectric constant in the air gap is greater than unity, since water will be present on the surfaces at ambient humidity. This would effect the dependence of the IV characteristics on tip-sample separation, since a higher dielectric constant would reduce the voltage drop in the gap.

References

1. C. Hill, J. Vac. Sci. Technol. B **10**, 289 (1992).

2. P. Roitman, J. Albers, and D. R. Myers, J. Appl. Phys. **55**, 4439 (1984).

3. C. Weisbuch and B. Vinter, *Quantum Semiconductor Structures,* Academic Press (1991).

4. C. Weisbuch and J. Nagle, Physica Scripta, **T19**, 209 (1987).

5. A. Zangwill, *Physics at Surfaces*, Cambridge University Press (1988).

6. S. H. Goodwin-Johansson, M. Ray, Y. Kim, and H. Z. Massoud, J. Vac. Sci. Technol. B **10,** 369 (1992).

7. R. J. Behm, N. Garcia, and H. Rohrer, *Scanning Tunneling Microscopy and Related Methods*, Kluwer Academic Publishers, 1990.

8. D. G. Cahill and R. J. Hamers, Phys. Rev. B **44**, 1387 (1991).

9. R. M. Feenstra and J. A. Stroscio, J. Vac. Sci. Technol. B **5**, 923 (1987).

10. S. Gwo, A. R. Smith, and C. K. Shih, K. Sadra, and B. G. Streetman, Appl. Phys. Lett. **61**, 1104 (1992).

11. R. Chapman, M. Kellam, S. Goodwin-Johansson, J. Russ, G. E. McGuire, K. Kjoller, J. Vac. Sci. Technol. B **10**, 502 (1992).

12. T. Tiedje and A. Brown, J. Appl. Phys. **68**, 649 (1990).

13. M. B. Johnson and J. M. Halbout, J. Vac. Sci. Technol. B **10**, 509 (1992).

14. R. Subrahmanyan, J. Vac. Sci. Technol. B **10**, 358 (1992).

15. H. Salemink and O. Albrektsen, J. Vac. Sci. Technol. B **9**, 779 (1991).

16. S. Kordic, E. J. van Loenen, and A. J. Walker, J. Vac. Sci. Technol. B**10**, 496 (1992).

17. J. A. Dagata, W. Tseng, J. Bennett, J. Schneir, and H. H. Harary, Appl. Phys. Lett. **59**, 3288 (1991).

18. J. A. Dagata and W. Tseng, App. Phys. Lett., submitted (1992).

19. B. G. Streetman and Y. C. Shih, J. Vac. Sci. Technbol. B **10**, 296 (1992).

20. W. Vandervorst and T. Clarysse, J. Vac. Sci. Technol. B **10**, 302 (1992).

21. Hans Cerva, J. Vac. Sci. Technol. B **10**, 494 (1992).

22. A. J. Melmed, J. Vac. Sci, Technol. B **9**, 601 (1991).

23. W. A. Harrison, *Electronic Structure and the Properties of Solids*, Dover Publications (1989).

24. This calibration technique was suggested to me by R. Andrews and R. Coope.

25. D. Rogers and T. Tiedje, Surface Science Letters, **274**, L599 (1992).

26. J. Jurgensen, J. Chem. Phys. **37**, 874 (1962).

27. G. S. Higashi, R. S. Becher, Y. J. Chabal, and A. J. Becker, Appl. Phys. Lett. **58**, 1656 (1991).

28. J. A. Dagata, J. Schneir, H. H. Harary, C. J. Evans, M. T. Postek, and J. Bennett, Appl. Phys. Lett. **56**, 2001 (1990).

29. T. Van Buuren, M. K. Weilmeier, I. Athwal, K. M. Colbow, J. A. Mackenzie, T. Tiedje, P. C. Wong, and K. A. R. Mitchell, Appl. Phys. Lett. **59**, 464 (1991).

30. C. Lavoie, S. R. Johnson, J. A. Mackenzie, T. Tiedje, and T. Van Buuren, J. Vac. Sci. Technol. A **10**, 930 (1992).

31. Takahisa Ohno, Phys. Rev. B **44**, 6306 (1991).

32. C. J. Sandroff, M. S. Hegde, L. A. Farrow, R. Bhat, J. P. Harbison, and C. C. Chang, J. Appl. Phys. **67**, 586 (1989).

33. J. Shin, K. M. Geib, and C. W. Wilmsen and Z. Lilliental-Weber, J. Vac. Sci. Technol. A **8**, 1894 (1990).

34. XPS and AES measurements performed by P. C. Wong.

35. J. Massies and J. P. Contour, J. Appl. Phys. **58**, 806 (1985).

36. PES performed by T. Van Buuren and T. Tiedje

37. Penn, D. R., Phys. Rev. B **13**, 5248 (1976),

38. T. Tiedje, K. M. Colbow, and D. Rogers., J. Vac. Sci. Technol. B **7**, 837 (1989).

39. M. Simard-Normandin, L. Weaver, and D. Vacca, and D. Rogers, A. Vitkin, and T. Tiedje, Can. J. Phys. **69**, 290 (1991).

40. SEM performed by M. Weiss. The Si/Ge sample was provided by J. Bean and the STM study was done in collaboration with A. Sanderson and T. P. Pearsall.

41. T. Pinnington, A. Sanderson, T. Tiedje, T. P. Pearsall, E. Kasper, and H. Presting, Thin Solid Films, accepted (1992).

42. This sample was supplied by D. C. Houghton.

43. All the GaAs samples studied in this work were grown by C. Lavoie and S. R. Johnson.

44. SEM performed by C. Lavoie.

45. T. Pinnington, S. N. Patitsas, C. Lavoie, A. Sanderson, and T. Tiedje, J. Vac. Sci. Technol, accepted (1992).

46. C. Lavoie, private communication.

47. J. A. Dagata, private communication.

48. A. Many, Y. Goldstein, N. B. Grover, *Semiconductor Surfaces*, North-Holland Publishing (1965).

49. W. A. Harrison, *Solid State Theory*, Mc Graw-Hill (1970).

50. J. S. Blakemore, J. Appl. Phys. **53**, 123 (1982).

51. The theoretical modelling and calculations were performed by S. N. Patitsas.

52. H. C. Card and E. H. Rhoderick, J. Appl. Phys. 4, 1589 (1971).

53. W. J. Kaiser, L. D. Bell, M. H. Hecht, and F. J. Grunthaner, J. Vac. Sci. Technol. A **6**, 519 (1988).

54. S. N. Patitsas, private communication.

55. C. Lavoie, private communication.

56. This sample was provided by J. P. Noel and G. Mattiussi.

Appendix. Current-Voltage Measurement Procedure

This section gives the details of the method used to obtain the current-voltage (IV) characteristics and current-voltage imaging (IVI) data presented in §7.1 and §7.2. The procedure was developed in collaboration with A. Sanderson, who wrote the software and assisted in testing.

For this procedure to work, the sample in the STM must be isolated from the chassis ground. The sample holder voltage input is connected to the BNC cable labelled 'sample' and the tip current output from the controller is connected to the BNC labelled 'current'. The dual-pin connectors 'tip bias' and 'relay' are connected to the 8-pin D-connector (STM preamp cable) and the 16-pin D-connector (computer control cable) respectively, at the back of the STM controller module. Both the IV characteristics and the IVI images are acquired after the constant-current image is obtained by exiting the image-acquisition software and running the program 'IVI'. The feedback loop is put under computer control by switching the integrator switch on the controller from 'ON' to 'HOLD', following the program prompt. This enables the software to interrupt the feedback control loop by means of the relay in the controller. The location at which data is to be acquired is selected by moving the cross-hairs to the corresponding location on the image. For an IVI-STM scan, the upper left and lower right corners of the desired scan area are selected, as well as the effective pixel size (ie. the spacing between measurement locations).

The essential features of the measurement procedure are illustrated schematically in Fig. A1. After the user has entered the pertinent data acquisition parameters as discussed below, the scanning probe is moved to the selected location (t_a). As the schematic indicates, the feedback control loop is enabled (relay 'ON') while the probe is in motion, and the tunnel current and tip bias remain at the values set by the controller. These are the

same conditions as for constant-current imaging. Once the probe has been positioned laterally, a voltage is applied to the sample, which changes the net tip-sample voltage to the data-acquisition set point (t_b). The tip-sample separation, s is adjusted by the feedback control to keep the tunnel current constant. Data are acquired by ramping the sample voltage and sampling the tunnel current, I_t (t_c). The feedback control is disabled (relay 'OFF') during data acquisition, so s is not changed. Usually more than one voltage ramp is performed, and the results averaged, to improve the signal-to-noise ratio. s is reset between voltage ramps by momentarily enabling the feedback control loop (t_d). In IVI mode, the current is measured at one selected voltage only. Once the run has been completed, the tunneling configuration is returned to the normal constant current imaging settings (t_e). In the case of IVI, the probe is moved to the next location. Note that the tip bias, which is set by the control module, remains fixed throughout the entire procedure.

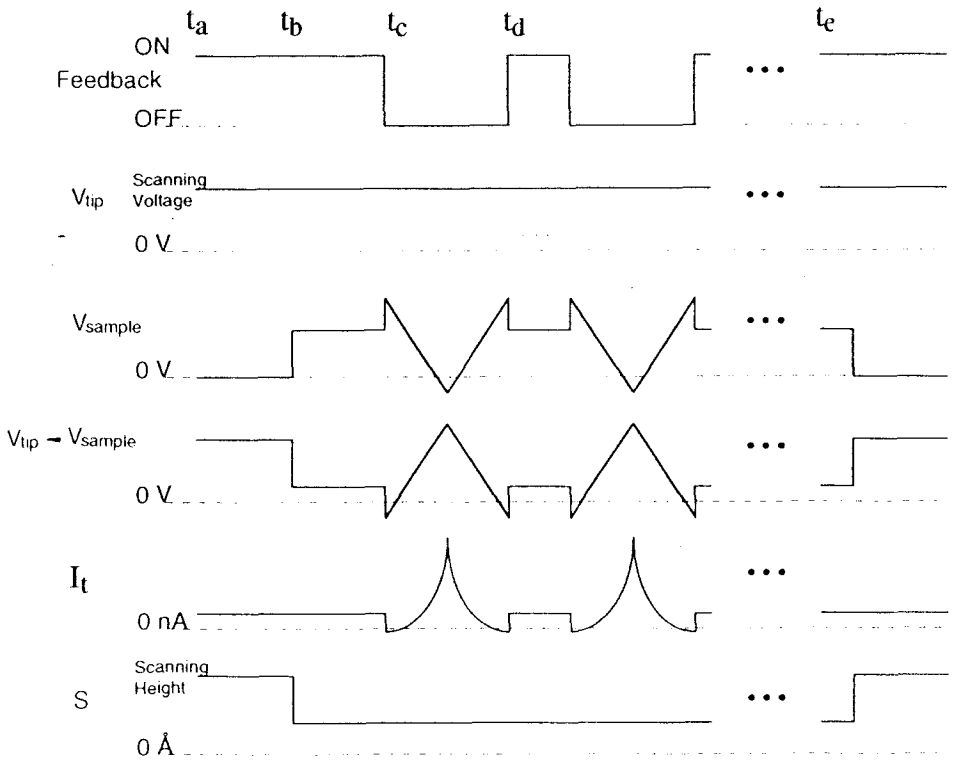

Fig. A.1. Voltage waveforms in the IV and IVI measurements. The tip voltage is unchanged throughout the procedure. Typically 20 voltage ramps are averaged each run, and the tip-sample separation is reset between eacn ramp by briefly enabling the feedback as shown.

A typical sample voltage waveform for IV data acquisition is shown in detail in Fig. A.2. Note that the voltage is ramped down and up while data are acquired (bold portion of waveform). The current readings from the two ramps are averaged. The voltage is actually incremented in discrete steps, where the magnitude of the increment, or step size, is set by the user. During data acquisition, the current is sampled after each voltage step. The ramp rate for voltage changes made while data is not being acquired is set separately. If the step size is greater than the actual ramp range, the voltage ramp is made in a single step. Several time delays are used and are also set by the user. A description of each is given below, along with the default setting.

τ_1: time delay after resetting relay. The mechanical relay specifications are 6ms to activate (ON) and 3 ms to disengage (OFF). Default setting: 10 ms

τ_2: time delay after setting or resetting tip-sample separation for data acquisition. This is to allow the feedback loop establish the set point current after the sample voltage has been changed. Default setting: 100 ms

τ_3: time delay after setting the tip-sample separation to the scanning set point in IVI mode, before moving the probe to the next imaging location. Default setting: 100 ms

τ_4: time delay after each motion of the probe. This sets the scan rate for positioning the

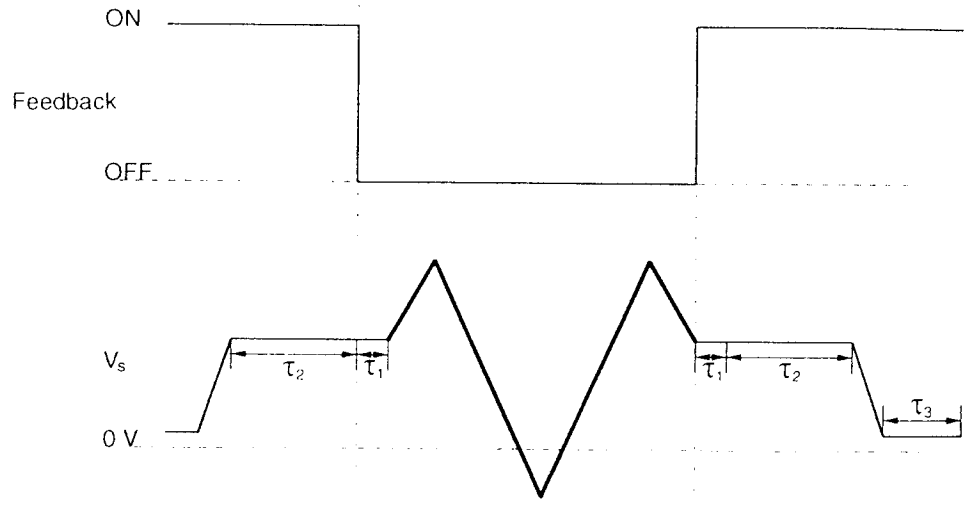

Fig. A.2. Detailed schematic of the sample voltage waveform during an IV measurement, showing the various time delays (see text).

probe, in both IV and IVI modes. The probe motion is in discrete steps, with each step corresponding to 2 pixels on the screen or 1/256 of the image width. Default setting: 10 ms. This corresponds to 2 seconds to scan the full width of the screen.

In order to establish an acceptable voltage range for the IV data acquisition, the 'quick run' feature may be executed. Here, allowed current limits are entered as inputs. The sample voltage is ramped up and down while monitoring the current until the current limits are reached or the maximum voltage range (±10 V on the sample) is exceeded. The corresponding voltage range is given as output.

As discussed on p. 78, tip noise might cause the tip-sample separation, s to be set inconsistently, perhaps by one or two angstroms. Accordingly, s is checked indirectly by monitoring the tunneling current immediately after the feedback is disabled. A specified number of current readings are taken (default setting: 50) and averaged. If these differ by more than the specified tolerance (default setting: 50%) from the set point current, then s is reset by enabling the feedback for τ_2 seconds. This process is repeated until the tolerance is met or the number of permitted attempts (default setting: 10) is exceeded, in which case the measurement is aborted. In IVI mode, the computer beeps and a default value corresponding to saturated white (+10 nA) is recorded for that data point.

The data are displayed immediately after acquisition and may be saved on disk as ASCII files. The current range greyscale for the IVI-STM image is adjusted by the user after data acquisition to obtain the desired visual contrast. The actual data file is unaffected by the contrast settings, which are not stored.